AD-A043 178 NAVAL RESEARCH LAB WASHINGTON D C F/G 4/1

POST STABILIZATION IONIZATION LEVEL PREDICTIONS. VOLUME III OF --ETC(U)

APR 77

UNCLASSIFIED NRL-MR-3488 NL

1 OF 2

ADA043178

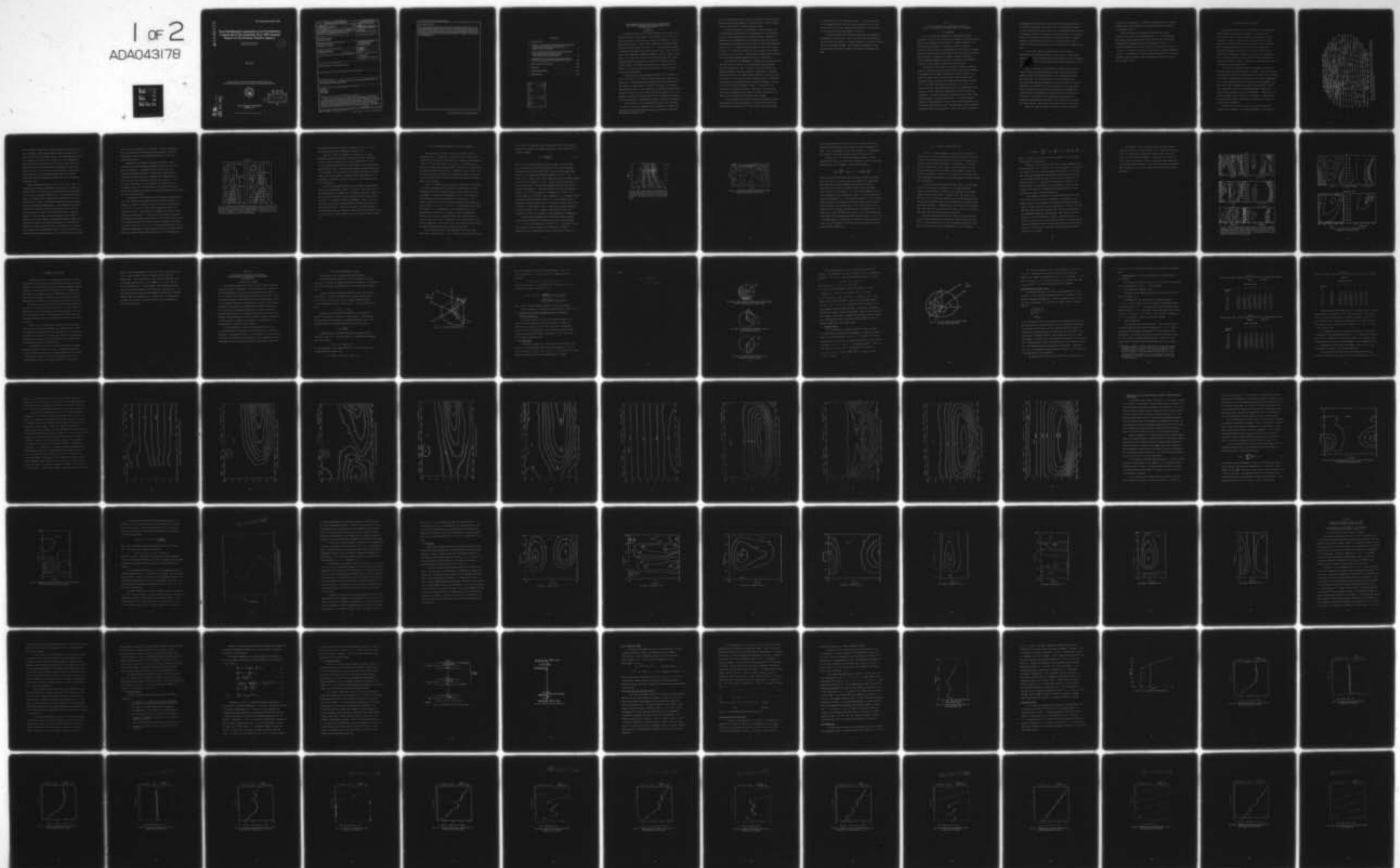

NRL Memorandum Report 3488

Post Stabilization Ionization Level Predictions Volume III of the Calendar Year 1975 Annual Report to the Defense Nuclear Agency

12

Plasma Dynamics Branch
Plasma Physics Division

April 1977

This research was sponsored by the Defense Nuclear Agency under subtask S99QAXHC065, work unit 08, and work unit title High Altitude Debris.

NAVAL RESEARCH LABORATORY
Washington, D.C.

SECURITY CLASSIFICATION OF THIS PAGE (When Data Entered)

9

REPORT DOCUMENTATION PAGE

READ INSTRUCTIONS BEFORE COMPLETING FORM

1. REPORT NUMBER: NRL Memorandum Report 3488

2. GOVT ACCESSION NO.: 14

3. RECIPIENT'S CATALOG NUMBER: NRL-MR-3488

4. TITLE (and Subtitle): 6 POST STABILIZATION IONIZATION LEVEL PREDICTIONS, VOLUME III OF THE CALENDAR YEAR 1975 ANNUAL REPORT TO THE DEFENSE NUCLEAR AGENCY

5. TYPE OF REPORT & PERIOD COVERED: Interim report on a continuing NRL problem.

6. PERFORMING ORG. REPORT NUMBER:

7. AUTHOR(s): Plasma Dynamics Branch, Plasma Physics Division

8. CONTRACT OR GRANT NUMBER(s):

9. PERFORMING ORGANIZATION NAME AND ADDRESS: Naval Research Laboratory, Washington, D.C. 20375

10. PROGRAM ELEMENT, PROJECT, TASK AREA & WORK UNIT NUMBERS: NRL Problem A02-36, DNA Subtask HC065

11. CONTROLLING OFFICE NAME AND ADDRESS: Defense Nuclear Agency, Washington, D.C. 20305

12 135 p.

11

12. REPORT DATE: April 1977

13. NUMBER OF PAGES: 152

14. MONITORING AGENCY NAME & ADDRESS (if different from Controlling Office):

15. SECURITY CLASS. (of this report): UNCLASSIFIED

15a. DECLASSIFICATION/DOWNGRADING SCHEDULE:

16. DISTRIBUTION STATEMENT (of this Report)

Approved for public release; distribution unlimited.

17. DISTRIBUTION STATEMENT (of the abstract entered in Block 20, if different from Report)

18. SUPPLEMENTARY NOTES

This research was sponsored by the Defense Nuclear Agency under Subtask S99QAXHC065, work unit 08, work unit title High Altitude Debris.

19. KEY WORDS (Continue on reverse side if necessary and identify by block number)

Mesosphere
Wind patterns
Nuclear debris

20. ABSTRACT (Continue on reverse side if necessary and identify by block number)

Patches of ionized air produced by the passage through the atmosphere of beta radiation emitted from nuclear debris clouds pose a potential threat to satellite communications. The distribution of the debris and the consequent ionization has been shown to be strongly a function of the mesospheric wind fields. Observational data for these wind fields is shown, upon analysis, to be inadequate for systems application and theoretical models have been developed to remedy this. The circulations in the upper atmosphere are driven by the time-dependent influx of solar radiation

(Continues)

DD FORM 1 JAN 73 1473 EDITION OF 1 NOV 65 IS OBSOLETE
S/N 0102-014-6601

SECURITY CLASSIFICATION OF THIS PAGE (When Data Entered)

251 950 mt

20. Abstract (Continued)

which is represented by a heating function used as input to the general circulation models. An improved heating function has been obtained and included in the NRL linear model, results for which are presented. Results obtained from improvements in the NRL program for the simulation of solar tidal influences are also presented. Finally, a computer program for predicting beta induced electron density distributions at any time after a nuclear burst is described. The program is suitably efficient for systems applications.

CONTENTS

POST STABILIZATION IONIZATION LEVEL PREDICTIONS
Volume III of the Calendar Year 1975 Annual Report to the Defense Nuclear Agency

Section 1
INTRODUCTION

Widespread ionization of the lower atmosphere by emissions from radioactive debris clouds formed in the aftermath of high altitude nuclear explosions is potentially a source of interference to satellite communication systems. Debris clouds, advected by mesospheric winds, have been shown by Zalesak and Coffey (1975) to spread over distances of hundreds of kilometers from the burst point within a few hours after detonation in addition to undergoing dramatic changes in shape. Typically, a cloud develops from an initial spherical shape into a highly elongated configuration under the influence of short-scale length vertical shears. The predictive capability for communications interference is very much a function of the accuracy of the mesospheric wind field data available.

The wind fields used by Zalesak and Coffey (1975) are given by Groves (1969),CIRA (1972), based on observational data acquired over many years. The mean deviations associated with these data indicated the presence of inconsistencies that were confirmed by a subsequent, more detailed analysis. This analysis of the observational data, which appears in section 2 of this volume, provides the impetus for the NRL program to develop theoretical models of the mesospheric circulation which could be used to substantially improve the wind data reliability.

Initial studies of the mesospheric circulation were undertaken as a part of last year's program with the assembly of a linear model for the mean circulation and both analytic and numerical simulation

Note: Manuscript submitted April 7, 1977.

of solar tidal phenomena which represent substantial diurnal and semidiurnal perturbations superposed on the mean winds. Further progress in each of these areas is reported in this volume.

The mean circulation of the mesosphere is driven primarily by the differential heating caused by the absorption of solar radiation by ozone. The parametization of radiative heating is comparable in importance to the parametization of Rayleigh friction and radiative cooling which were optimized in the initial NRL linear model(Baker and Strobel, 1975). The radiative heating function taken from the work of Leovy (1964) has been replaced by the more accurate one described in section 2 of this volume. Results from the updated model containing the new radiative heating parametization are also presented.

The response of the atmosphere to diurnal and semidiurnal heating has been studied at NRL with a three-dimensional numerical model initially reported last year. The model, which uses pressure as a vertical coordinate, has been improved by insertion of a prognostic equation to determine the lower boundary condition at every time step in contrast to the earlier versions's assumption that the substantive derivative of the pressure was zero at the lower boundary. Grid resolution has also been increased to about 0.5 km from the 4 km resolution of the earlier version. This permits the more accurate simulation of propagating waves under the general prescription that eight to ten grid points per wavelength are necessary.

A fast running code suitable for systems applications has been prepared which follows the movement of a debris cloud using input wind data and calculates the ion density distribution attributable

to beta emission from the radioactive debris. The betas are guided by the geomagnetic field lines into regions conjugate to the cloud. A description of this code along with a discussion of the accuracy of the beta deposition treatment appears in section 4.

The work performed at NRL during the past year is summarized in the remainder of this volume. Much of this work has been previously reported in NRL Memo Reports, at several symposia, in technical journals, and at DNA sponsored meetings. The principal contributors in each technical area are listed as authors of the section describing that work.

Section 2

A CRITICAL ANALYSIS OF CLIMATOLOGICAL WIND DATA USED IN THE FORECAST OF RADIOACTIVE DEBRIS CLOUD MOVEMENT

M. R. SCHOEBERL

It is of considerable importance to communication system performance (ELF, VLF, HF) in a nuclear environment to be able to predict debris cloud transport in the mesosphere. Zalesak and Coffey (1975) have shown that transport can profoundly alter the location of radioactive debris clouds. The subsequent beta decay within the cloud results in long lasting, widespread ionization that can severely affect the performance of communication systems. Accurate prediction of system performance depends critically on our ability to describe the movement of debris patches by mesospheric wind systems.

The purpose of this report is to assess the present method by which the spread of radioactive debris clouds in the upper atmosphere is determined and to suggest guidelines for future research. The current technique used to forecast debris cloud advection uses a Lagrangian computer code with model wind fields (Zalesak and Coffey, 1975). The wind fields are given by Groves (1969), CIRA (1972). These wind fields, being based upon many years of observational data, represent the best statistics available at the time the study was undertaken. The results produced by Zalesak and Coffey clearly hinge upon the accuracy of the wind field data. It is thus important to examine the data carefully and ask if these wind fields actually give an accurate representation of the upper atmospheric motions relevant to determining debris cloud advection. Groves' data are an "average" or

climatological representation of the wind field from which some spatial and temporal fluctuations have been removed by the averaging process. If these fluctuations are quite small, then the averaged data may be used to accurately forecast the transport of trace constituents. On the other hand, if the fluctuations are large, the actual wind field may rarely resemble the climatological wind field and resulting debris cloud forecasts based upon the latter will be reliable only in a climatological sense.

In this report the wind fields given by Groves shall be examined with the following criteria. First, we can, to some extent, quantitatively assess variability within the wind field data by examining the standard deviation of the climatological average published by Groves (CI[illegible]).

Second, we examine the consistency of the data with theoretical models of upper atmospheric dynamics. While inconsistency between empirical models and theoretical models does not necessarily imply unreliable data, consistency allows us to use theoretical models where empirical data may be lacking or difficult to obtain. From this viewpoint we can determine if the wind structure of the upper atmosphere as computed from theoretically postulated heat and momentum sources bears any resemblance to the empirical wind structure given by Groves. Or conversely, we can compute the implied heat and momentum sources required to maintain Groves' wind model and compare with known sources. Both aspects of this problem will be discussed.

Third, the zonal wind model of Groves is tested for stability

to small wave perturbations. Instability probably implies the presence of large scale eddy mixing which could greatly affect the transport of radioactive debris.

Within the body of this report the data and its observed variability of the data are discussed in Part 2.1. The implied heat and momentum sources derived from Groves' data and the theoretically predicted heat and momentum sources are compared in Part 2.2. Stability computations for Groves' wind model are presented in Part 2.3. In Part 2.4 we conclude that Groves' wind fields are probably inadequate for debris cloud advection forecast purposes and suggest that theoretical prediction models currently under development can be used to provide more reliable results.

2.1 UPPER ATMOSPHERIC WIND DATA

Wind observations above 30 km and below 150 km are principally obtained through rocket based techniques. At high altitudes a meteorological rocket releases an object or chaff which is tracked by radar as it falls. Lateral motion of the falling object then yields horizontal wind data and the local density of the atmosphere may be computed by observing the rate of fall. Compared with radiosonde observations used below 30 km, rocket methods are very expensive and technologically complex. As a result, the network of rocket launching stations is quite sparse and regular observations are taken only weekly. Figure 2.1 shows the station locations for the Meteorological Rocket Network (MRN).

The rocket data obtained through the MRN facilities contains both systematic and random deviations or "errors". Both kinds reduce the usability of the derived climatological wind models for forecasting. We may further subdivide the deviations into those due to measurements (e.g., faulty radar techniques) and those due to the phenomena (e.g., small scale eddies inadequately resolved by the MRN grid). Quiroz (1969) discusses systematic and random measurement deviations at length and his findings will not be reviewed here. Measurement error of the systematic type is assumed to be negligible, whereas random error associated with the measurements is assumed to be removed by climatological averaging.

Probably the most obvious source of systematic deviations associated with phenomena in the upper atmosphere is that produced

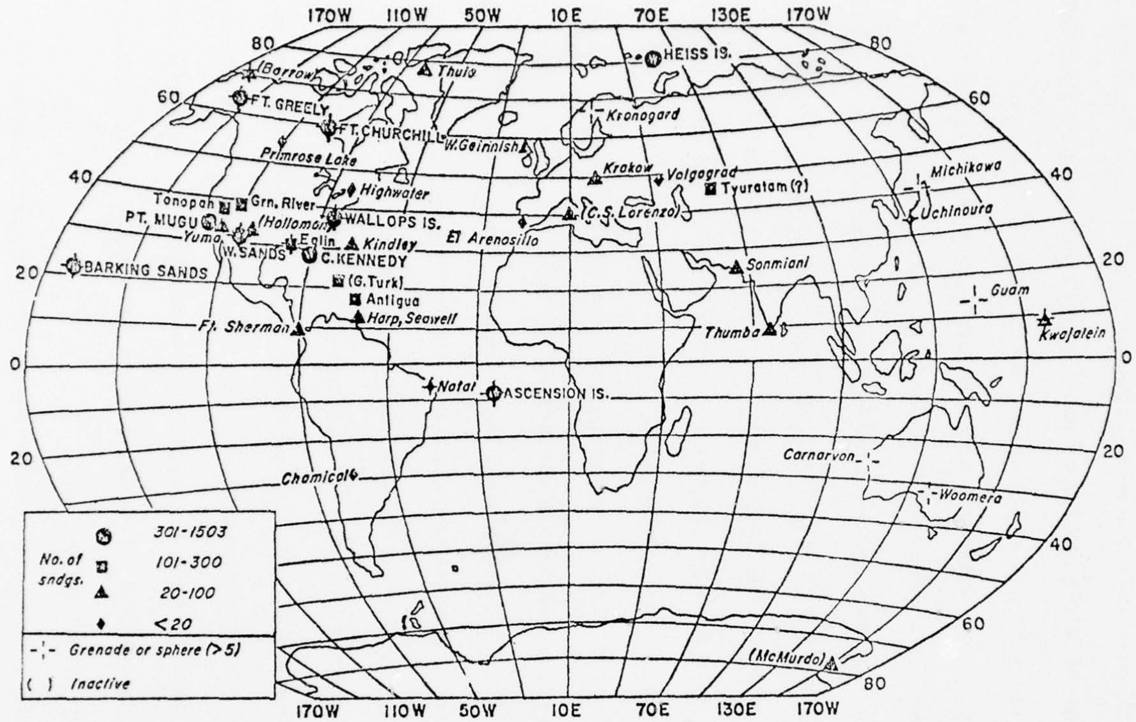

Fig. 2.1 — Rocket network station locations as of 1968. Some significant modifications have occurred since then, such as the introduction of the Soviet Antarctic rocket program at Molodeylinaza (68S,46E) in 1969

by the presence of tidal winds. Most MRN data is taken at local noon. Thus, if regular diurnal and semidiurnal tidal wind components are present, they will be interpreted in any local climatological analysis as a component of the mean wind. Lindzen (1967) has computed the amplitude of the tidal winds up to 100 km and has found that winds associated with the solar semidiurnal and diurnal tides may be as large as 100 ms^{-1} at 100 km in the zonal direction. Measurement of tidal winds below 60 km shows general agreement with Lindzen's computation with some disagreement evident above 60 km (Glass and Spizzichino, 1974).

Groves' wind model presented in CIRA (1972) (also Groves, 1969) has been constructed by grouping MRN and other data into monthly or bimonthly sets. The data within a set have been further subdivided into four hour time groups depending on the local time the data were taken. The average within each group was computed as well as the mean deviation. Above 60 km Southern Hemisphere data were assumed to be equal to Northern Hemisphere data. Final wind model values were computed by an iterative scheme involving the average of the mean deviations and the average of the group averages and a weighting formula. Using an average of the group averages is equivalent in some sense to a daily average. Provided large monthly changes in the amplitude and phase of the tidal components do not occur and data samples are present within each group, this method should eliminate the systematic error introduced by tides. In reality, however, many groups lack data altogether above 60 km so that model points are based

upon only one or two groups (cf. CIRA, 1972). We may conclude then that high altitude winds presented by Groves probably contain considerable bias from tidal winds superimposed upon the zonal and meridional mean winds.

Essentially, the systematic deviation introduced by tidal components results from inadequate temporal resolution of the zonal mean wind components. Inadequate spatial resolution can also introduce systematic deviations. In particular, quasistationary planetary scale waves as well as tides have wind components which vary very slowly over horizontal distances on the order of 5,000 to 10,000 km. From Figure 2.1 it is apparent that MRN stations are principally located in the northern part of the Western Hemisphere, and thus the network will be unable to resolve wind components associated with very long zonal scales.

A comparison of West European and North American data presented in CIRA (1972) indicates the presence of these long spatial waves. For example, in January the mean zonal wind velocity over North America is $\sim$20 ms^{-1} at 50 km at 55°N, while the mean zonal wind velocity over Europe is $\sim$80 ms^{-1}. The difference is presumably attributable to the long wave wind components. The difference between North American and European mean zonal wind velocities below 60 km is largest during winter and is consistent with the observed strength of planetary scale waves below 30 km (van Loon, et al., 1973). Theoretical calculations of the amplitude of stationary planetary waves in the upper atmosphere indicate that these waves may have sizable amplitudes up to the mesopause and

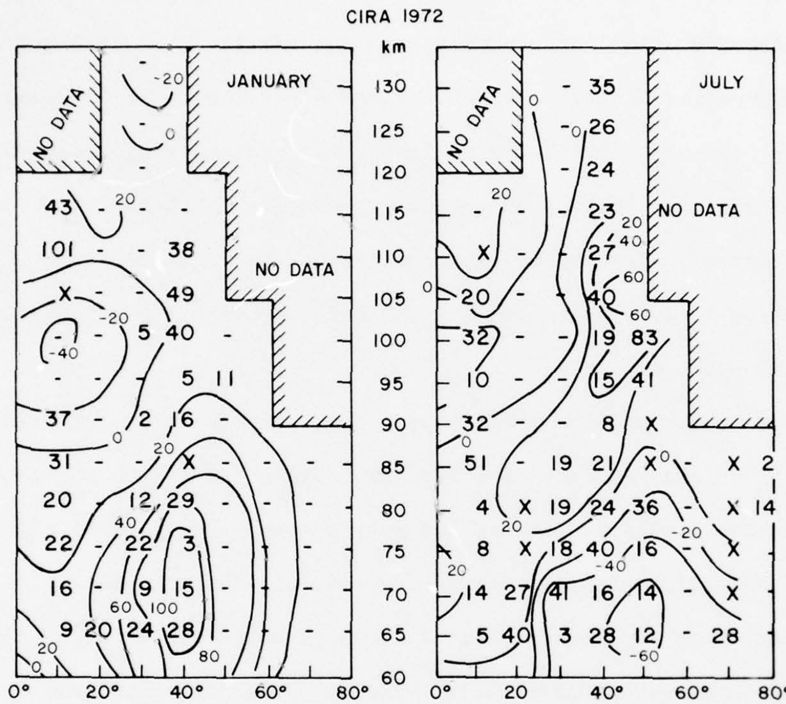

Fig. 2.2 — January and July statistical wind data used to construct the CIRA (1972) model atmosphere. Bold face numbers show the standard deviation in meters per second of the observational data at the indicated altitudes. X's indicate only a single measurement available; —'s indicate no measurements. Contours labeled with light numbers are model wind values in meters per second.

may generate zonal wind components as large as 20 ms^{-1} - 30 ms^{-1} in the mesosphere and lower thermosphere (Schoeberl, 1975).

Small scale eddies are probably also present in the upper atmosphere generated by baroclinic instability near the stratopause. If their horizontal length scales are much smaller than 1000 km, then the spatial distribution of the MRN network will be inadequate to properly resolve them. These eddies will appear as random fluctuations in the MRN data. For the purpose of predicting the location of debris clouds, these eddies may be as important as the zonal mean flow. No information is available from Groves' models on their possible structure or amplitude.

All of the phenomena discussed above contribute to the standard deviation of the MRN data as error. In Figure 2.2 the model values of the mean zonal wind in January and July above 60 km given by CIRA (1972) and the standard deviation of the observations from the model values are given. Two important features are apparent. First, it is clear from the large number of missing standard deviations how limited the data base actually is. Second, we note that the standard deviation is often larger than the mean value indicating that climatological state of the wind field (Groves' model) occurs as an exception rather than the rule.

2.2 HEAT AND MOMENTUM SOURCES IN THE UPPER ATMOSPHERE

The mean zonal circulation is driven by external heat and momentum sources. In some cases, these sources may be theoretically computed and a circulation model developed to compare with observations (Leovy, 1964; Baker and Strobel, 1975_a, 1975_b). Alternatively, a wind model derived from data can be used to calculate the implied heat and momentum sources which may then be compared to theory (Ebel, 1974). We shall consider the consistency of computed wind models and implied heat and momentum sources with their observed and theoretical counterparts in this section.

Leovy (1964) showed that the westerly stratospheric jet observed in the winter hemisphere and the easterly jet observed in the summer hemisphere arise from the meridional ozone heating gradient in the stratosphere. Mean zonal wind maximums of 80 ms^{-1} were computed by Leovy associated with mean meridional wind velocities of 0.7 ms^{-1}. The mean zonal wind velocities fluctuate in magnitude throughout the winter (Belmont, et al., 1975), but 80 ms^{-1} is relatively good agreement with Groves' (1969) climatological value considering many of the simplifications used by Leovy. However, Groves' mean meridional velocities are an order of magnitude larger than those computed by Leovy and Baker and Strobel. Furthermore, their meridional winds blow from the summer pole to the winter pole, while Groves' meridional winds are quite variable depending upon latitude and altitude.

The discrepancy between these computations and Groves' data may be due to several factors. First, assuming Groves meridional winds

are correct, the mean zonal winds (which result from Coriolis torques acting upon northward or southward moving flow) may be computed by the following equation.

$$\bar{u} = \frac{2\Omega\bar{v}\ \sin\theta}{\beta_R} \tag{2.1}$$

where Ω is the earth's frequency of rotation and θ is the latitude. β_R is the Rayleigh friction coefficient; $\bar{v}$ is the zonally averaged meridional velocity of the wind, and $\bar{u}$ is the zonally averaged zonal velocity. β_R is unknown but has been estimated to be $\sim 10^{-6}\ \text{sec}^{-1}$ (Leovy, 1964). Using 10 ms^{-1} for $\bar{v}$, which is the order of magnitude given by Groves (1969), gives $\bar{u} = 1000\ \text{ms}^{-1}$, which is inconsistent with the $\bar{u}$ values also given. If $\bar{u}$ and $\bar{v}$ are assumed correct, we are forced to conclude that equation (1) does not describe the correct relationship between $\bar{u}$ and $\bar{v}$, and the addition of a momentum source term, M, of unknown value to the righthand side of Equation (2.1) is required to form a consistent equation between $\bar{u}$ and $\bar{v}$. It is also apparent that the magnitude of M must be quite large. The presence of eddies which could contribute to M are known to exist in winter but are generally absent in summer (Kriester, 1972). However, large values of $\bar{v}$ are also indicated by Groves for the summer, so this explanation is implausible.

A more complete calculation of the required momentum and heat sources needed to maintain the Groves model winds in the mesosphere (70 - 100 km) has been carried out by Ebel (1974). The strength of the heat sources is shown in Figure 2.3 for solstice conditions. A comparison with the computed heat sources from Park and London (1973),

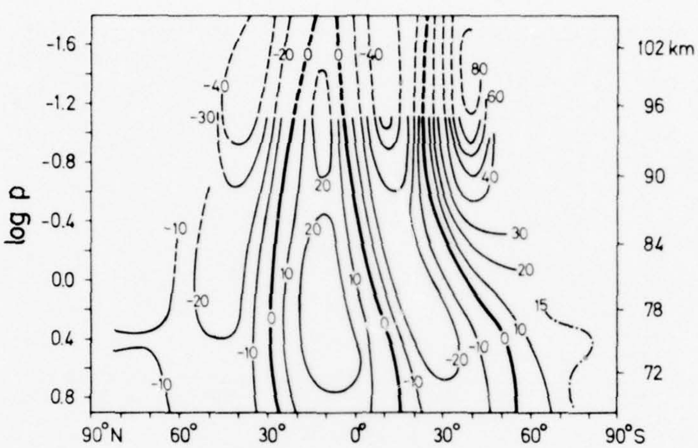

Fig. 2.3 — Heat sources required to maintain Groves' observationally based wind models during solstice as computed by Ebel (1974). Units are 10^{-5} K/S or 0.864 K per day. The winter pole lies in the northern hemisphere.

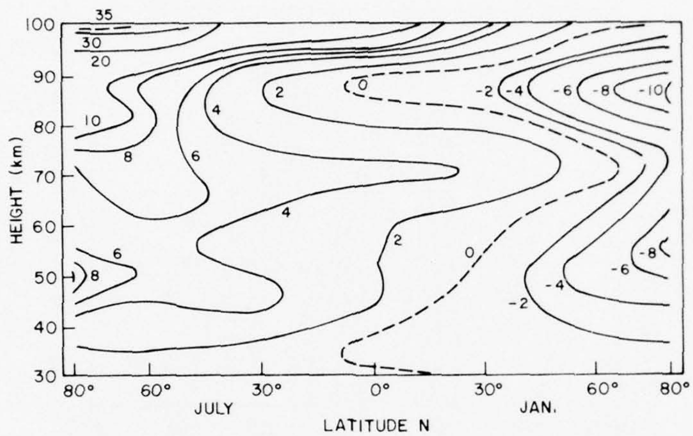

Fig. 2.4 — Theoretically computed heating rates for solstice conditions after Park and Jordon (1974)

Figure 2.4, indicates that the value of the heat sources required to maintain the Groves wind field is roughly an order of magnitude too large. Thus, in agreement with our above arguments, it is improbable that Groves' $\overline{v}$ values are consistent with the $\overline{u}$ values given.

Equation (2.1) is the zonal mean momentum equation. If, as suggested in Section 2.1 the MRN data is biased by tidal and stationary planetary waves, then Equation (1) should be written as

$$\beta_R u_g + \frac{\partial u_g}{\partial t} + 2\Omega v_g \sin\theta = \frac{1}{a\cos\theta}\frac{\partial\Phi}{\partial\lambda} \qquad (2.2)$$

where Φ is the geopotential and the subscript g indicates the values given by Groves (1969) which are now not assumed to be zonal means. Both tidal and long wave components can theoretically produce meridional wind velocities as large as those reported in Groves' model (Lindzen, 1967; Schoeberl, 1975) and in all probability it is these components that are reported by Groves. The larger velocities permitted by Equation (2.2) arise from the presence of a zonal pressure gradient force on the righthand side and the second term on the left-hand side which is an inertial term. Both of these terms are much larger than the term $\beta_R u_g$ for planetary scale and tidal motions. The value of v_g is thus not coupled to u_g alone. For tidal and planetary scale waves, both observations and theory indicate that $u \sim v \sim 10\text{-}20$ ms^{-1} in the stratosphere. These values of v are more consistent with the values of v_g and suggest that the data are indeed biased by planetary wave and tidal components.

2.3. STABILITY OF MEAN ZONAL FLOW

While it is nearly impossible to quantitatively estimate the magnitude of the bias that long wave components and smaller scale eddy components have introduced into Groves' wind fields, we can gain some estimate through a stability analysis. Our argument is as follows: If the mean zonal wind field is stable to wave perturbations, then any finite amplitude eddy disturbances can be assumed to arise from boundary (tropospheric) forcing. If the flow field is unstable, then finite amplitude disturbances may arise spontaneously from infinitesimal, local disturbances.

It has been shown by Charney and Drazin (1961) that only large planetary scale eddies can propagate into the upper atmosphere. Synoptic scale disturbances observed in the troposphere will remain trapped below the stratosphere. Dickinson (1973) and Simmons (1975) have shown that the long wave components are the fastest growing modes for unstable flow fields similar to those observed in the upper stratosphere and mesosphere. A computation of the stability of the observed zonal mean flow field as given by Groves (CIRA, 1972) may thus indicate where large amplitude eddy components could arise.

Using the Charney-Stern stability criteria (Charney and Stern, 1962) we compute numerically the stability of Groves' mean zonal wind field. In the stability criterion for an atmosphere bounded by rigid walls, a necessary condition for instability is that Q, defined as

$$Q \equiv 2(\Omega+\bar{\omega}) - \frac{\partial^2\bar{\omega}}{\partial\theta^2} + 3 \tan\theta \frac{\partial\bar{\omega}}{\partial\theta} - \sin^2\theta\, e^z \frac{\partial}{\partial z} \frac{e^{-z}}{S} \frac{\partial\bar{\omega}}{\partial z} \quad (2.3)$$

where $z - \ell n(p_o/p)$, $\bar{\omega} = \bar{u}/a \cos\theta$, and p is pressure, does not change sign within the bounded region.

Figures 2.5 and 2.6 show the value of Q computed numerically for parts of the CIRA (1972) and CIRA (1965) model atmospheres, respectively. Also shown is a plot of the corresponding flow pattern. It is evident that these model atmospheres have unstable regions, particularly near the stratopause and near the pole at all levels, as indicated by the negative values of Q. A term by term examination of Equation (2.3) indicates that the sign change in Q is principally a result of sign changes in the last term. Instabilities developing from this flow pattern would thus be primarily baroclinic.

The assumption that Groves' wind models characterize the mean zonal flow field is, of course, introduced in this analysis. One example where such an assumption is certainly incorrect is evident in Figure 2.4 where a patch of negative Q appears to 50°N and 30 km in the wind model taken from North American data. No such region appears in the computations based upon European data. The source of the sign change in Q is the appearance of a region of easterly winds in the midst of a westerly jet in the North American data. The winds in this region are probably strongly biased by planetary waves as discussed in Section 2.1 and not zonal means; hence, the Charney-Stern stability criteria does not apply.

The existence of high frequency motions at the stratopause have been observed by Leovy and Akerman (1973), and these motions may be due to unstable wind configurations such as those given by the CIRA (1972, 1965) model atmospheres. In any event, the fact that Groves' models are unstable indicates that either eddy components of the wind have biased the data to such an extent that the wind profile appears unstable; or, that eddy components are present with sizable amplitudes.

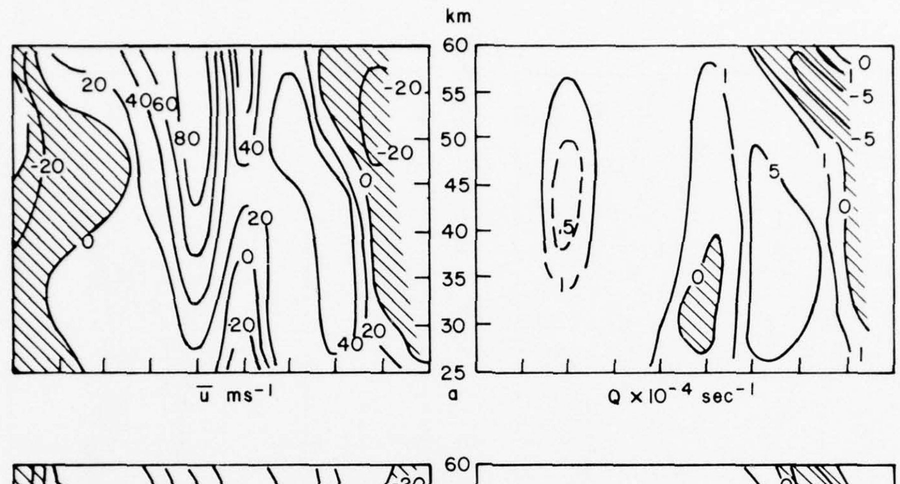

Fig. 2.5 — The zonal wind model (left) and value of Q defined in text (right) computed for CIRA (1972) Northern Hemisphere data (top), CIRA (1972) Western European data (center), and all longitudes for the mesosphere (bottom). Wind profiles for January were used in all instances. Sign changes in Q are necessary conditions for instability in the wind profile.

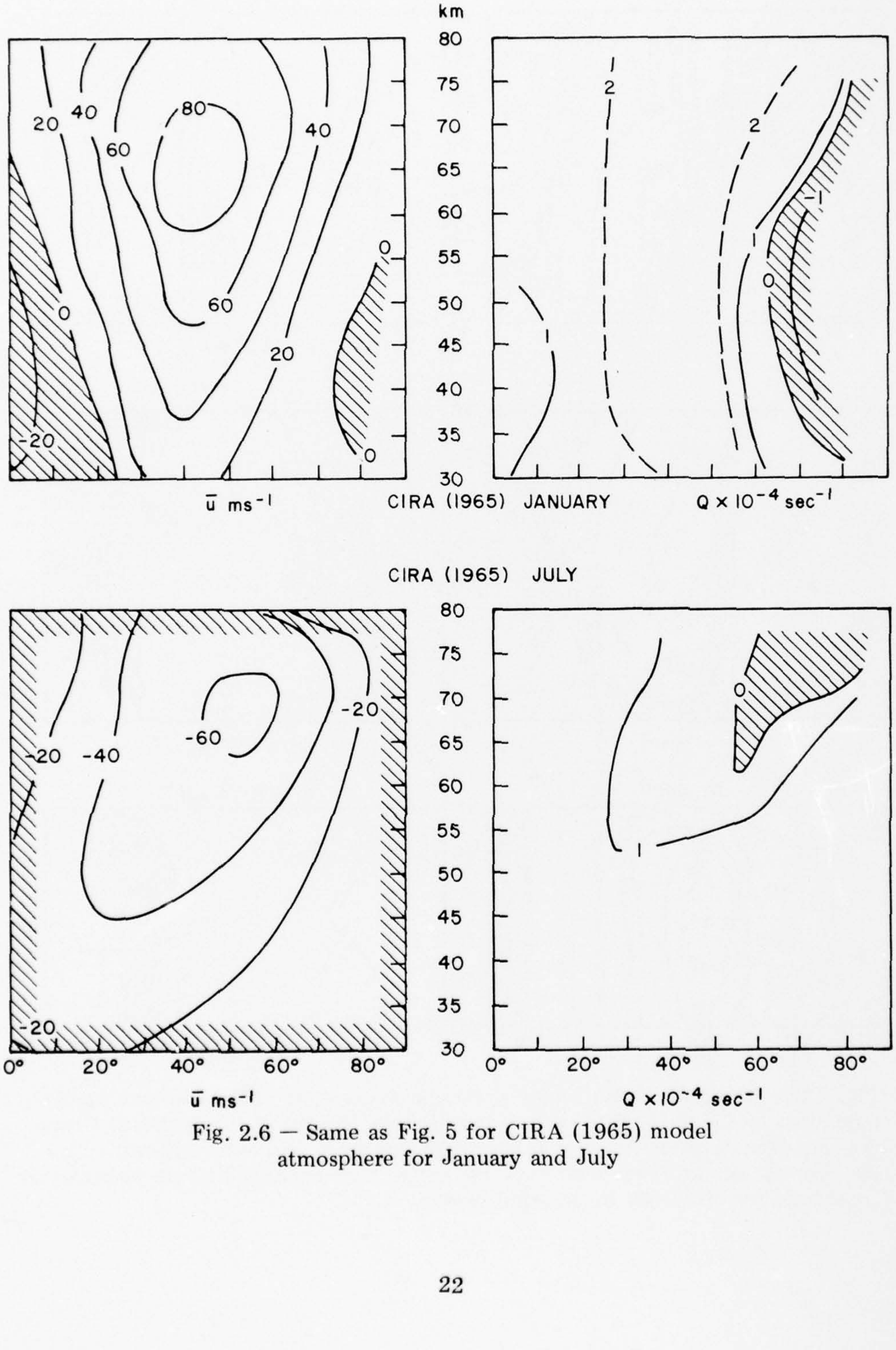

Fig. 2.6 — Same as Fig. 5 for CIRA (1965) model atmosphere for January and July

2.4. SUMMARY AND CONCLUSION

The usability of Groves' climatological wind fields for forecasting debris cloud advection has been assessed from three different viewpoints. We have briefly discussed the data and suggested possible biasing of the wind field by tidal, planetary wave, and amall scale eddy motions. An examination of the standard deviation of the data indicates that the actual structure of the wind field in the upper atmosphere rarely resembles the climatological data given by Groves.

We have also examined the heat and momentum sources implied by wind fields. The values of $\bar{v}$ given by Groves (1969) are an order of magnitude too large, and imply heat and momentum sources much larger than expected from theory. We conclude that the $\bar{v}$ values actually represent meridional velocities associated with planetary scale waves and tides.

Finally, we note that Groves' zonal wind fields are unstable, especially near the polar stratopause. The instability could imply the existence of large amplitude eddy components in the wind field for that region. We conclude then that Groves' wind fields inadequately represent the structure of the upper atmosphere for the purposes of forecasting the advection of debris clouds.

An alternative to the use of Groves' wind fields to forecast movement of a debris cloud is the use of a theoretical prediction model which can be initialized on a regular schedule or at the moment of debris cloud release. Such a model is presently used in the lower atmosphere and gives reliable forecasts up to three days in

advance. With some adaptations, this type of model can be constructed for the upper atmosphere and can be initialized with satellite radiance data. This data, which is in the form of temperature fields, is currently available up to 60 km (Chapman, et al., 1972) and will soon be available up to 80 km and higher. Upper atmosphere forecast models are under development at NRL at present. Madala, et al., (1975) have shown that tidal winds can be adequately simulated with a spectral forecast model, and Schoeberl (1975) has been able to determine theoretically the structure of planetary waves in the upper atmosphere using a similar method.

Section 3

CALCULATIONS OF HEATING DUE TO ABSORPTION OF SOLAR RADIATION BY OZONE IN THE STRATOSPHERE AND MESOSPHERE

L. Baker and D. Strobel

The thermal structure and circulation of the "upper atmosphere" (upper stratosphere - mesosphere - lower thermosphere) are controlled by the thermodynamics of that region; specifically the absorption of solar radiation and the radiative transport of heat energy. As part of an upper atmospheric modelling effort of the Plasma Dynamics Branch of NRL, a general computer code was written to treat the first problem-absorption of insolation by an absorber with arbitrary distribution. This code may be used through various entries to give either mean, seasonal heatings for use in climatological forecasts or to give point-by-point local heating rates, as would be useful in tidal calculations. It can be useful in studying the interaction of circulation and the photochemistry of ozone and other absorbers.

Most descriptions of radiative heating calculation in the literature have been very sketchy as to the details of the integration procedure. We intend this report to fully document this code. Because this code is not intended for applications to the troposphere and lower stratosphere, we do not include scattering or atmospheric refraction.

3.1 CALCULATION OF HEATING AT A POINT

This chapter and the next deal mostly with geometry.

After determing that a point is in fact illuminated by the sun (see part 3.2; at these altitudes scattering is negligible), an integration along the line-of-sight is performed (see 2.3 for path length increment used).

Assume a Cartesian Coordinate System with origin at the center of the earth, the Z - axis as the north pole, a vector from the center of the earth to the sun lying in the x-z plane, making an angel α (solar declination) with the X axis (Fig. 3.1). The unit vector to the sun is

$$S = (\cos \alpha, 0, \sin \alpha) \quad .$$

A point P with latitude ϕ and longitude L is located by the vector $P = r\ (\cos\phi \cos L, \cos\phi \sin L, \sin\phi)$ where r is the distance from the center of the earth and L is measured from the X axis. Then the angle between the sun and local vertical at P, γ, is given by

$$\cos \gamma = \frac{P \cdot S}{|P|\,|S|}$$

Starting from P we integrate with step Δs along the line of sight to P' (Fig. 3.1). The new altitude r' is calculated by applying the law of cosines

$$r'^2 = r^2 + \Delta s^2 + 2\Delta s r \cos \gamma$$

The new latitude ϕ' may be found from $P' = P + \Delta s S$, by equating the Z-components and solving to find

$$\phi' = \arcsin\ (\Delta s \sin \gamma + r \sin \phi)\ / r' \quad .$$

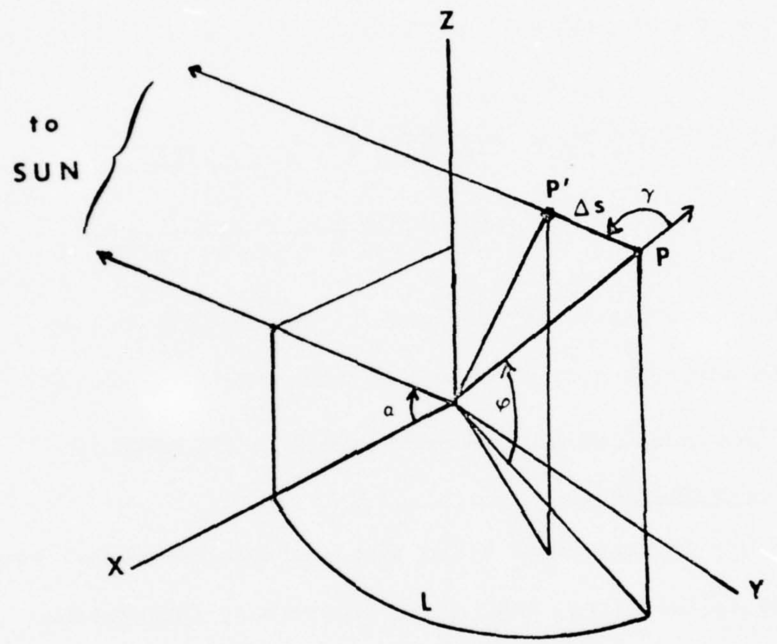

Fig. 3.1 — Geometry of illuminated point

When this calculation is done, using the colatitude $\theta = \frac{\pi}{2} - \Phi$ (and similarly for θ'), $0 < \theta < \pi$, there is no ambiguity in the quadrant of

$$\theta' = \text{arc cos } (\Delta s \sin\gamma + r \cos\theta)/r' \quad .$$

Finally we must find L'. The easiest way to do this (and to be sure of being in the proper quadrant) is to use

$$\tan L' = P_y / P_x = \frac{\cos\Phi \sin L}{\cos\Phi \cos L + \Delta s \cos(\gamma)/r}$$

$$= \frac{\sin\theta \sin L}{\sin\theta \cos L + \Delta s \cos(\gamma)/r}$$

and to find L' using the DATAN2 function of the Fortran Library.

Various criteria for stopping the integration may be used (see 3.3).

3.2 Calculation of Latitude, Longitude Limits. Averaging in Seasonal Calculation.

The cutoff criteria used below have multiple purposes. For the point-wise calculations, they decide whether an integration should be done or whether the point is in the earth's shadow and receives no direct illumination. For the seasonal calculation they determine the duration of heating (relative to 24 hrs.) and control the averaging (discussed below).

A. Latitude Cutoff

To find the latitude above (or below) which all longitudes are dark, we find the ray which grazes the earth at radius r_o (Fig. 3.2a). For this ray $\cos(\beta) = r_o/r$ (Fig. 3.2b, 3.2c); For illuminated latitudes $\cos\beta$ is smaller, while for dark latitudes $\cos\beta$ is larger.

Here

$$\beta = \begin{cases} \theta - |\alpha| & \alpha < 0 \\ \pi - \theta - |\alpha| & \alpha \geq 0 . \end{cases}$$

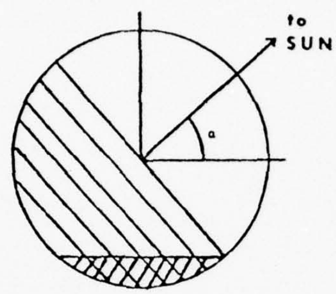

Fig. 3.2(a) — Basic geometry of shadow region. Hatched region is dark. Crosshatched region is dark all day.

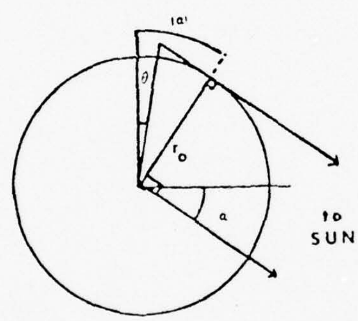

Fig. 3.2(b) — Geometry of dark latitudes for case of northern hemisphere winter

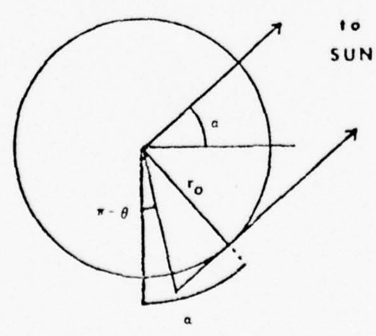

Fig. 3.2(c) — Geometry of dark latitudes for case of noethern hemisphere summer

The possible magnitude of the z/r correction to the cutoff latitude is not negligible. Consider the case $\alpha < o$ ($\alpha > o$ is completely analogous). Let $A = |\alpha|$. Then the cutoff colatitude θ_c is given by

$$\cos(\theta_c - A) = ro/(r_o + z)$$

Then $\sin(|\theta_c - A|) = (1 - 1/(1 + (z/r_o))^2)^{\frac{1}{2}}$

For small z/r_o, the right-hand side of this becomes $\sim (2z/r_o)^{\frac{1}{2}}$ $(1 + \frac{1}{2}\frac{z}{r_o})^{\frac{1}{2}} / (1 + z/r_o)$ or $\sim (2z/r_o)^{\frac{1}{2}}$. For $r_o = 6800$ km, $z \sim 100$ km, $z/r_o \sim .02$ $\sin|\theta_c - A| \sim \sqrt{.04} \sim .2$ and $|\theta - A| \sim 10^\circ$. Note, however, that the line-of-sight to points with colatitudes between θ_c and $|\alpha|$ (or $\pi - \alpha$ for $\alpha > o$) between the sun and a point P, will pass through points with lower altitudes. As the ozone distribution decreases with height (except near mesopause, where the ozone absorption is not large), this effect is somewhat less important for ozone heating, since such glancing lines of sight are usually optically thick due to passage through dense ozone layers below.

B. Longitude Cutoff

Given a partially illuminated latitude, we wish to inquire as to what range of longitudes are illuminated (we measure longitude from 0 at the subsolar point) see Fig. 3.3. We require $|R + \beta S| > r_o$ for all β, for the point $\vec{R}$ to be illuminated, where r_o is the radius of the earth. Let $\Delta^2 = r^2 - r_o^2 > 0$, r the radius of point R. Then for Q $\sin\alpha \cos\theta + \sin\theta \cos\varphi \cos\alpha$, we can have the solution to

$|R + \beta S| = r_o$ $\beta = \frac{1}{2}(-2rQ \pm \sqrt{4r^2Q^2 - 4\Delta^2})$. As β must be real, $4(r^2 Q^2 - \Delta^2) \geq 0$.

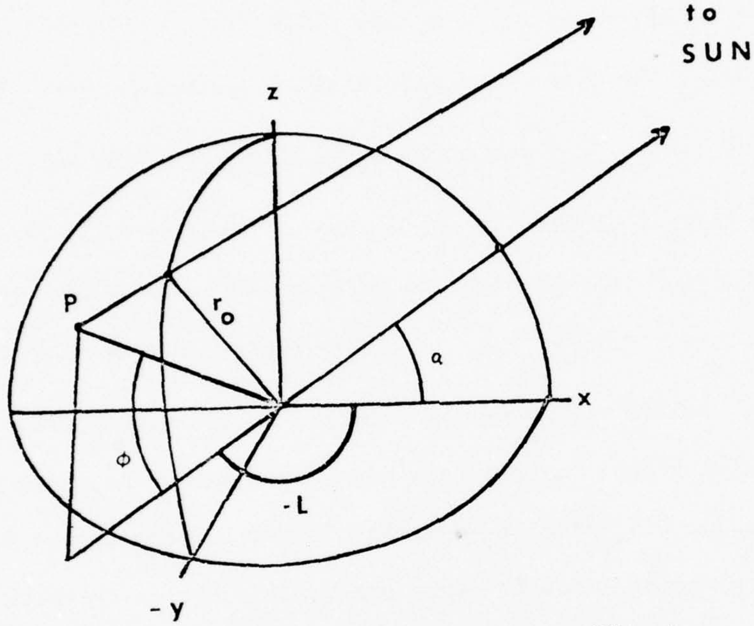

Fig. 3.3 — Geometry of the "longitude cutoff" angle for a given latitude and height

The limiting tangential case is for the equality $r^2Q^2 = \Delta^2$, i.e. $Q = \pm \Delta/r$. The negative root should be used as β must be positive. Consider, for example, an equinoctal case $\alpha = 0$, at the equator ($\theta = \pi/2$). Then $\theta = \cos \varphi_{lim} = \pm \Delta/r$. Clearly we want $\Delta > 0$ to increase the value of φ_{lim} beyond $\pi/2$, and hence the negative sign is mandatory.

Averaging and Sensitivity to Δs.

The seasonal heating is calculated by averaging results at each latitude, for NAV longitudes, equally spaced from 0 (subsolar) to the maximum illuminated longitude φ_m. The daily average heat input is then φ_m/π times this average. One may also use a mean effective longitude,

$$\cos \bar{\varphi} \equiv \frac{\int_0^{\varphi_m} \cos\varphi_o \, d\varphi}{\int_0^{\varphi_m} d\varphi},$$

$$= \quad \sin \varphi_m/\varphi_m$$

in the calculation of γ, and then perform one integration for each latitude and altitude at which heating is desired. Experiments with various cases showed that the results are not very sensitive to the choice of procedure for seasonal heating. The differences are most marked in the lower regions of maximal heating. Here varying NAV from 3 to 4 alters the heating, for typical ozone distribution used (see below), by less than 4%. Using φ_m instead results in difference of the same order, less than 6%; the larger NAV gave slightly smaller heating rates. Varying Δs from 3 to 5 km decreased the heating rates by at most .5%, at the regions of maximum heating (less elsewhere).

The variations above are for a solsticial case; the effects of

altering Δs or the longitudinal averaging is even smaller in equinoctal cases.

3.3 Sample Results: Mean Seasonal Heating Due to Ozone Absorption of Insolation.

The procedures described above were used to find the solar heating due to ozone absorption NAV=3, Δs = 5km were used.

a) Ozone absorption parameters used.

The data for ozone absorption cross section and solar flux were taken from Blake (1973).

We compared the calculated values of "apparent heating",[1] $h\nu\, J_\nu\, n\, d\nu$, to the values given by the analytic approximate formula of Lindzen and Will (1973). The agreement is exact at optical column density (cm NTP) u = .27. For larger u our absorption rates are smaller, e.g. at u = 1 we have 3.23×10^4 ergs $^{-1}$ cm $^{-2}$ (cm NTP^{-1}) compared to 3.5×10^4; the reverse is true for longer path lengths.

b) Ozone Distribution

For altitudes below (pressures above) .8 mb the ozone mixing ratios were taken from the figures of Krueger et al (1973). Table 1c gives the pressure-latitude distribution of ozone mixing ratio in Dobson units, for solstitial and equinoctal northern hemisphere values are 6 mo- different northern hemisphere values. Above the .8 mb height level, theoretical ozone distributions were used (see below).

1. The terms "apparent heating" and "actual heating" are used by Fukuyama (1974b). We use his notation in the integral giving the apparent-actual heating. Here ν is the frequency, h is Planck's constant, n the ozone number density, and $J_\nu(z)$ the photodissociation coefficient (i.e., the product of solar flux at frequency ν and height z, and the absorption cross section at that frequency).

Table 1a

Ozone Mixing Ratio (Dobson Units) as a Function of Latitude and Pressure

WINTER SOLSTICE

NORTH LATITUDE

PRESSURE MB.	0.	20.	30.	40.	60.	80.	90.
0.8	2.0	3.0	3.5	3.7	6.0	7.0	8.0
1.0	4.0	4.0	5.0	5.0	6.0	5.0	4.0
2.0	9.0	10.0	12.0	13.0	13.0	10.0	8.0
4.0	14.0	15.0	15.0	15.0	16.0	10.0	8.0
6.0	16.0	16.0	15.0	13.0	12.0	10.0	8.0
8.0	16.0	16.5	14.0	12.0	11.0	10.0	8.0
10.0	15.0	16.0	12.0	12.0	12.0	9.0	8.0
20.0	11.0	10.0	10.0	9.0	11.0	7.0	5.0
30.0	8.0	8.0	7.5	8.0	10.0	7.0	5.0

Table 1b

Ozone Mixing Ratio (Dobson Units) as a Function of Latitude and Pressure

SUMMER SOLSTICE

NORTH LATITUDE

PRESSURE MB.	0.	20.	30.	40.	60.	80.	90.
0.8	2.0	1.0	1.0	1.0	1.0	1.0	1.0
1.0	4.0	4.0	4.0	4.0	4.0	4.0	3.0
2.0	9.0	9.0	8.0	8.0	8.0	8.0	8.0
4.0	14.0	14.0	12.0	13.0	13.0	8.0	7.0
6.0	16.0	16.0	14.5	13.0	10.0	9.0	8.0
8.0	16.0	16.0	15.5	13.0	10.0	8.5	8.0
10.0	15.0	16.0	16.0	12.0	8.0	8.0	7.0
20.0	11.0	10.0	14.0	11.0	8.0	7.0	6.0
30.0	8.0	9.0	8.0	7.0	8.0	6.0	5.0

Table 1c
Ozone Mixing Ratio (Dobson Units) as a Function of Latitude and Pressure

EQUINOX

NORTH LATITUDE

PRESSURE MB.	0.	20.	30.	40.	60.	80.	90.
0.8	4.0	4.0	4.0	4.0	4.0	4.0	4.0
1.0	4.0	4.0	5.0	4.0	6.0	7.0	8.0
2.0	9.0	9.5	8.0	10.0	11.0	7.0	6.0
4.0	13.5	14.0	12.0	13.0	10.0	6.0	4.0
6.0	16.0	16.5	14.0	12.0	8.0	5.0	3.0
8.0	16.5	16.5	14.5	11.0	8.0	5.0	2.0
10.0	16.0	16.5	14.5	10.0	8.0	4.0	1.0
20.0	11.0	12.0	12.0	8.0	8.0	3.0	1.0
30.0	8.0	8.0	7.7	8.0	8.5	8.2	7.5

Heating functions were computed with the infrared radiative cooling parameterization of Dickinson (1973). This approximation becomes poor above a 65 km but nothing better is currently available. Below 30 km the relaxation rate is taken as fixed and equal to the rates at 30 km. The cooling (to space) term is taken to behave as $c(70) \exp[-(Z-70)/8]$ z in km., above 70 km.

The relaxation rate due to ozone photochemistry is an additional contribution to the thermal relaxation rate. It is calculated following Leovy (1964). Comparison with the work of Blake (1970), however a more detailed reaction rate set, is quite favorable. This contribution to k_R, K_{O3}, is proportional to the local ozone heating. Then $k_R = K_{O3} + K_{IR}$, K_{IR} found from Dickinson (1973) as described above.

The ozone heating is found using the program discussed above. Below 50 km the ozone distribution used is that of Kreuger et al. (1972).

above 50 km, the values are from Crutzen (1971) for the summer and Fukuyama (1974a) for the winter. For equinox a latitudinally independent distribution that was intermediate between winter and summer values was used. Contours of these distributions are shown in Figs. 3.2a and 3.3a.

In computing the heating rate above 70 km the heating function (Fukuyama 1974b) is used and is assumed proportional to $n(h\nu - E - D) J_\nu d_\nu$ where E,D are excitation and dissociation energies. Below 70 km we use an "apparent" heating rate, assuming that the chemical energy is locally converted to thermal energy. Clearly the transition between these limiting cases is not so abrupt, but this is adequate for our calculation. The resultant heating rates are shown in Figs 3.4b, 3.5b. Note the "island" of heating in the upper low-latitude winter hemisphere due to large O_3 density. There is a relative maximum of heating at the summer pole $\sim$85 km which is not seen due to the contour interval. Combined with an assumed $T_o(Z)$ (COSPAR 1961) the infrared transfer parameterization described above gives the net heating/cooling rates shown in Figs 3.4c, 3.5c. The thermal relaxation rates, Figs. 3.4d, 3.5d are also found as described above. Using k_R and the net heating Q, a radiative equilibrium temperature may be found, as in Figs. 3.4e, 3.5e. The solstitial results are closer to the profile assumed by Trenberth (1973), than that of Leovy (1964a); Leovy's results evidence much colder winter pole values.

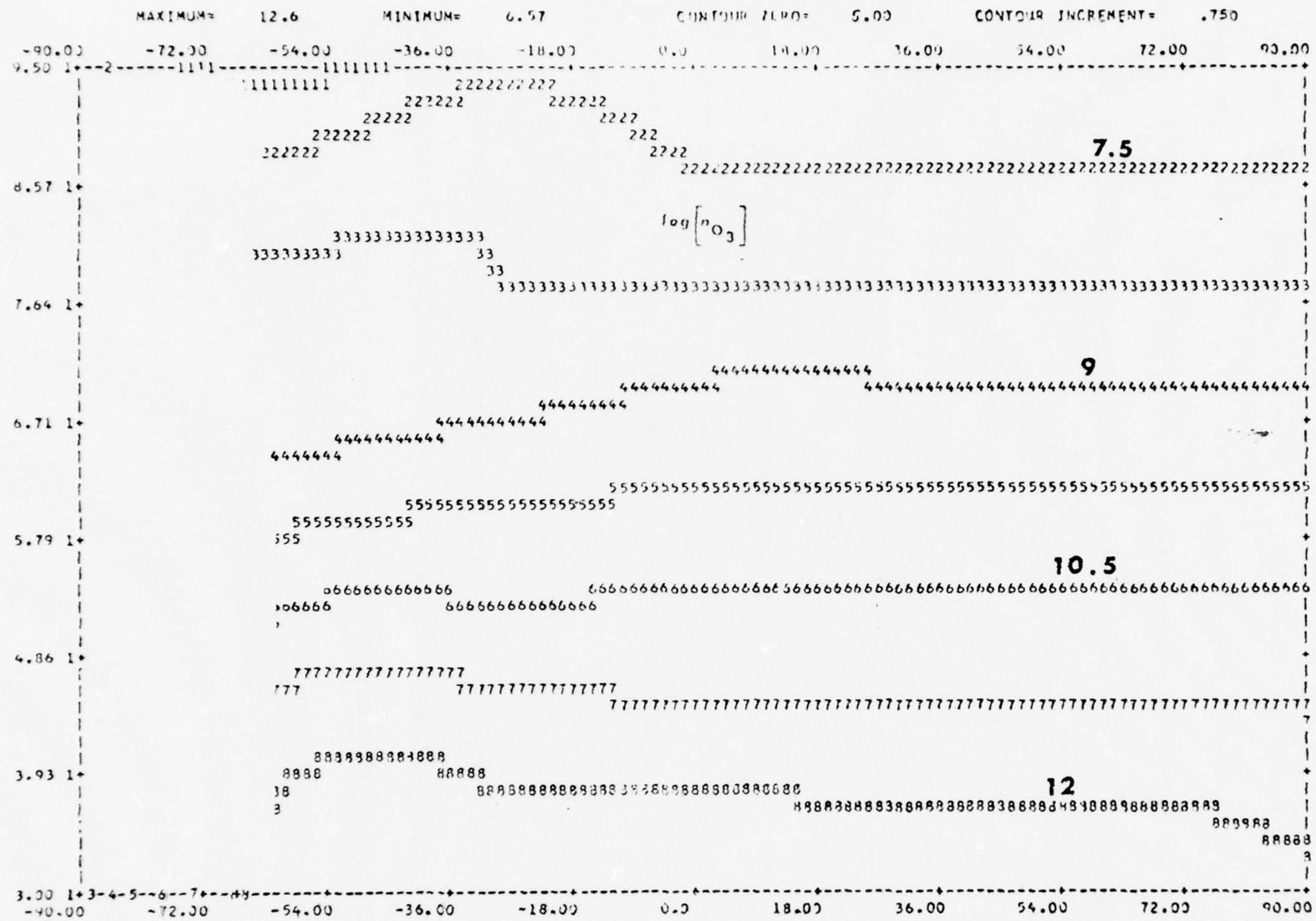

Fig. 3.4(a) — Contours of ozone number density assumed-solstice

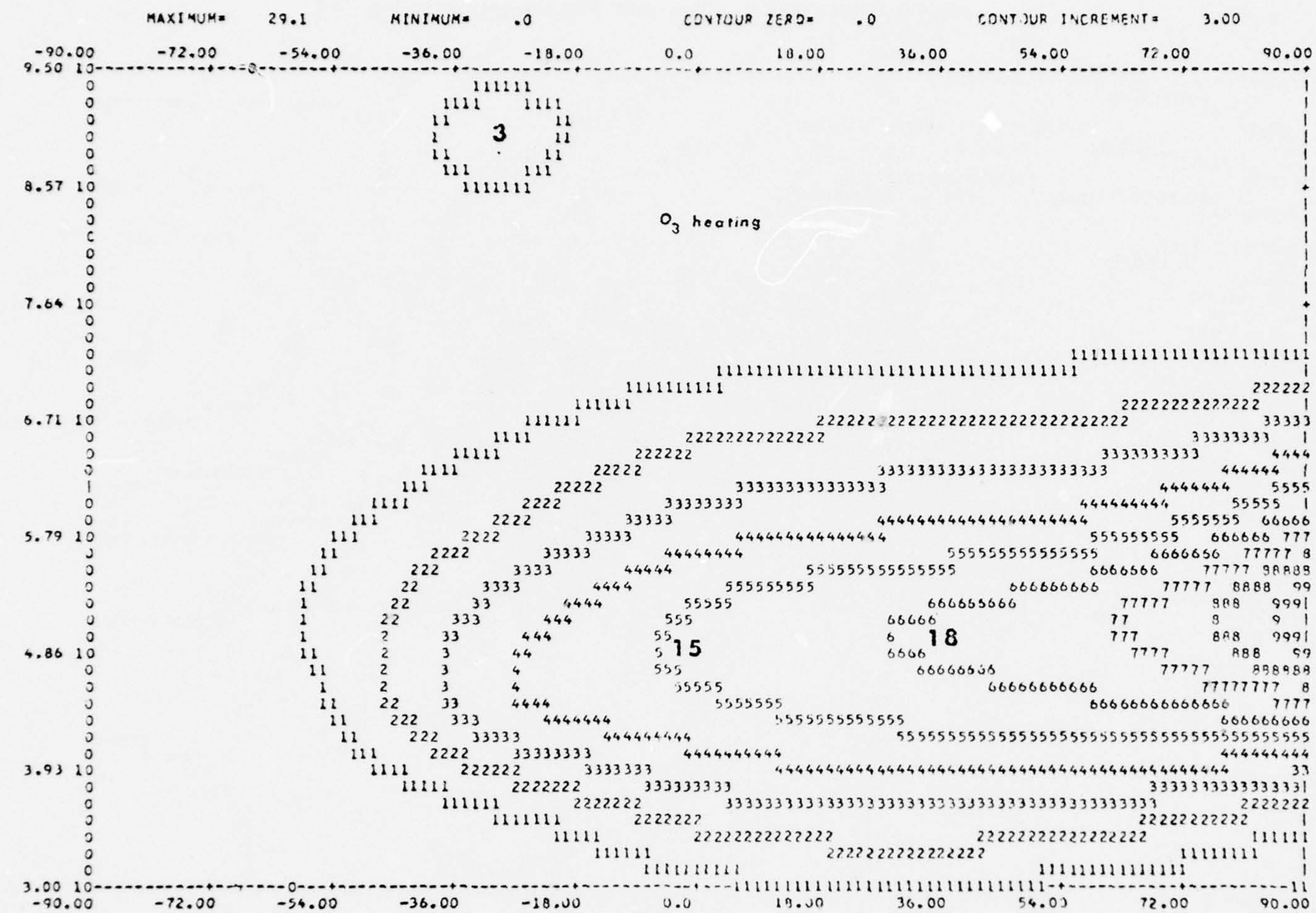

Fig. 3.4(b) — Resulting heating rate due to insulation, in degrees day^{-1}

Fig. 3.4(c) — Net heating including infrared radiative transfer

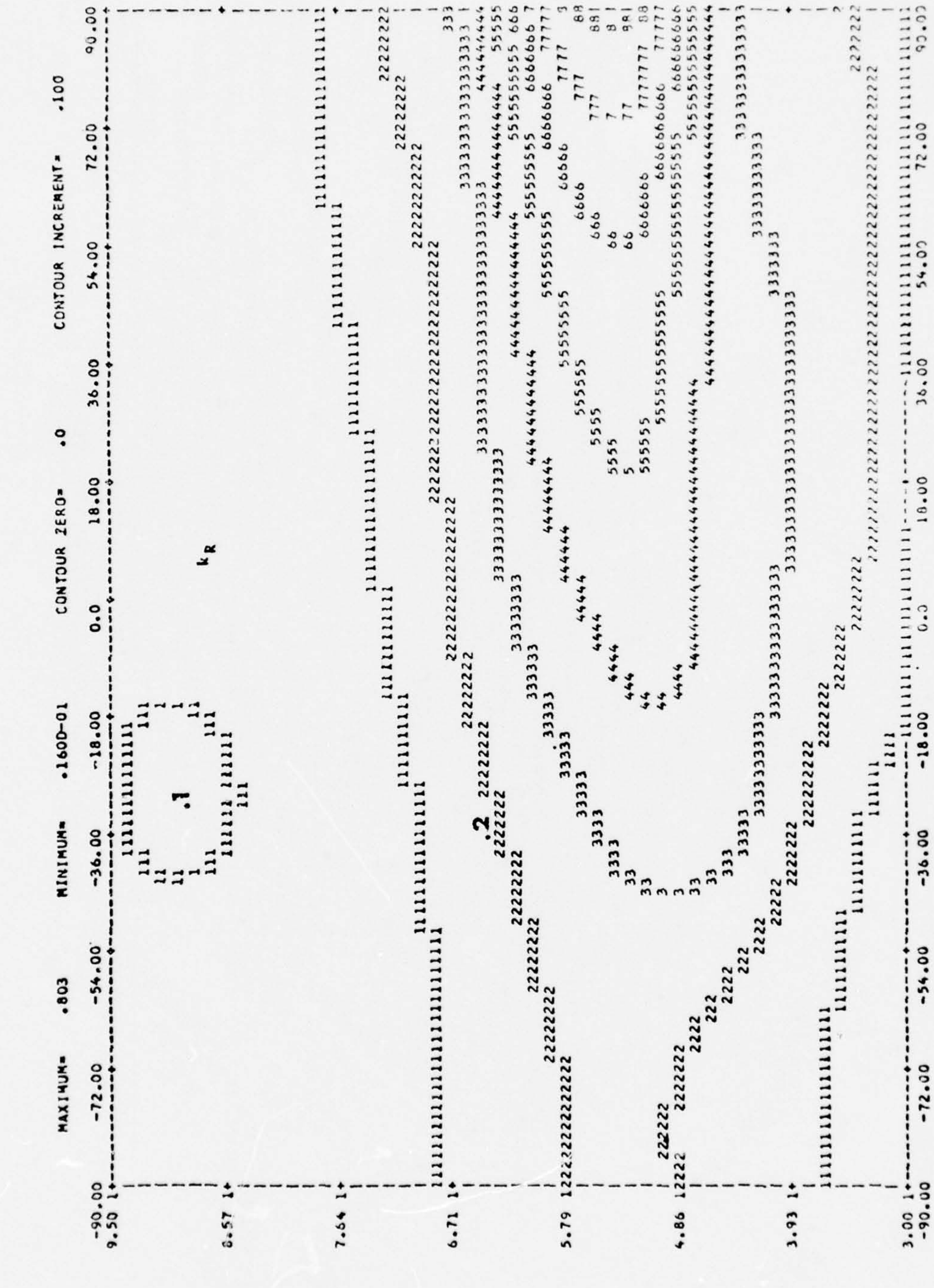

Fig. 3.4(d) — Thermal relaxation rate, day^{-1}

Fig. 3.4(e) — Radiative equilibrium temperatures

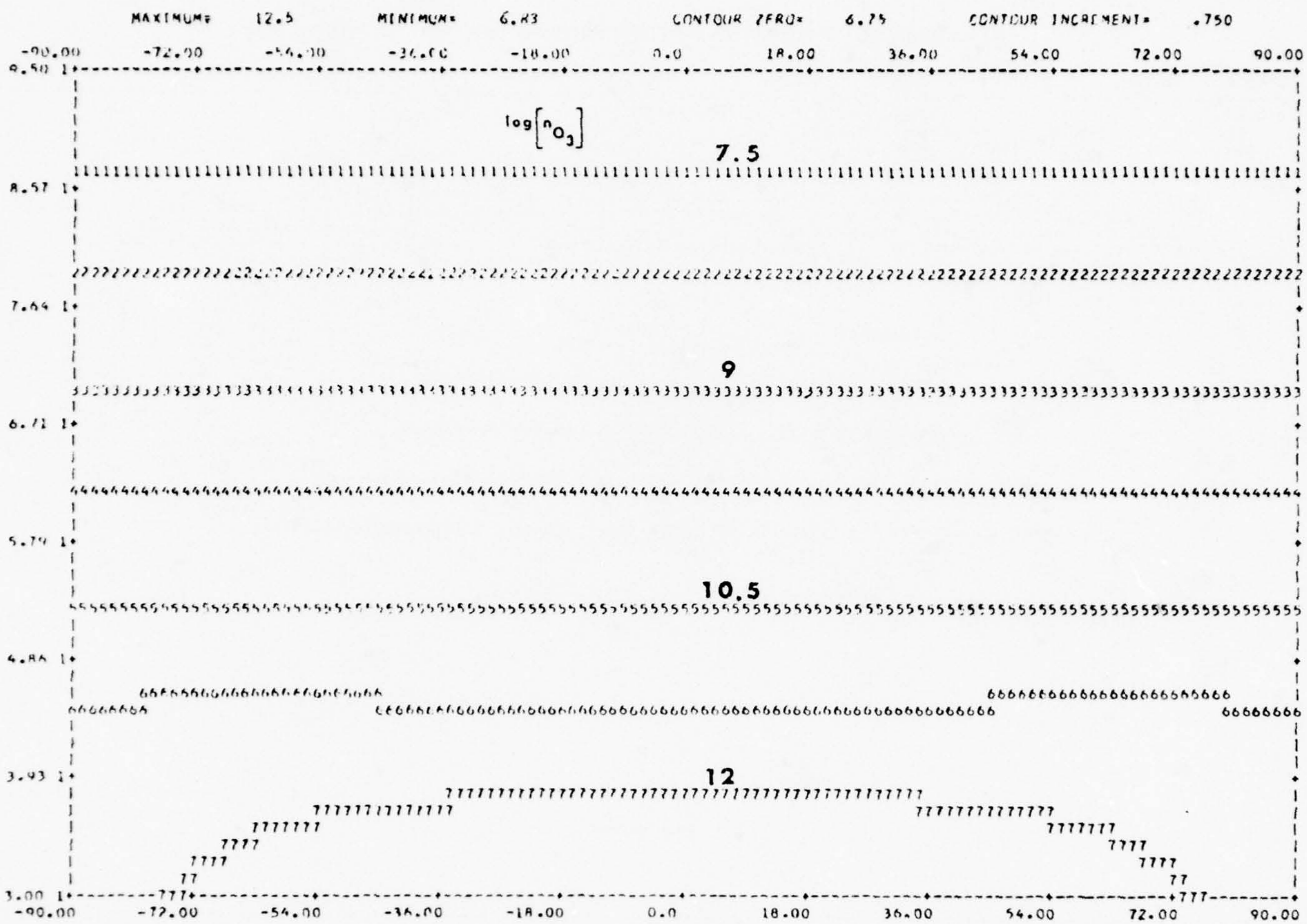

Fig. 3.5(a) — Contours of ozone number density assumed - equinox

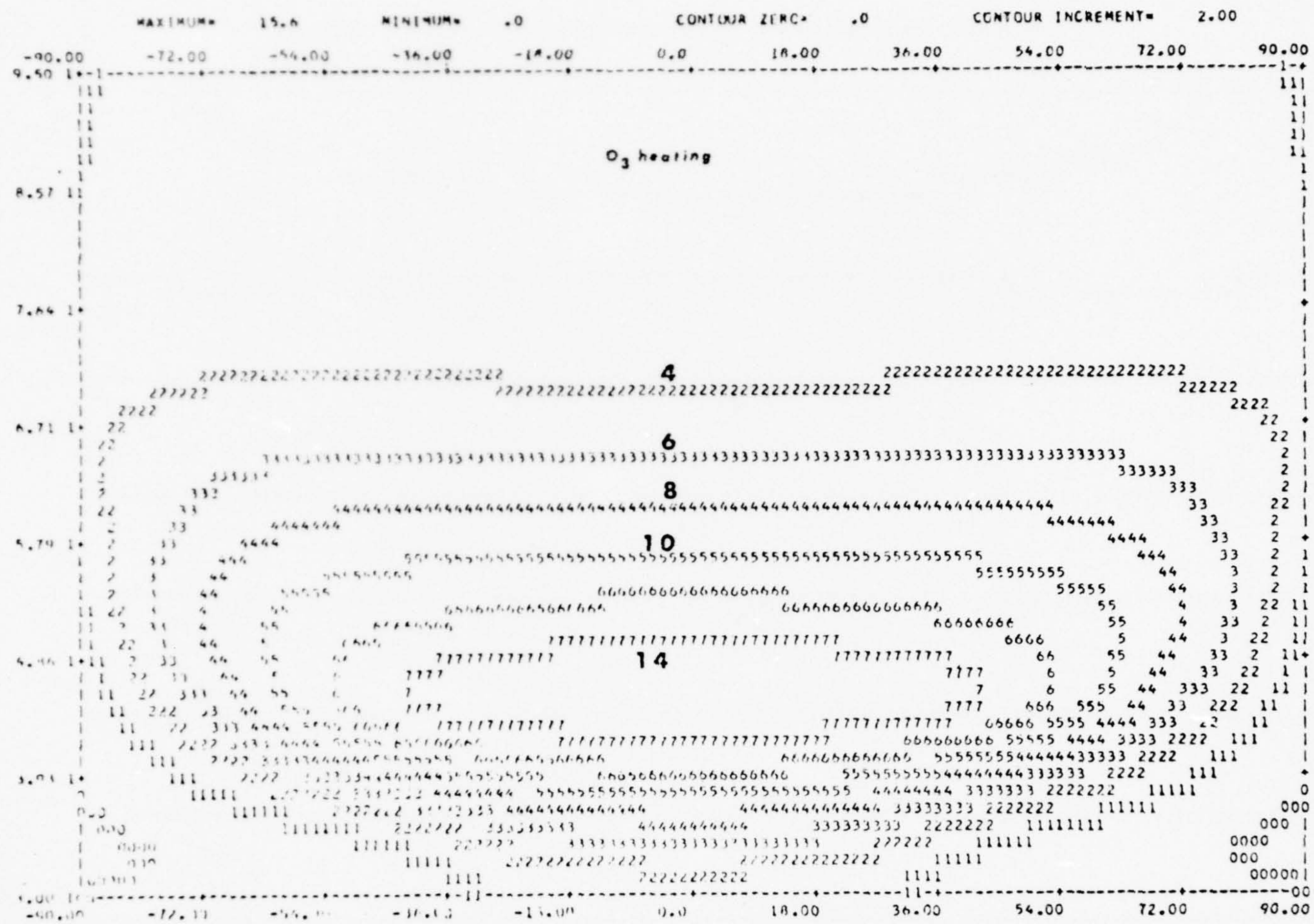

Fig. 3.5(b) — Resultant heating rate due to insulation in degrees day^{-1}

Fig. 3.5(c) — Net heating, including infrared radiative transfer

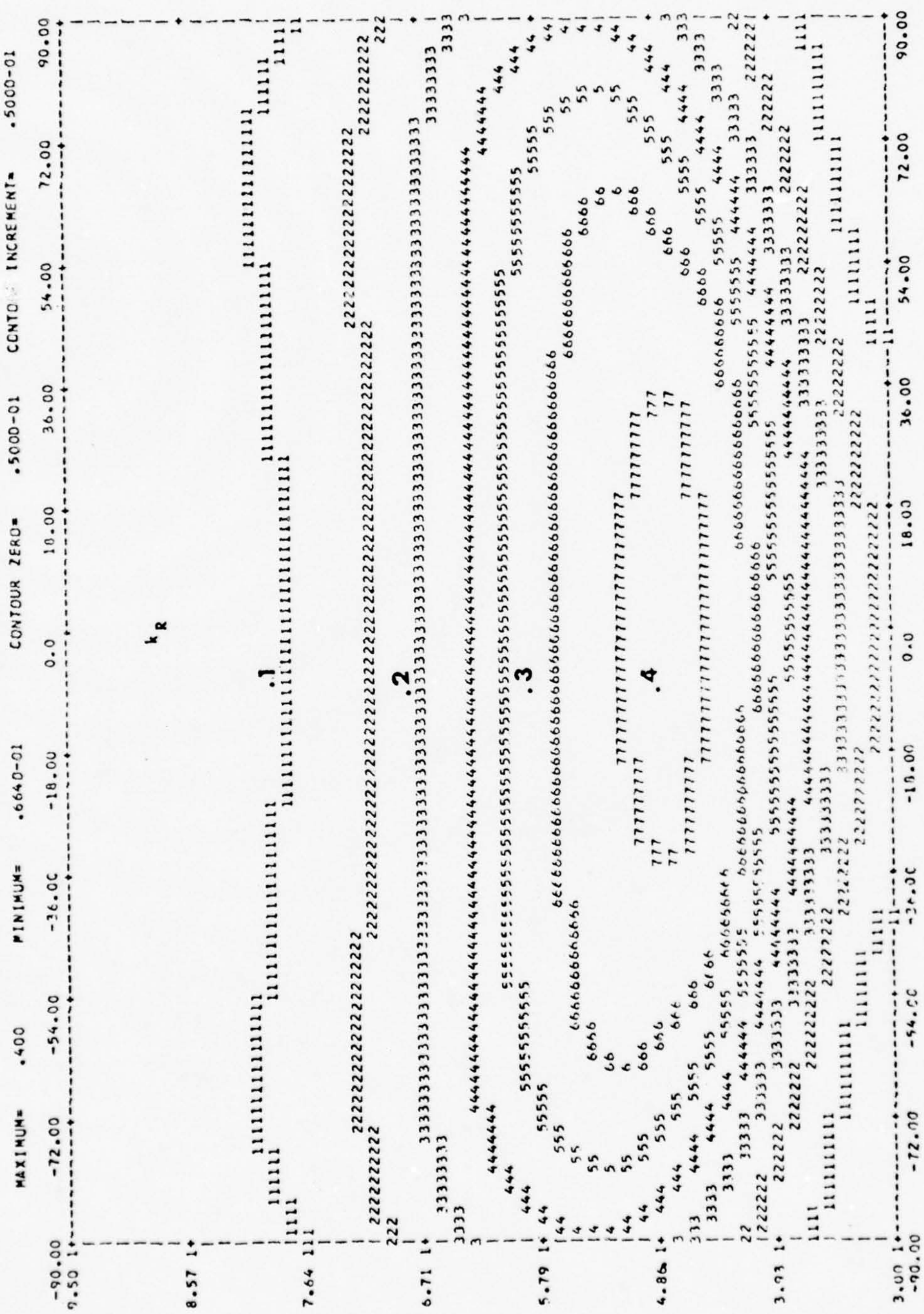

Fig. 3.5(d) — Thermal relaxation rate, day^{-1}

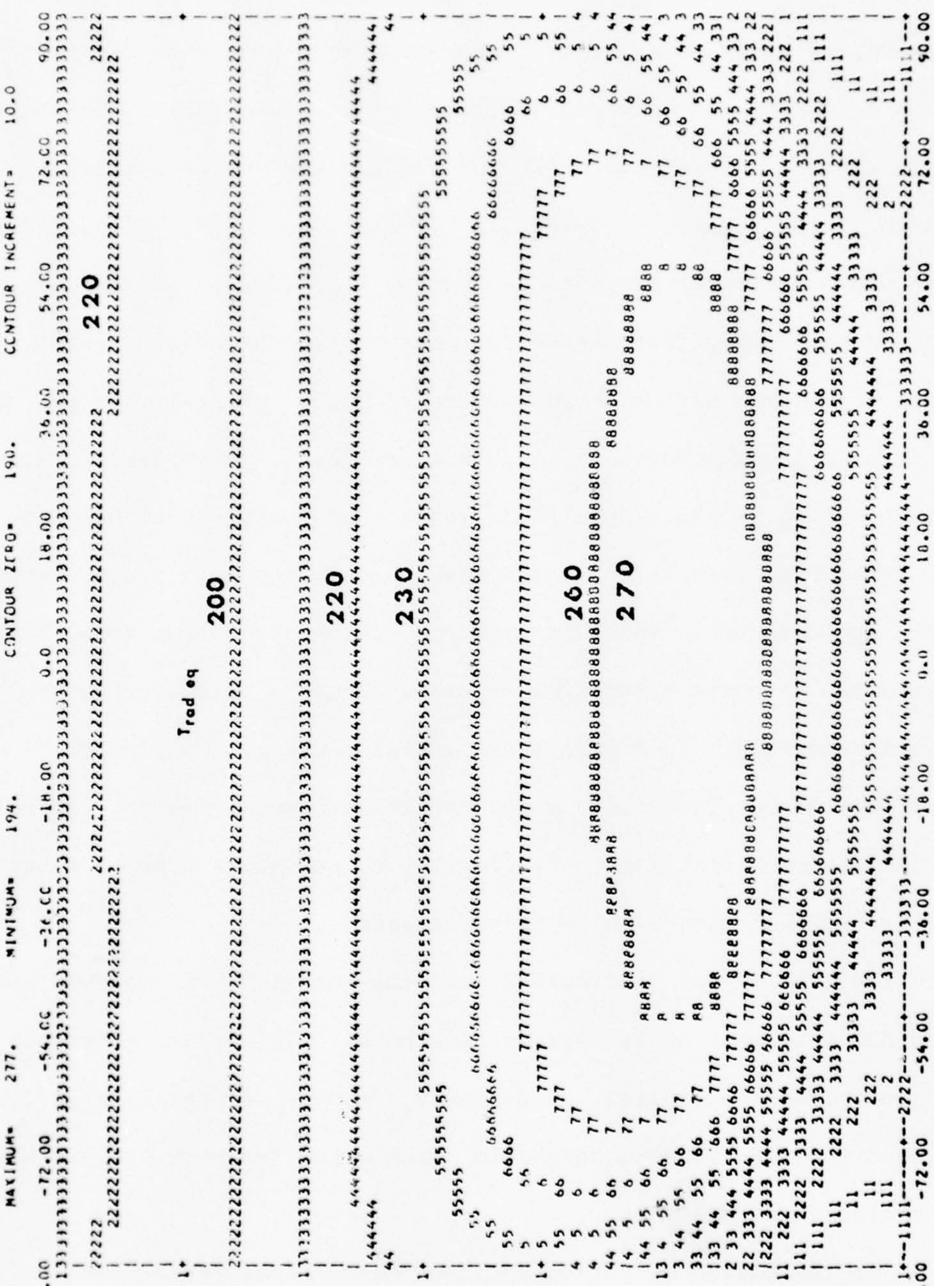

Fig. 3.5(e) — Radiative equilibrium temperatures

3.4 Application of the Heating Function & Models of the Mesospheric Circulation.

In a previous report (Baker and Strobel, 1975; hereafter referred to as Report I) we constructed linear separable models to describe the mean circulation of the upper stratosphere and mesosphere. This circulation can have a profound effect on radioactive debris patches created by high altitude nuclear explosions (Zalesak and Coffey, 1975). The subsequent beta decay results in long lasting, widespread ionization that can severely affect the performance of communication systems. Accurate prediction of system performance depends critically on our ability to describe the movement of debris patches by mesospheric wind systems, of which the mean circulation is one important component.

Accurate simulation of the mean circulation in the upper stratosphere and mesosphere which is primarily driven by differential radiative heating due to ozone absorption requires accurate parameterization of radiative heating. In Report I the emphasis was on the importance of other parameters, particularly the Newtonian (radiative) cooling rate and the Rayleigh friction coefficient. The radiative heating functions of Leovy (1964a) were used in the calculation.

In this report we describe calculations with the improved heating functions described above and the Dickinson (1973) parameterization of infrared radiative cooling. Our improved models accurately simulate the observed mean zonal mesospheric circulation for both solstitial and equinoctial conditions.

In the course of our research we have discovered a number of inconsistencies in the Leovy (1964a,b) heat functions. Briefly the

inconsistencies of Leovy (1964a,b) relate to the assumed equilibrium, basic state of the atmosphere (mean density, pressure, temperature, and wind fields) and the corresponding differential heating functions which are temperature dependent. For example, any latitudinal variation in the equilibrium basic temperature field requires a corresponding zonal geostrophic wind to describe the equilibrium state of the atmosphere. This zonal geostrophic wind was ignored in some of Leovy's models.

The ozone heating rate, $Q(\pi,\varphi)$, where π is the vertical coordinate (log pressure coordinates, see Report I) and φ is latitude, is computed for an assumed ozone density distribution as described above. The infrared radiative cooling rate is based on Dickinson's (1973) results. The thermal relaxation rate, $k_R(\pi,\varphi)$ is given by the sum of the IR cooling rate and the ozone photochemical damping rate calculated by Leovy (1964b) and is consistent with the results of Blake (1973).

Given the functions $Q(\pi,\varphi)$ and $k_R(\pi,\varphi)$ we can compute the latitudinally averaged values of k_R, denoted by $\langle k_R(\pi)\rangle$ and expand the heating function in a modal representation

$$Q(\pi,\varphi) = \sum_m \frac{d\eta_{m(\varphi)}}{dy} Sm(\pi) \tag{3.1}$$

as defined in Report I and where y - sin φ. We calculate $Sm(\pi)$ by the usual technique of assuming the expansion form (1) and use the orthogonality of the $\frac{d\eta_m}{dy}$ functions. These functions were evaluated at each π level of the model. Two modes were required for solstitial conditions whereas only one mode sufficed for equinoctial conditions. Their numerical values are shown in Figs. 3.6 and 3.7 respectively.

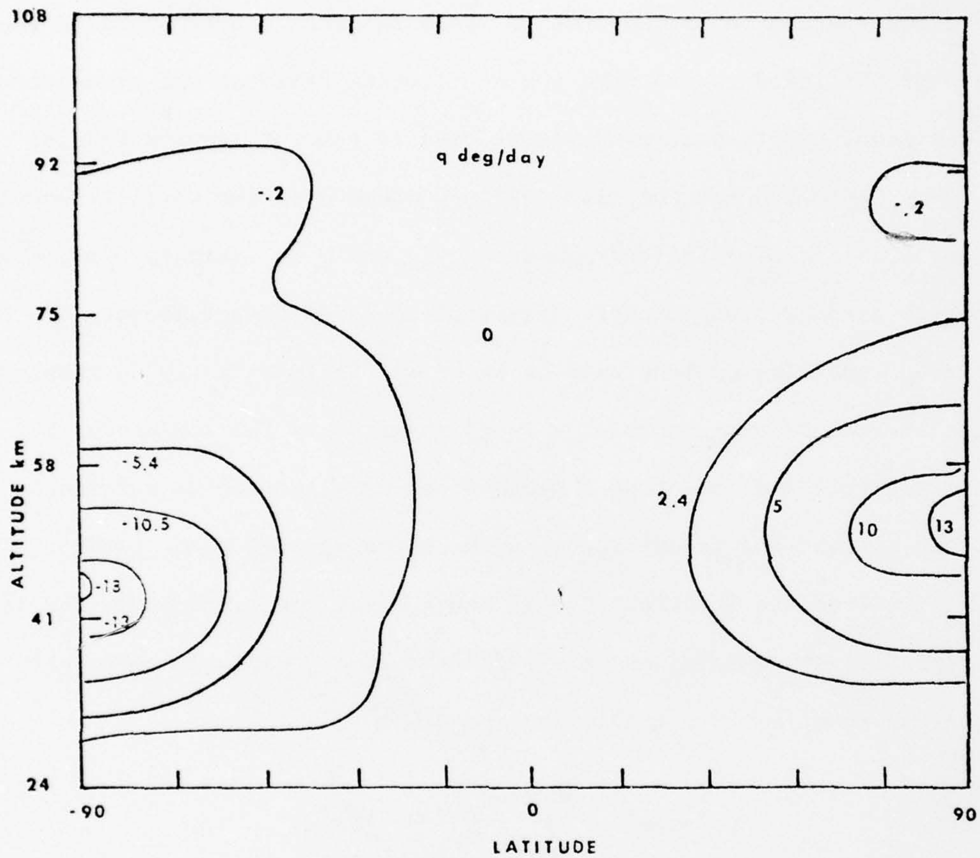

Fig. 3.6 — Isopleths of heating function (°K day^{-1}) used in solstitial model, plotted against latitude and altitude

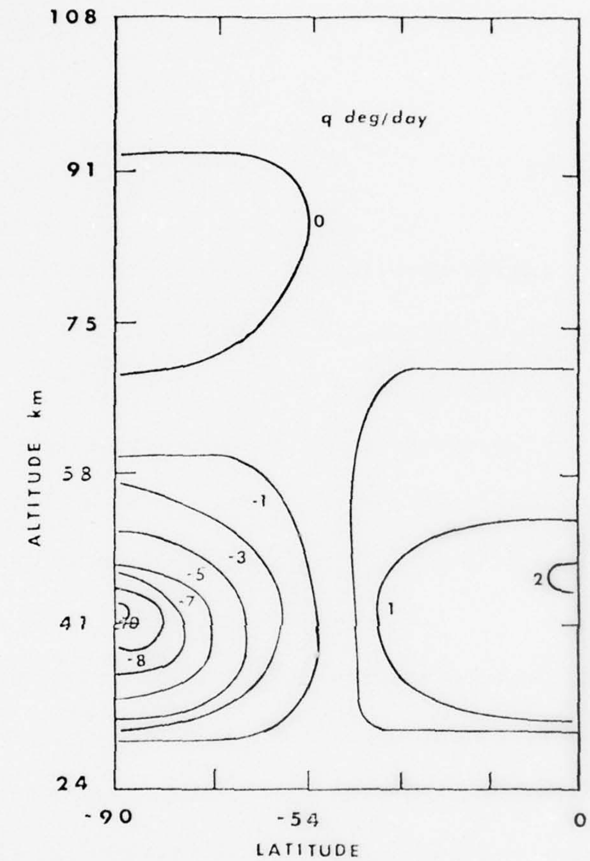

Fig. 3.7 — Isopleths of heating function (°K day^{-1}) used in equinoctial model, plotted against latitude and altitude

For equinoctial conditions the latitudinal average of $k_R(\pi,\varphi)$ weighted by $\cos\varphi$ to account for surface area variation with latitude was used for $\langle k_R(\pi)\rangle$. For solstitial conditions it is necessary to insure the correct total thermal forcing that drives the circulation. In radiative equilibrium

$$T_{eq}(\pi, \pm 90^\circ) = T_0(\pi) + \frac{Q(\pi, \pm 90^\circ)}{\langle k_R(\pi)\rangle}$$

where T_{eq} is the radiative equilibrium temperature and T_0 its mean value. The pole to pole temperature difference

$$\Delta T_{eq} = [Q(\pi, +90^\circ) - Q(\pi, -90^\circ)]/\langle k_R(\pi)\rangle$$

determines $\langle k_R(\pi)\rangle$. These values for $\langle k_R(\pi)\rangle$ were slightly smaller ($<10\%$) than the "weighted" mean $k_R(\pi,\varphi)\cos\varphi$. In addition the weighted arithmetic $\langle k_R \cos\rangle$ and harmonic $\langle (k_R^{-1}\cos\varphi)\rangle^{-1}$ means differ only slightly.

The mean temperature profile $T_0(\pi)$ and the corresponding static stability parameter $R_s(\pi)$, a function of $T_0(\pi)$ and $\frac{dT_0}{d\pi}$, must be consistently selected. Based on the CIRA (1961) mean temperature profile, the corresponding height profile of $R_s(\pi)$ is illustrated in Fig. 3.8. The Rayleigh friction coefficient, R_F, was taken to be 1.5×10^{-6} sec^{-1} in accord with other models.

The model results for solstitial conditions are shown in Figures 3.9a -3.9d. We note from Fig. 3.9a that the model predicts zonal jets of approximately correct velocities and at the observed heights. For example Murgatroyd (1970) gives observed peak velocities of 80 m sec^{-1} for the winter jet and -60 m sec^{-1} for the summer jet. The winter jet

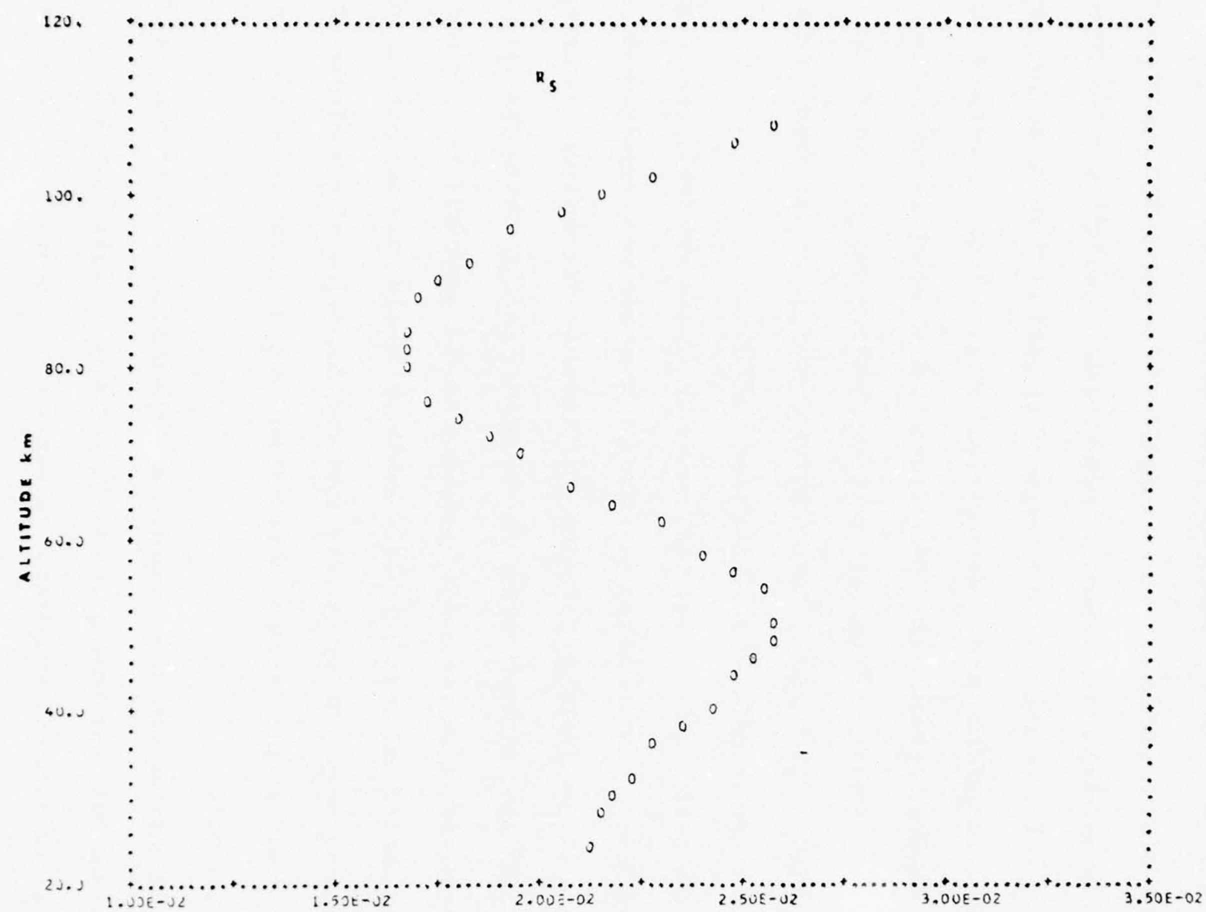

Fig. 3.8 — Assumed static stability parameter, R_s, as a function of altitude, from CIRA 1961

is centered approximately 10 km below the summer jet and they are not on the same geopotential surface. We expect this result due to the added symmetric heating mode which forces an asymmetric zonal velocity field. The fact that the resultant zonal velocity field is in good agreement with observations would suggest that a symmetric component of heating is an essential element of mesospheric circulation at solstice.

At solstice the winter mesosphere is predicted to be approximately isothermal in agreement with observations (Fig. 3.9b). No attempt was made to accurately model the lower stratosphere, which is controlled by tropospheric forcing. Thus the predicted temperature minimum at the winter pole is 30° K colder than observed, whereas at the summer pole the difference is only 5° K (Murgatroyd, 1970).

The meridional and vertical velocity fields are small (cf. Figures 3.9c and 3.9d). As discussed in Report I they are very sensitive to the magnitude of the Rayleigh friction coefficient. The vertical velocities (Fig. 3.9d) show sinking motion at the winter pole at twice the rate of the rising motion at the summer pole due to the symmetric heating mode. Also the meridional velocity field exhibits similar asymmetries due to this heating mode. We anticipate that the inclusion of non-linear advection would result in reduced meridional and vertical velocities at the winter pole.

At equinox the model results are symmetrical with respect to the equator and only one hemisphere is illustrated in Figs. 3.10a-3.10d. The zonal jet velocity is comparable in magnitude to solstitial conditions, but are accompanied with peak meridional winds only one-half as strong as at solstice. The poleward, symmetric about the equator, motion re-

sults in a "2 - cell" circulation rather than the predominate 1 - cell circulation at solstice. At midlatitudes the equinoctial results for zonal wind and temperature are in good agreement with observations. However at the equator, where the quasi-geostrophic assumption breaks down, there are observed zonal jets ~ 40 m sec^{-1} not predicted by our model.

3.5 Conclusion

Linear zonally symmetric models can accurately simulate the observed zonal wind and temperature fields particularly at mid and high latitudes. Based on realistic values for the Rayleigh friction coefficients we predict peak vertical velocities of 0.3 - 0.6cm sec^{-1} at the poles during solstice and equinox. The peak mean meridional velocities occur at midlatitudes and are $\leq$ 1m sec^{-1}.

It should be noted that only ozone heating was included in our model. The next step is to investigate the importance of atmospheric heating due to molecular oxygen absorption in the Schumann-Runge bands above ~ 70km on mesospheric circulation. In addition the non-LTE effects on the infrared radiative cooling rate, neglected in the Dickinson (1973) parameterization must also be evaluated. These sources and sinks of heat energy tend to offset each other. We do not anticipate that the inclusion of these processes will dramatically alter the results presented in this report. At equinox the physics of the equatorial jets must be included for accurate simulation in the equatorial regions of the mesosphere.

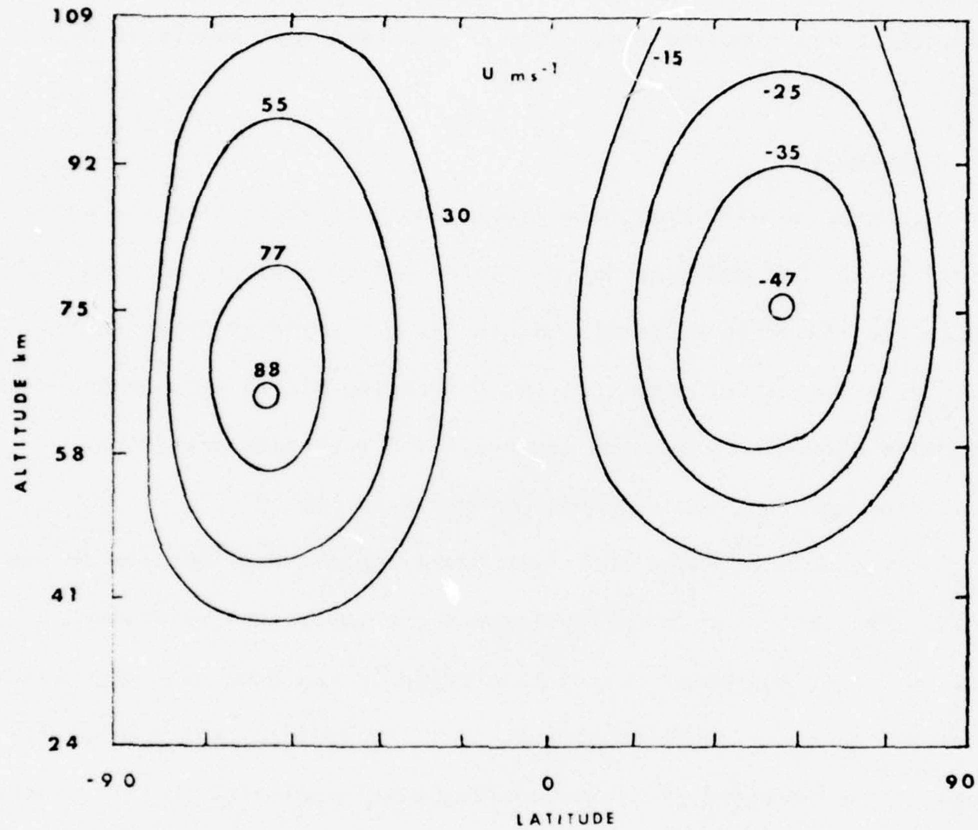

Fig. 3.9(a) — Isotachs of u, m s^{-1}

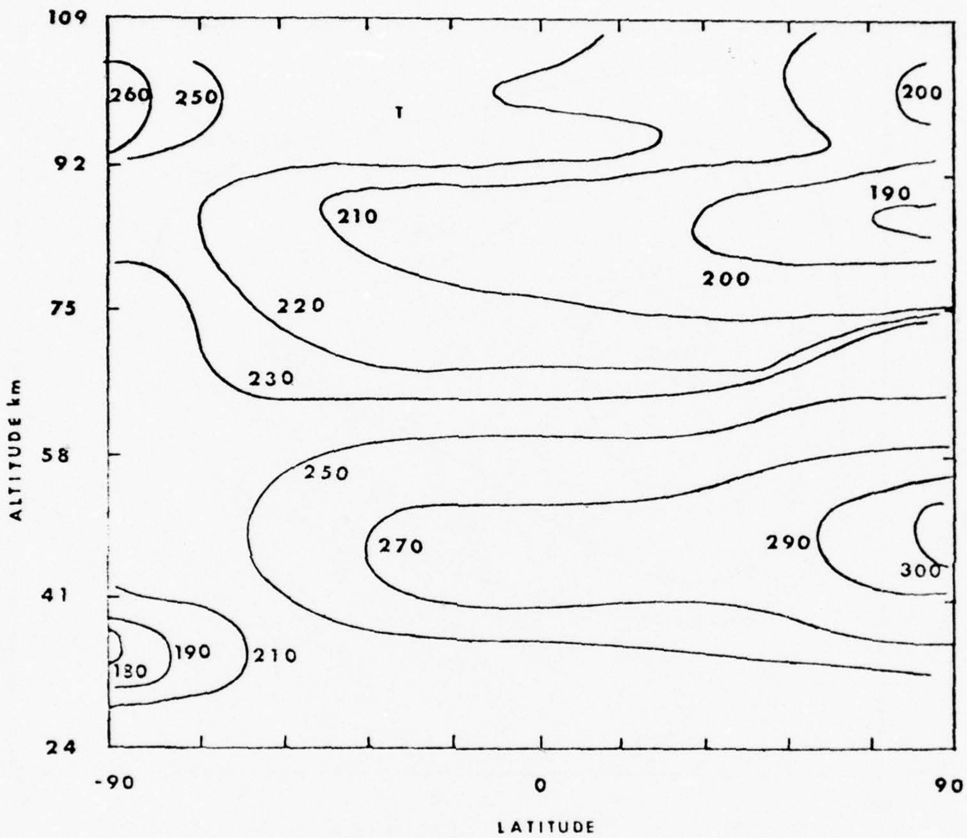

Fig. 3.9(b) — Isotherms of T, °K

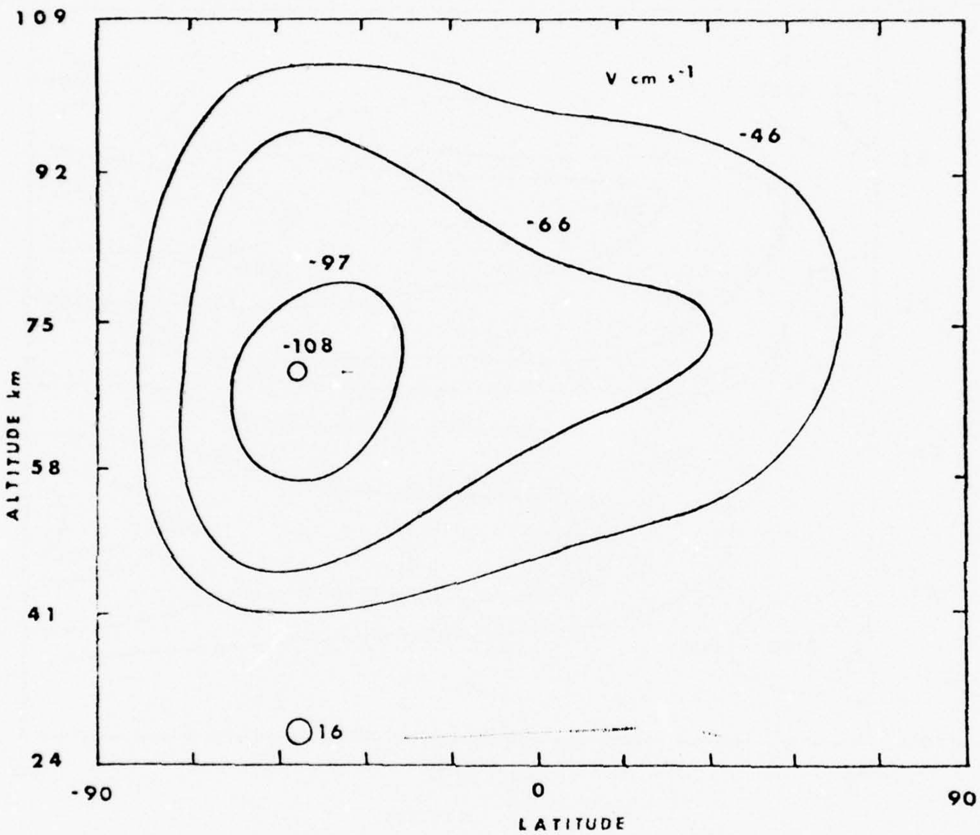

Fig. 3.9(c) — Isotachs of V, cm^{-1}

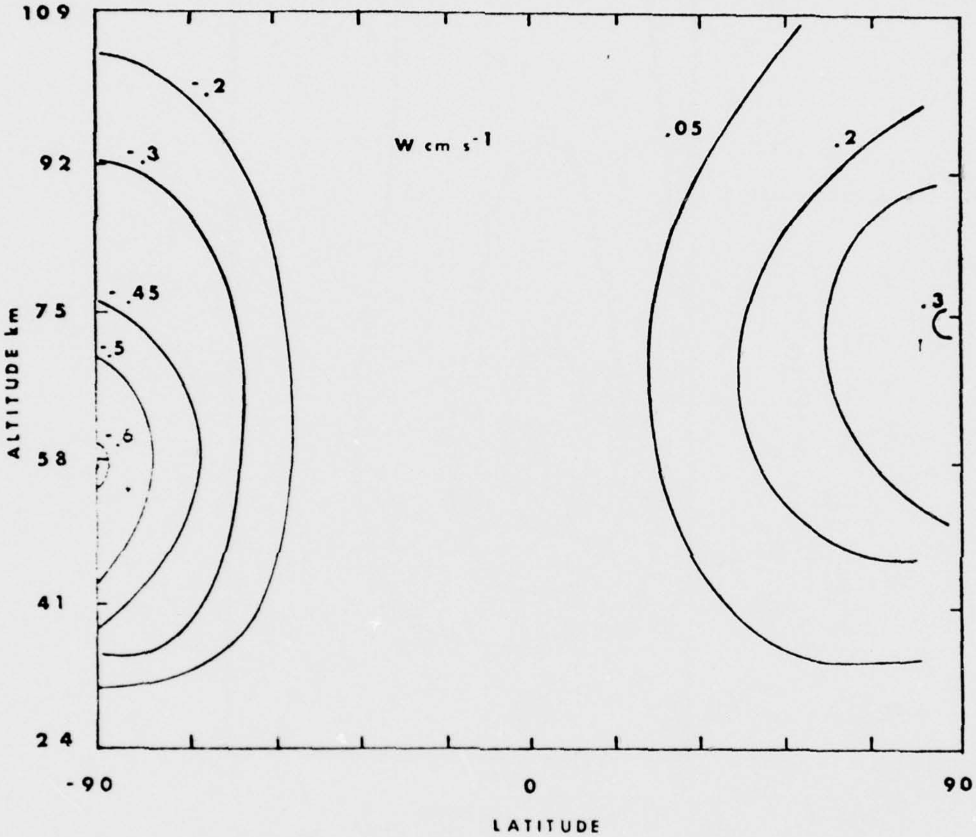

Fig. 3.9(d) — Isotachs of W, cm^{-1}

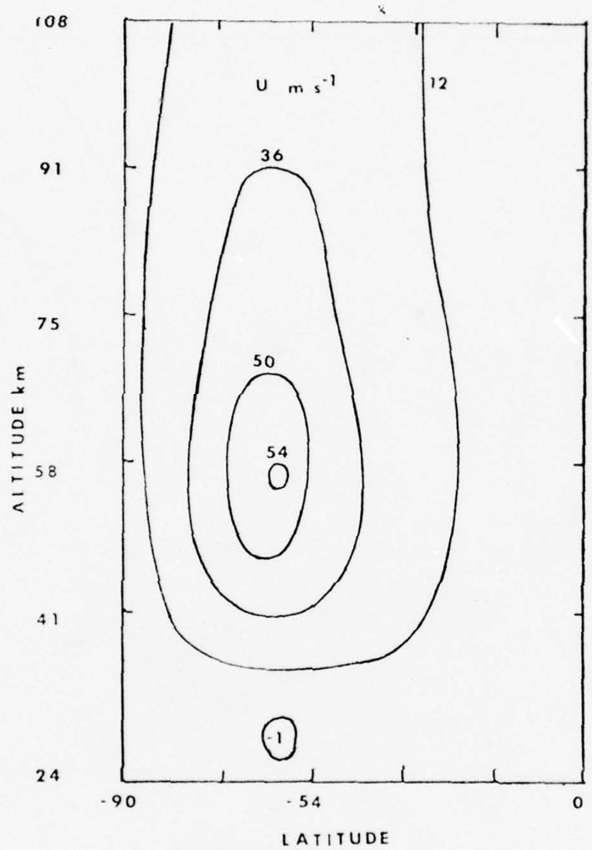

Fig. 3.10(a) — Isotachs of u, m s^{-1}

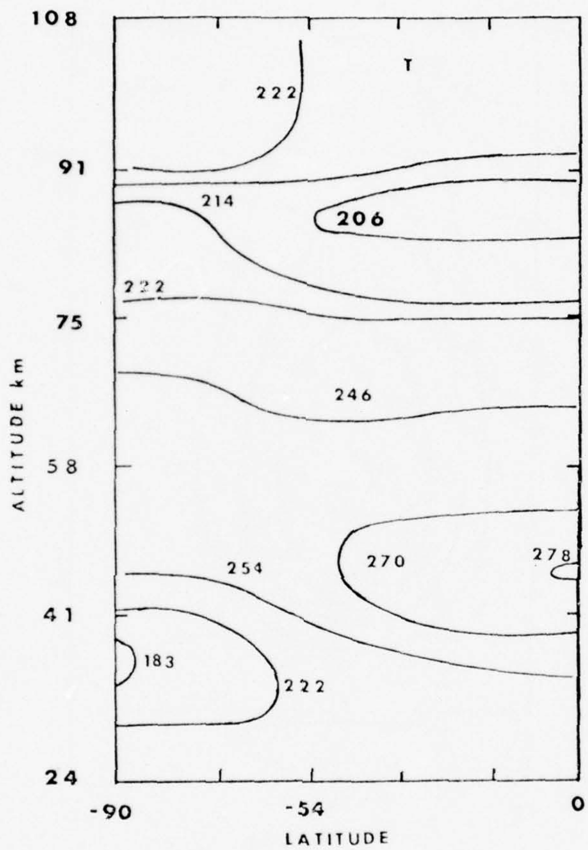

Fig. 3.10(b) — Isotherms of T, °K

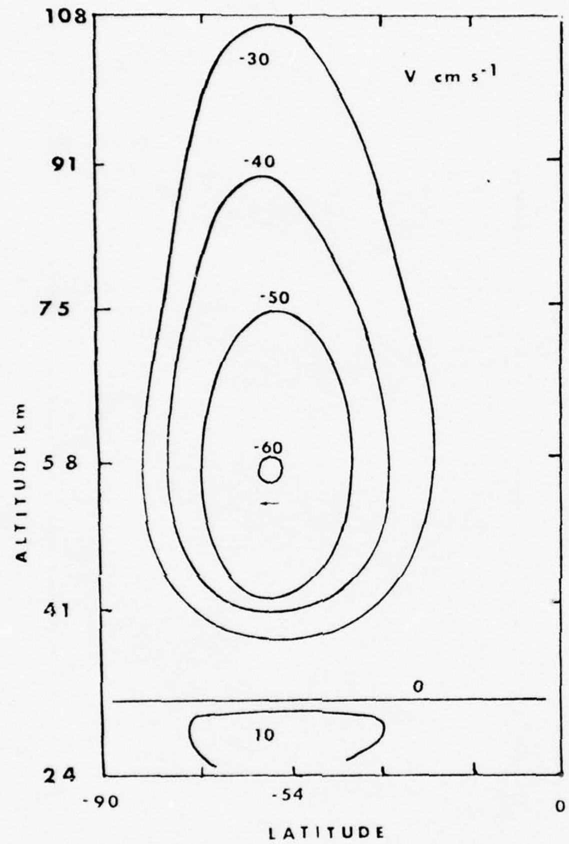

Fig. 3.10(c) — Isotachs of V cm^{-1}

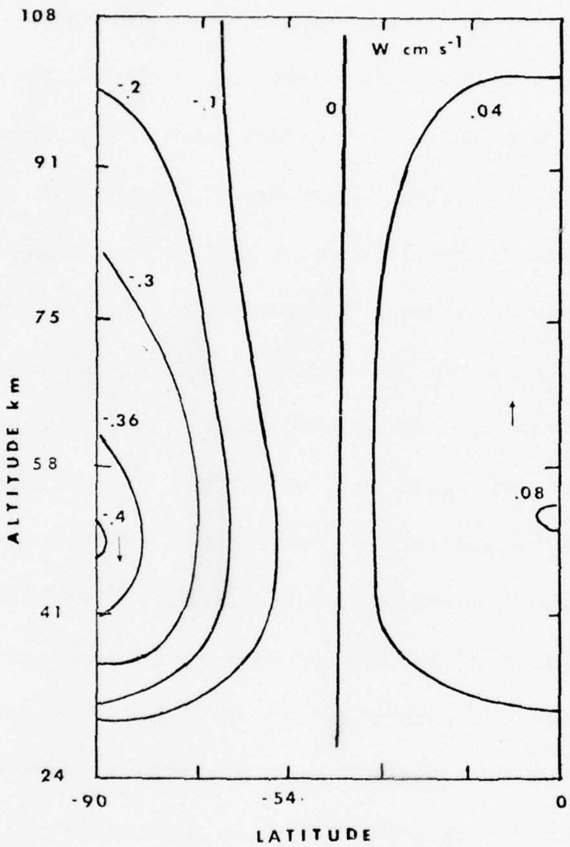

Fig. 3.10(d) — Isotachs of W, cm^{-1}

Section 4

A SEMI-SPECTRAL NUMERICAL MODEL FOR FORCED, VERTICALLY PROPAGATING PLANETARY WAVES

Part I-Application of the Model to Linear Diurnal and Semi-Diurnal Atmospheric Thermal Tides

R.V. Madala, S.A. Piacsek, and S.T. Zalesak

The study of non-linear interactions of forced planetary waves with one another and with the mean current can best be treated as a time dependent initial-value problem. However, this approach suffers from the disadvantage that some of the free modes of the atmosphere will be excited besides the desired response to a particular forcing, due to inaccurate initial conditions. As shown by Lindzen et al. (1968) the numerical models also suffer from another disadvantage in that the vertically propagating modes are reflected back by a rigid or inaccurate upper boundary, leading to change in the structure of these waves.

Yanowitch (1969) and Houghton and Jones (1969) have investigated the vertical propagation of gravity waves in isothermal atmospheres, and studied the reflection and absorption of these waves by an exponentially increasing friction profile and Rayleigh viscosity, respectively. Hong and Lindzen (1973) have simulated the tides numerically in the presence of a geostrophic mean wind, but obtained convergent results only for the semidiurnal tide. In each of these studies, only sinusoidal waves of the form $e^{i\omega t}$ were considered, leading to an eigenvalue problem of ordinary differential equations in the height z. The gravity wave studies were concerned only with plane geometry, whereas the tidal studies involved spherical harmonics and treatment of the poles; on the other hand, the latter did not include the formation of critical layers (i.e., where

the phase speed of the wave equals the wind speed at that level), because both the 24 and 12 hour tides propagate around the Earth much faster than any wind can move.

The main thrust of the present paper is to utilize the information derived by the foregoing studies on vertical propagation and reflection, and to consider the alternate method of asymptotically reaching a quasi-steady oscillatory state of forced motions via initial value, time-dependent methods. This seemed to be desirable not only to avoid the difficulties associated with inverting the diurnal matrix, but to formulate more general techniques for non-linear problems. The tides were deemed an ideal problem to test the linear version of the model, since both analytical and numerical (at least for semi-diurnal tide) solutions are available.

The disadvantages mentioned earlier are circumvented in this model by introducing a transient Rayleigh friction (decaying in time) to get rid of the unwanted free modes, and a sponge layer below the upper boundary to absorb the vertically propagating modes. As a test case, the linear version of the model is applied to the semi-diurnal and diurnal thermal tides in the lower and middle atmospheres ($\leq$100 km). The numerical results are compared with the analytical results obtained by Lindzen (1971).

Since we are dealing with a small number of planetary waves, a semi-spectral model with Fourier expansions in the E-W direction is more efficient than a 3-D grid point model because only a limited number of modes are needed to describe these waves. In general, at least 9-10 mesh points per wave length are needed to describe a

sinusoidal wave accurately, so for phenomena containing a narrow spectral band the saving in computer storage can be very large. However, spectral models are difficult to use in a system with height as the vertical coordinate, since the corresponding pressure tendency equation contains dependent variables in the denomenator. Therefore, in the present model, a quantity $\pi = -H_o \ln P/P_o$ is used as the vertical coordinate instead of height. The spectral equations in the π-coordinate system are less complicated than those in the z-coordinate system.

The physical model (described in Section 4.1) used for the test case is the same as the one described by Lindzen (1971), except for π being the vertical coordinate instead of height. The numerical techniques are described in Section 4.2. The model results are compared with Lindzen's (1971) results in Section 4.3.

4.1 The Physical Model

Following previous modelers, we shall make the following assumptions:

a. The atmosphere is a perfect gas in local thermodynamic equilibrium, with the gas constant uniform in height,

b. The earth is a perfect sphere with no topography,

c. The atmosphere is thin compared to the earth's radius,

d. Gravitational potential due to moon can be neglected,

e. The basic (or background) atmosphere is in hydrostatic balance with no motion,

f. Tidal oscillations are in quasi-hydrostatic balance, and

g. Equations of motion for the tidal oscillations can be linearized.

Lindzen (1971) gave some justification of making these assumptions in a study on atmospheric thermal tides; for more details, the reader is referred to this monograph.

With these assumptions, the relevant equations (see Appendix A for list of symbols) governing the tidal oscillations, in a system with $\pi = -H_o \ln P/P_o$ as

$$\frac{\partial u}{\partial t} - fv = -\frac{1}{a\cos\theta}\frac{\partial\Phi}{\partial\phi} + F_u \tag{4.1}$$

$$\frac{\partial v}{\partial t} + fu = -\frac{\partial\Phi}{a\partial\theta} + F_v \tag{4.2}$$

$$\frac{\partial\Phi}{\partial\pi} = \frac{R\, e^{-k\pi/H}\,\theta}{H} \tag{4.3}$$

$$\frac{\partial u}{a\cos\theta\partial\phi} + \frac{\partial v\cos}{\cos\theta\, a\,\partial\theta} + e^{\pi/H}\frac{\partial}{\partial\pi}\left(e^{-\pi/H}w\right) = 0 \tag{4.4}$$

$$\frac{\partial\theta}{\partial t} + w\frac{\partial\theta_M}{\partial\pi} = \frac{e^{k\pi/H}\,Q}{c_p} \tag{4.5}$$

and

$$\frac{\partial\Phi_B}{\partial t} = -\frac{R}{H}\,\theta_{MB}\, e^{-k\pi_B/H}\, w_1\,. \tag{4.6}$$

Equations (4.1) and (4.2) represent momentum conservation in the E-W and N-S directions respectively. The terms F_u and F_v are frictional terms and are intended mainly to: (a) get rid of the unwanted free inertia-gravity modes generated by the imperfect initial conditions; and (b) avoid reflections of the vertically propagating waves from the top boundary. Equations (4.3) and (4.4) represent the hydrostatic balance and mass continuity, respectively, and (4.5) is the thermodynamic equation. The term Q on the right side of (4.5) represents diabatic heating and contains, in this model, absorption of radiation by water vapor and ozone. The values of Q are computed by Leovy (1964) for various seasons

of the year, and their diurnal and semi-diurnal components in terms of Hough modes are given by Lindzen (1971). The latter values of Q are used in this model. Equation (4.6) is the tendency equation for the geopotential of the lower boundary.

4.2 The Numerical Model

Unlike in the usual spherical harmonic (spectral) models, in the semi-spectral model the variables are expanded in Fourier series in the E-W direction only, and are specified at discrete grid points in the N-S and vertical directions. The equations governing the coefficients of the Fourier modes are obtained by substituting the Fourier expansions of all the dependent variables in Equations (4.1) through (4.6). The resultant partial differential equations in latitude, height, and time are solved by finite difference methods.

The distance between the two poles is divided into equally spaced mesh intervals with a grid spacing of 2.5° latitude. The thermodynamic variables and vertical velocity are specified at one set of grid points (Figure 4.1) and the horizontal components of the velocity are specified at another set located half-way between them. The vertical direction is divided into a number of layers (Figure 4.2). All the variables except the vertical velocity are specified at the middle of each layer, and the vertical velocity is specified at the boundaries separating the layers. Below 100 km a layer thickness of 1 km is used for the diurnal and 2 km for semi=diurnal tide, since the former exhibits a more rapid vertical variation. Above 100 km the respective thicknesses are 2 and 4 km, since the Rayleigh friction damping increases rapidly with height.

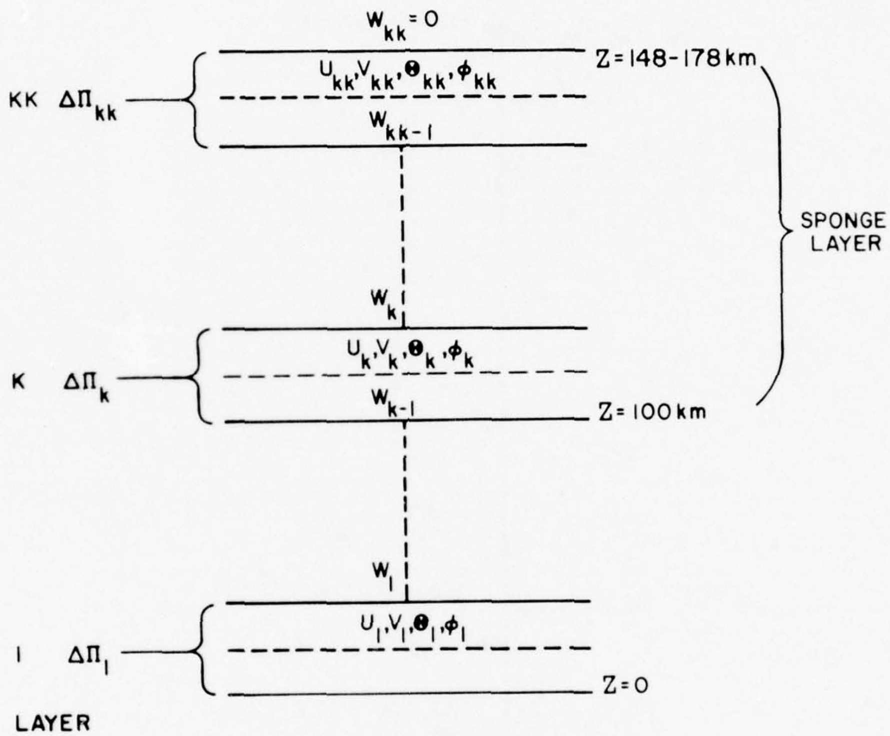

Fig. 4.1 — Vertical layering of the numerical model

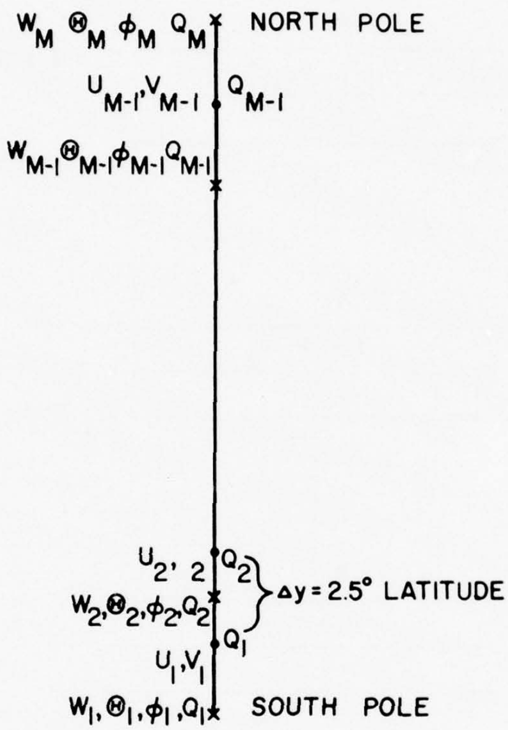

Fig. 4.2 — Grid system in the N-S direction

Time Integration Scheme

The model is integrated by using a two step predictor-corrector (leapfrog-trapezoidal) scheme. When applied to a wave equation, this scheme has a neutral amplitude growth with a very small phase error (Kurihara, 1965). The two steps of integration for the equation $\frac{du}{dt} = F(H)$ are:

$$H^{*} = H^{t-Dt} + 2Dt\, F(H^{t}) \qquad \text{Leapfrog Predictor} \qquad (4.7)$$

$$H^{t+Dt} = H^{t} + \frac{Dt}{2} \left| F(H\ ) + F(H^{t}) \right| \qquad \text{Trapazoidal Corrector} \qquad (4.8)$$

where the superscript represents the time level and H is the value of H predicted by leapfrog scheme. Even though the scheme generates a computational mode, the latter never grows big enough to cause appreciable time splitting.

The Sponge Layer and Rayleigh Friction

One of the main disadvantages of using the initial-value problem approach for the tidal problem is that many, if not all, of the free modes of atmospheric oscillations will be excited due to imperfectly posed initial conditions. These are eliminated in this model by introducing a transient Rayleigh friction of about 1.5×10^{-6} sec^{-1} (which corresponds to an e-folding time of about six days for atmospheric oscillations) throughout the lower 100 km of the atmosphere. It is gradually reduced over a period of 25 days to a value of about 10^{-7}sec^{-1} (yielding an atmospheric e-folding time of 108 days). Since the final value of the Rayleigh friction is neglegibly small, the results obtained from the model will approximately correspond to those of a non-viscous atmosphere.

For an atmosphere with little or no friction, the initial value approach suffers from another disadvantage, namely, that the vertically propagating waves are reflected back from the top boundary and contaminate the solution. These reflections are eliminated in the model by introducing a sponge layer with a thickness between 50 km to 80 km above the region of interest. In this layer, the Rayleigh friction is increasing with height, thereby absorbing the vertically propagating oscillations as they move up (and down) through the region. This upper layer friction remains constant in time; in order to maintain continuity with the diminishing lower layer friction, we must lower the boundary of the lower and upper regions appropriately with time, approaching 80 km near the end. The terms F_u and F_v in Equations (4.1) and (4.2) take the following form:

$$F_u = - K_z(\pi)\, u \qquad (4.9)$$

and

$$F_v = - K_z(\pi)\, v \qquad (4.10)$$

where $K_z(\pi) = 0.25 \times 10^{-6} \exp (\pi + \pi_B - 95)/7 \qquad \pi_1 \leq \pi \leq \pi_T$

$$= K_z(\pi_1) \qquad \pi_B \leq \pi \leq \pi_1$$

Figure 4.4 illustrates the behavior of $K_z(\pi, \pi_1(t))$.

Boundary and Initial Conditions

In order to solve Equations (4.1) through (4.6) numerically, it is sufficient to specify the values of the geopotential and the vertical velocity at the two poles, and vertical velocity at top of the model. All of these are assumed to be zero. The absence of real friction

and advection makes these simple conditions possible.

Initially, all the tidal perturbations are assumed to be of zero amplitude. The basic atmosphere is in hydrostatic balance with no motion. The basic atmosphere for the diurnal tide is assumed to be isothermal with a temperature of 260°K. The temperature distribution for the basic atmosphere in semi-diurnal case is given in Figure 4.3. In the lowest 100 km, this is the same as the equatorial temperature profile given by Lindzen (1971).

The diabatic heating is that of Lindzen (1971) and consists of linear combination of the (2,2), (2,4), and (2,6) Hough modes for the semi-diurnal tide, and the (1,-4), (1.-2), (1,1), (1,3), and (1,5) Hough modes for the diurnal tide. For the semi-diurnal tide, all the three Hough modes propagate vertically for the temperature distribution used in the calculations (Fig. 4.3) except the (2,2) mode between 50 km and 80 km altitude. For an isothermal basic temperature, the modes (1,-4) and (1,-2) are trapped completely, while the other three modes propagate vertically everywhere. The trapped modes dominate at higher latitudes while the propagating modes dominate at latitudes between the equator and 30°. The modes (2,6) and (1,5) have the shortest vertical wave lengths for semi-diurnal and diurnal tides, respectively, with wave lengths of about 33 km and 7 km. The reader is referred to Lindzen (1971) for more details about the structure and behavior of these modes.

The Diurnal Tide

In order to see how well the model reproduced both the trapped and propagating modes, a comparison is made with Lindzen's (1971) results

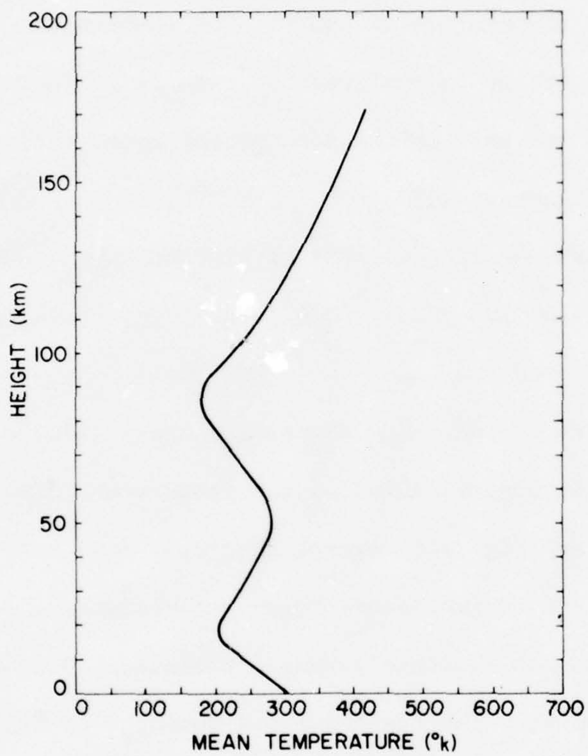

Fig. 4.3 — Mean atmospheric temperature (°K) for the semi-diurnal tide

at 75°, 45° and 15° latitudes. Amplitudes and phases of the three components of the tidal velocity are given in Figures 4.5 through 4.10 at 75° latitude, in Figures 4.11 through 4.16 at 45° latitude, and in Figures 4.17 through 4.22 at 15° latitude. It can be seen from these figures that the model reproduced the analytical results at 75° and 45° latitudes very well. However, the numerical results deviated slightly from the analytical results at 15° latitude. This can be attributed to poor vertical resolution, insufficient to resolve the (1,5) Hough mode. According to Grammeltvedt (1969), in general one needs more than 15 grid points per wave length to reproduce the amplitude and phase of a propagating wave. With 1 km grid length, we have only about 7 grid points to resolve the (1,5) Hough mode, therefore, one can attribute the observed deviations to truncation errors. It is important to note that the vertical velocities presented in Figures 4.9, 4.15 and 4.21 represent $\frac{d\pi}{dt}$, rather than $\frac{dz}{dt}$. In order to achieve a comparison, the $\frac{d\pi}{dt}$ values corresponding to Lindzen's z calculations have been computed.

Semi-Diurnal Tide

It is easier to simulate the semi-diurnal tide numerically than the diurnal tide, since the former has a less complicated vertical structure than the latter. To show the accuracy of the model in simulating the semi-diurnal tide, the amplitudes of u at 75° latitude, v at 45° latitude, and w at 15° latitude are plotted against the analytical results in Figures 4.23, 4.24, and 4.25 respectively. It can be clearly seen from the figures that the model reproduces the analytical semi-diurnal tide almost exactly.

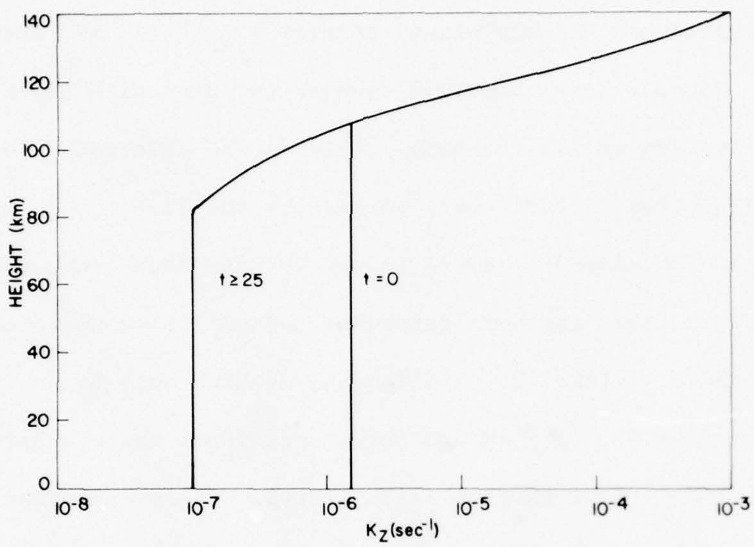

Fig. 4.4 — k_z as a function of height and time

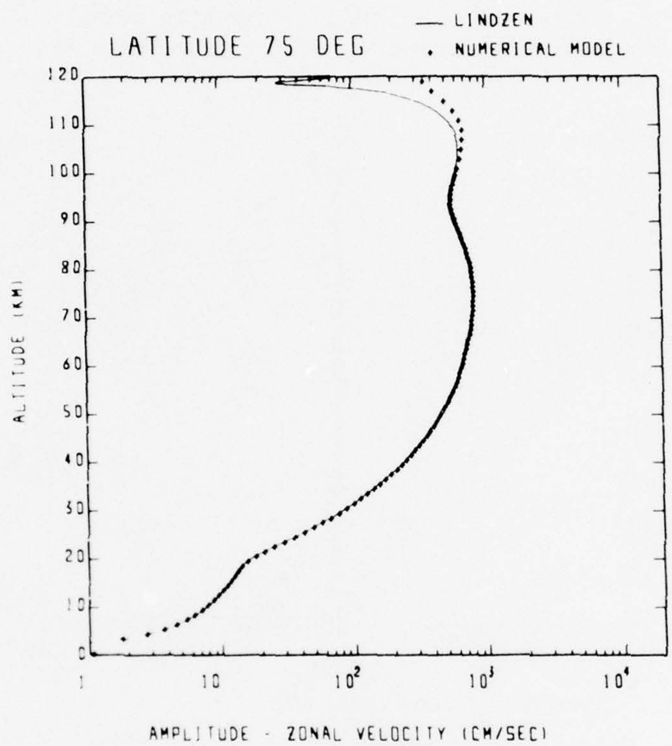

Fig. 4.5 — Amplitude of the westerly velocity (cm sec^{-1}) of the diurnal tide at 75° latitude

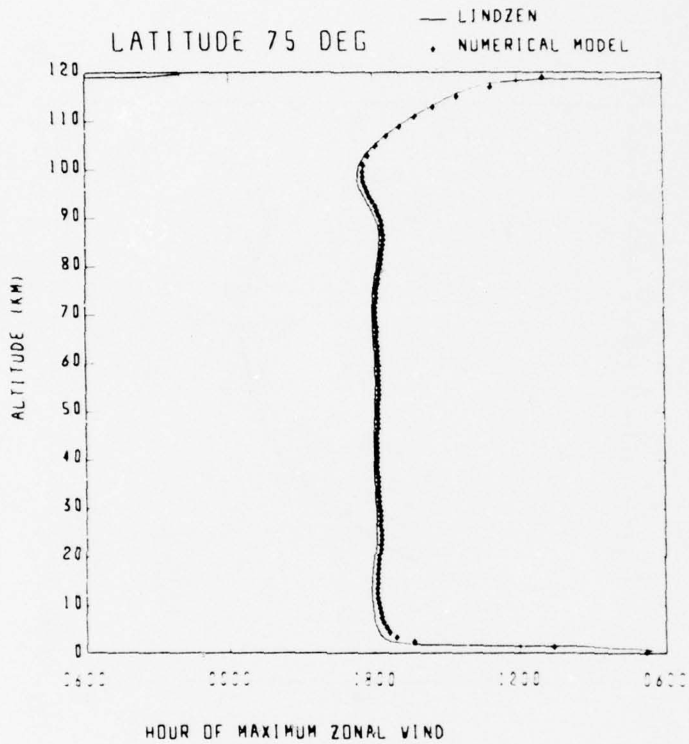

Fig. 4.6 — Phase of the westerly velocity of the diurnal tide at 75° latitude

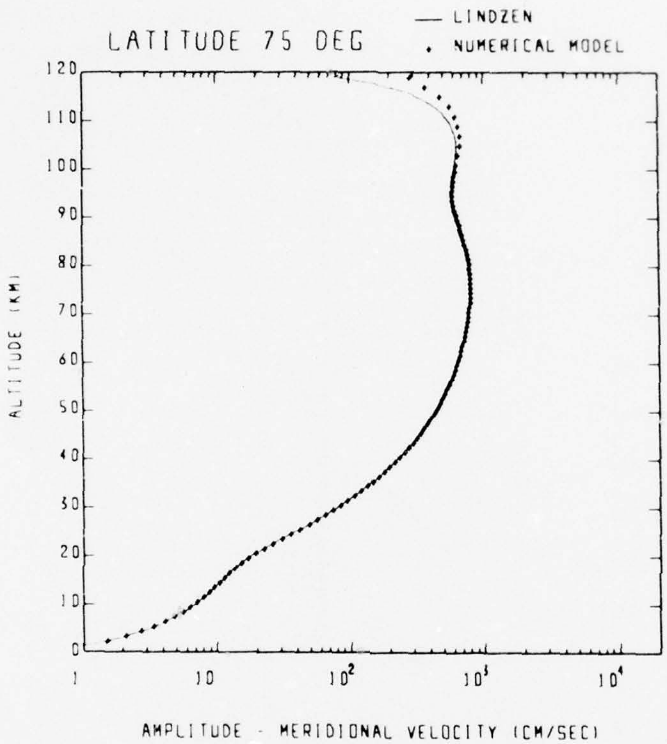

Fig. 4.7 — Amplitude of the northerly velocity (cm sec^{-1}) of the diurnal tide at 75° latitude

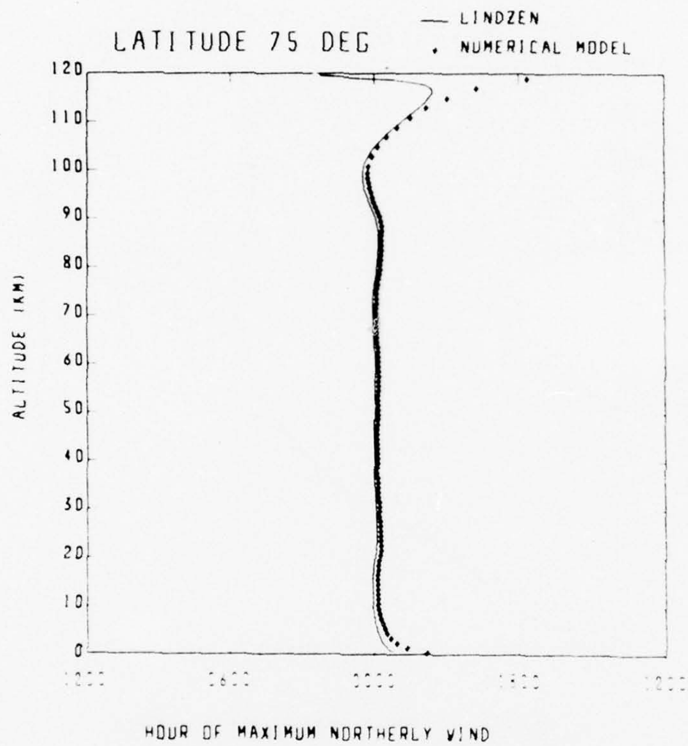

Fig. 4.8 — Phase of the northerly velocity of the diurnal tide at 75° latitude

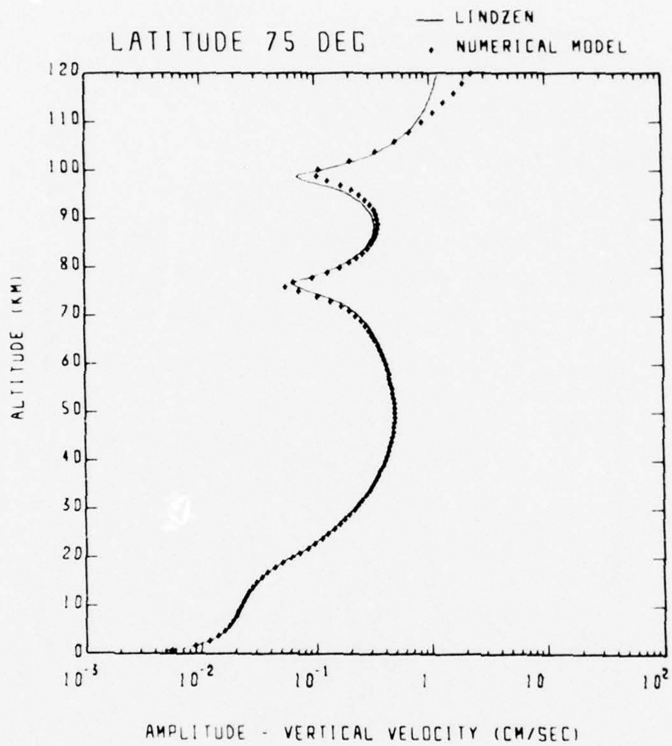

Fig. 4.9 — Amplitude of the vertical velocity, $d\pi/dt$, of the diurnal tide at 75° latitude (units: cm sec^{-1})

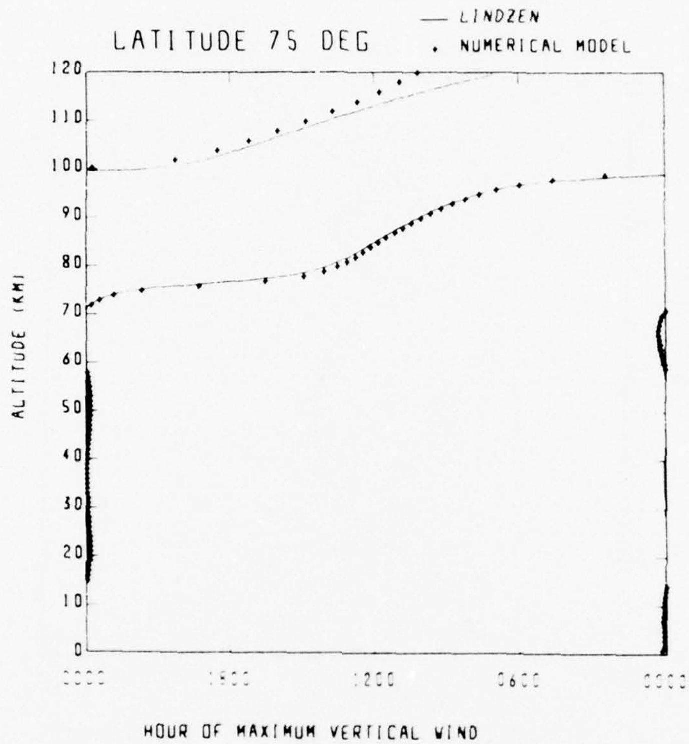

Fig. 4.10 — Phase of the vertical velocity of the diurnal tide at 75° latitude

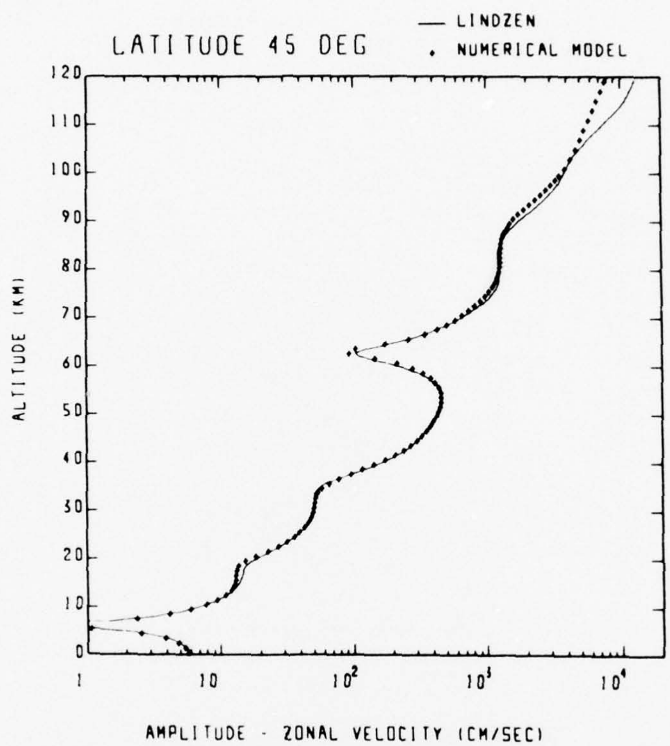

Fig. 4.11 — Amplitude of the westerly velocity (cm sec^{-1}) of the diurnal tide at 45° latitude

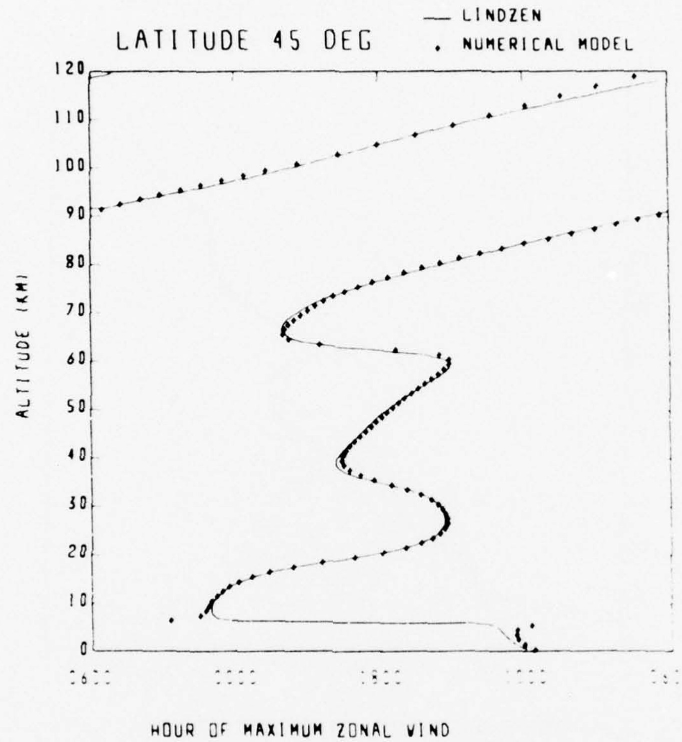

Fig. 4.12 — Phase of the westerly velocity of the diurnal tide at 45° latitude

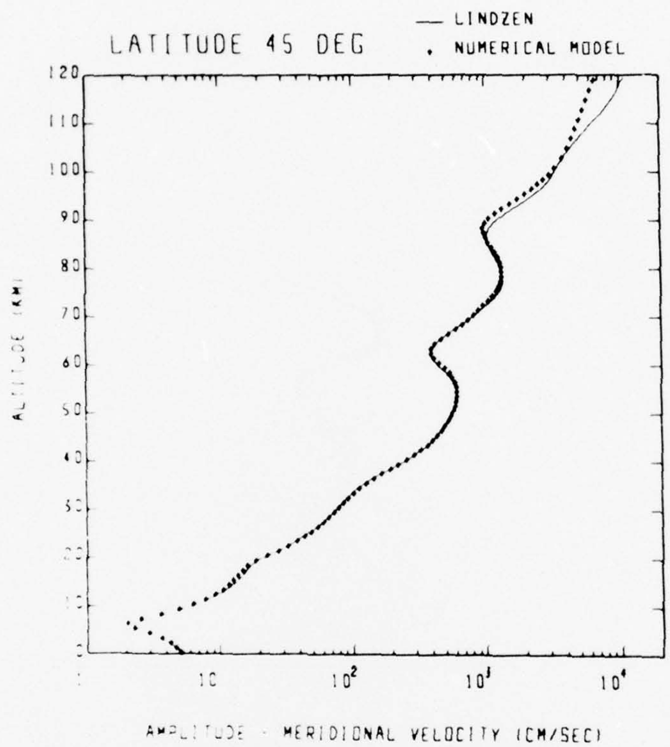

Fig. 4.13 — Amplitude of the northerly velocity (cm sec^{-1}) of the diurnal tide at 45° latitude

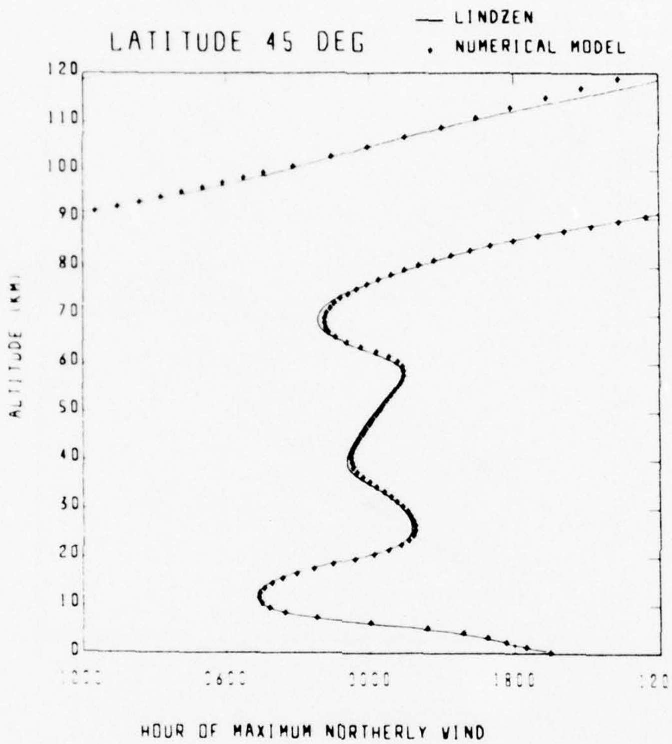

Fig. 4.14 — Phase of the northerly velocity of the diurnal tide at 45° latitude

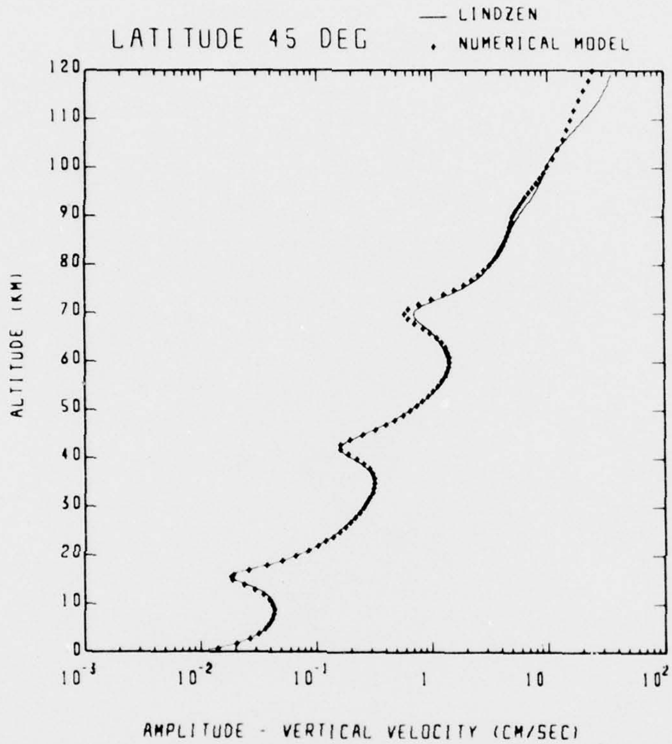

Fig. 4.15 — Amplitude of the vertical velocity, $d\pi/dt$, of the diurnal tide at 45° latitude (units: cm sec^{-1})

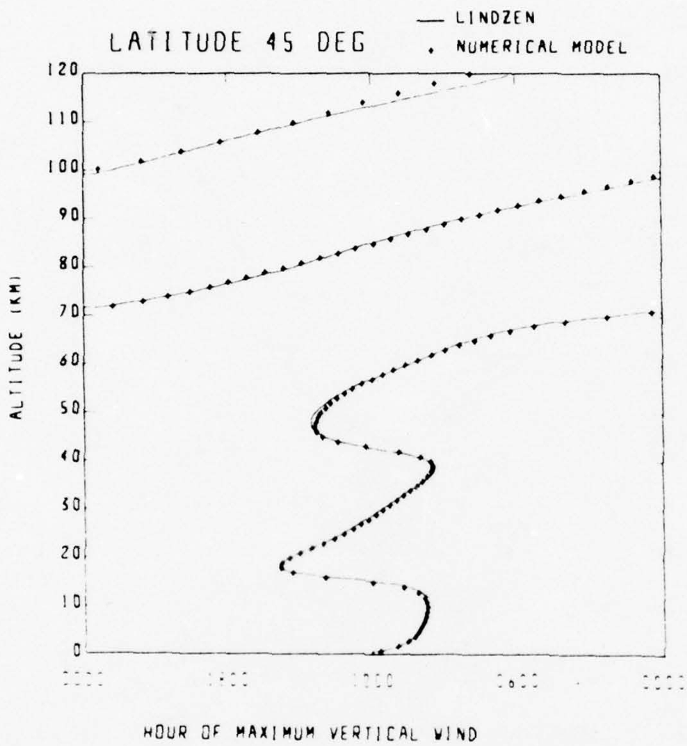

Fig. 4.16 — Phase of the vertical velocity of the diurnal tide at 45° latitude

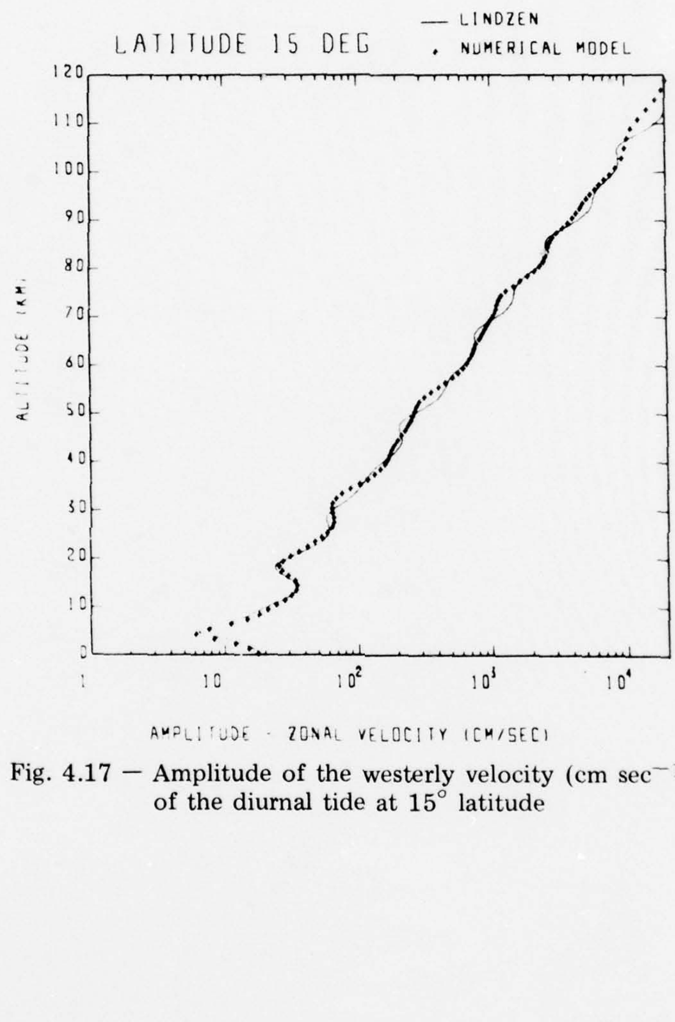

Fig. 4.17 — Amplitude of the westerly velocity (cm sec^{-1}) of the diurnal tide at 15° latitude

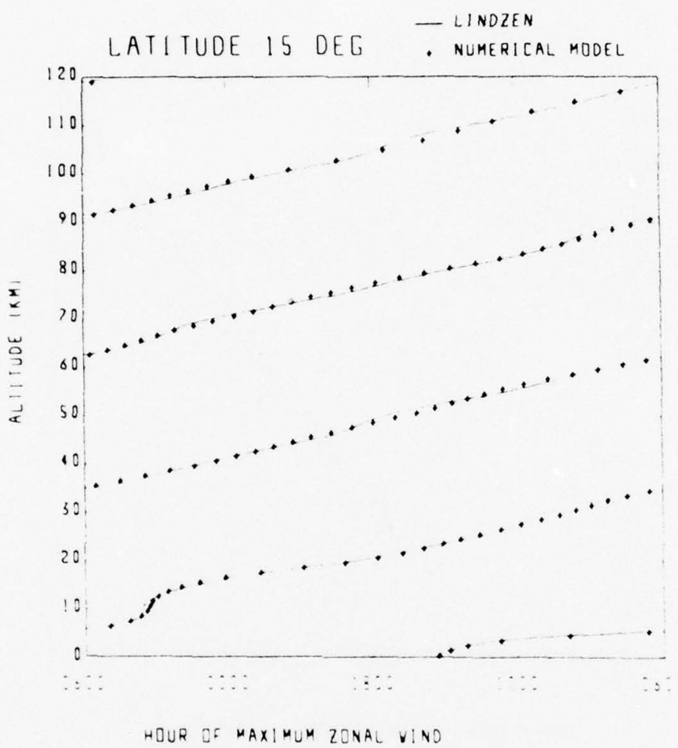

Fig. 4.18 — Amplitude of the northerly velocity (cm sec^{-1}) of the diurnal tide at 15° latitude

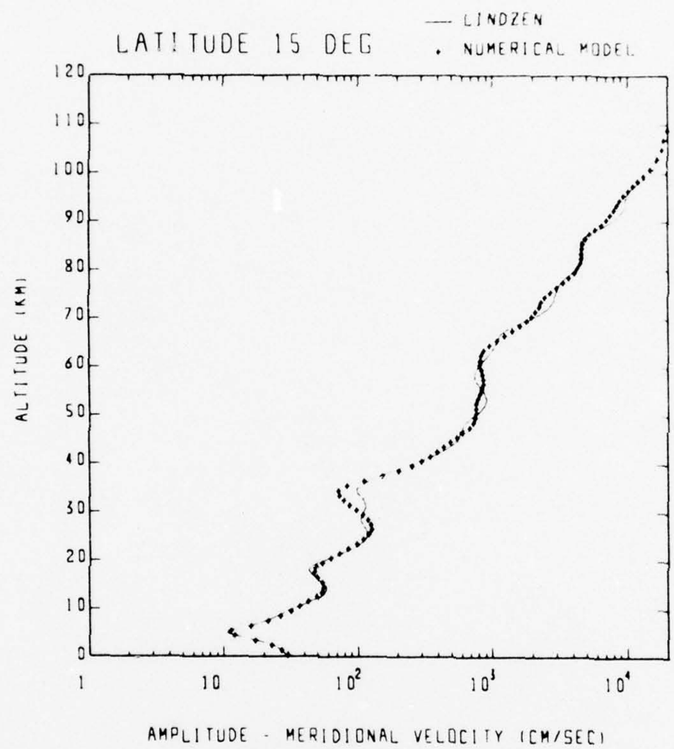

Fig. 4.19 — Amplitude of the northerly velocity (cm sec^{-1}) of the diurnal tide at 15° latitude

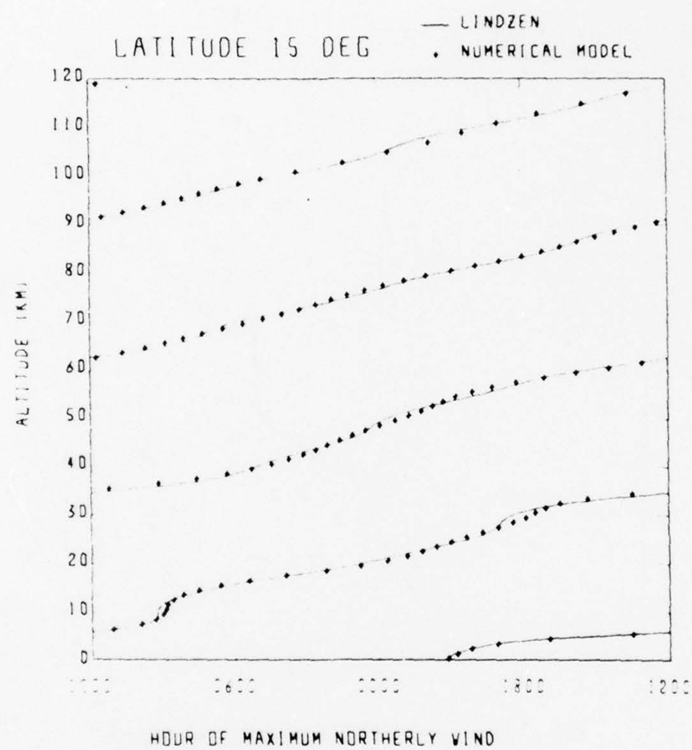

Fig. 4.20 — Phase of the northerly velocity of the diurnal tide at 15° latitude

AD-A043 178 NAVAL RESEARCH LAB WASHINGTON D C F/G 4/1
POST STABILIZATION IONIZATION LEVEL PREDICTIONS. VOLUME III OF --ETC(U)
APR 77
UNCLASSIFIED NRL-MR-3488 NL

2 OF 2
ADA043178

END
DATE
FILMED
9-77
DDC

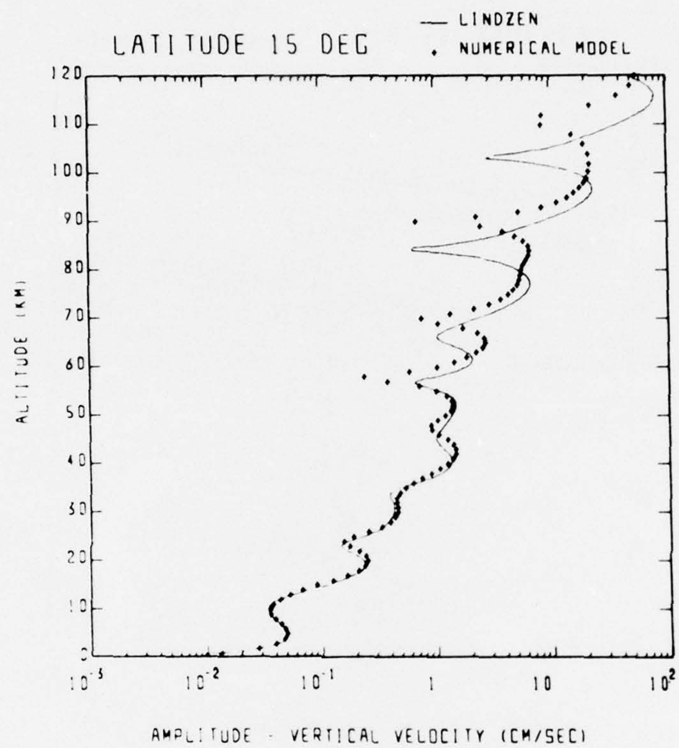

Fig. 4.21 — Amplitude of the vertical velocity, $d\pi/dt$, of the diurnal tide at 15° latitude (units: cm sec^{-1})

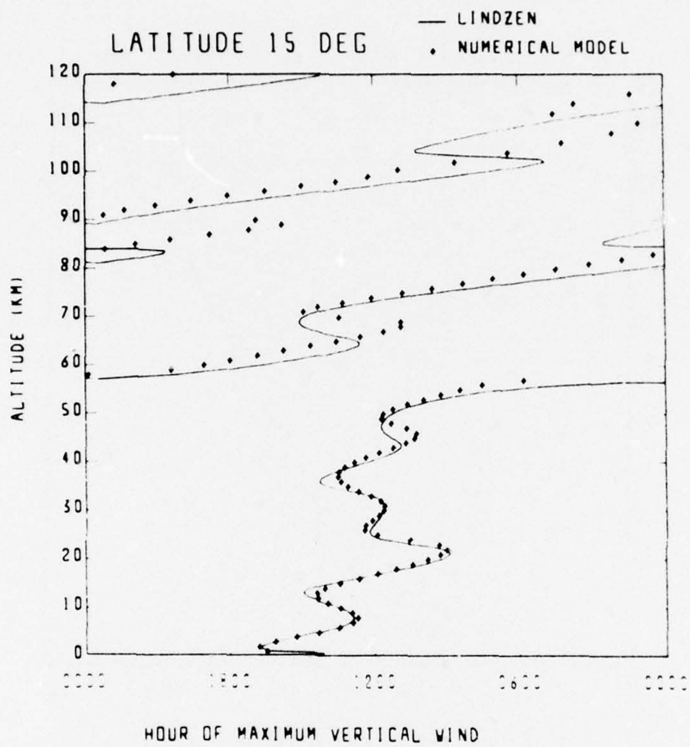

Fig. 4.22 — Phase of the vertical velocity of the diurnal tide at 15° latitude

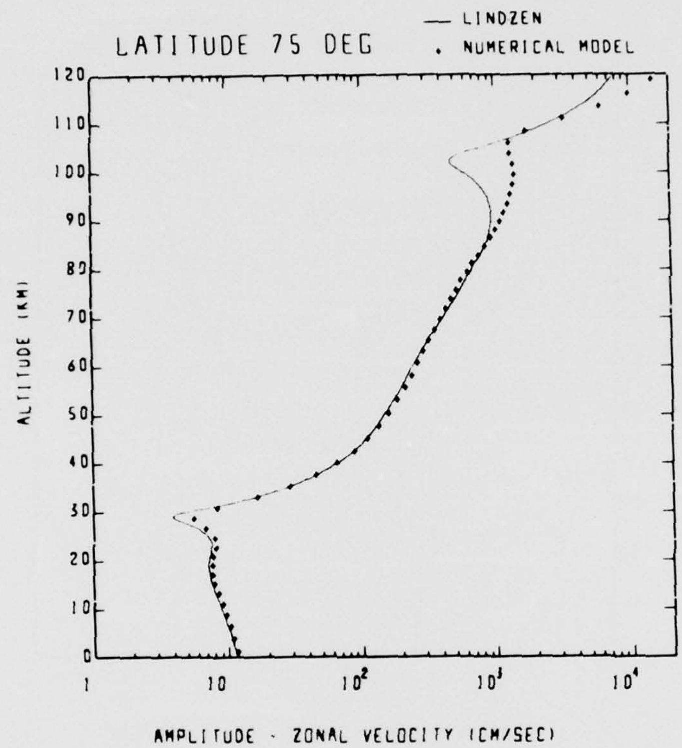

Fig. 4.23 — Amplitude of the westerly velocity (cm sec^{-1}) of the semi-diurnal tide at 75° latitude

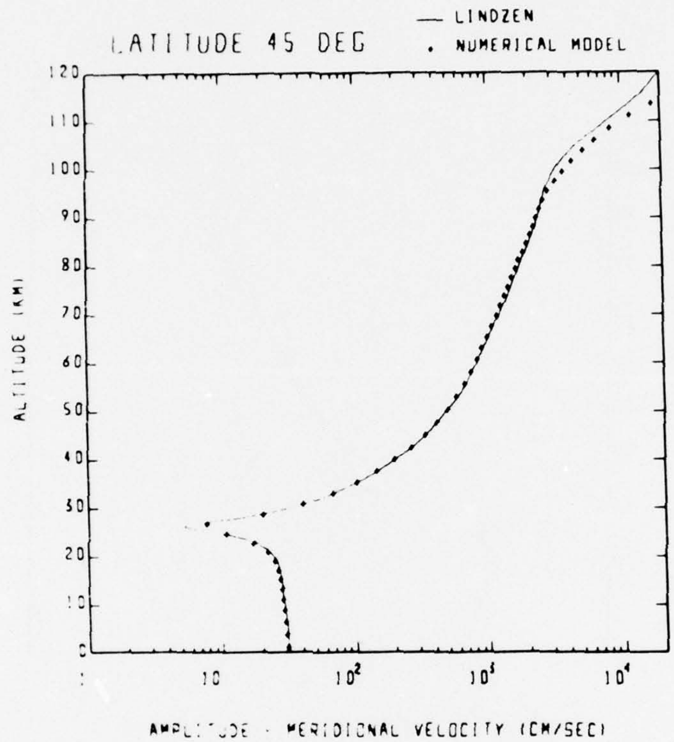

Fig. 4.24 — Amplitude of the northerly velocity (cm sec^{-1}) of the semi-diurnal tide at 45° latitude

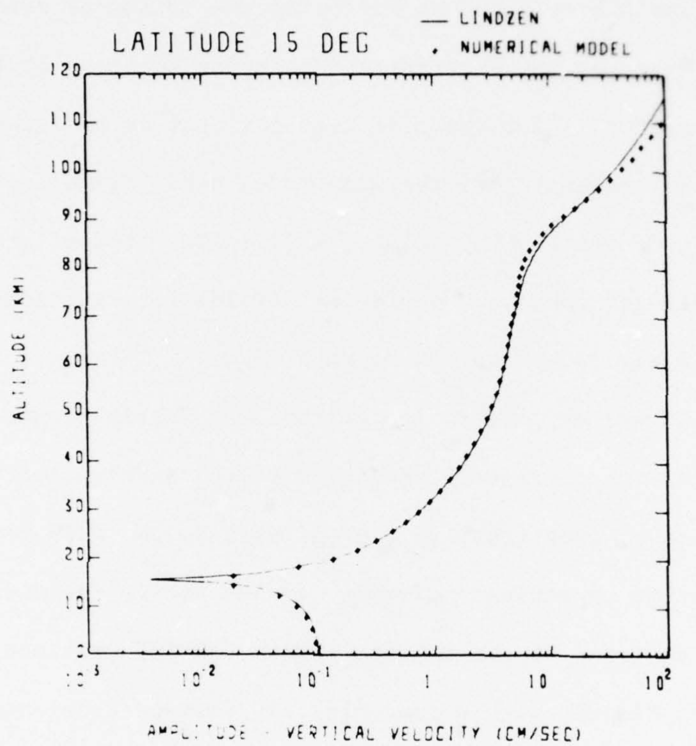

Fig. 4.25 — Amplitude of the vertical velocity, $d\pi/dt$, of the semi-diurnal tide at 15° latitude (units: cm sec^{-1})

Section 5

BETA PATCH DEVELOPMENT

S.Zalesak, J. Block, D. Strickland

ADVECT is a Lagrangian computer program which tracks the advection of a passive nuclear debris cloud by following the motion of nets of tracer particles defining the exterior and interior surfaces of the cloud. The wind field responsible for the advection is input as an external parameter. For the present study the wind model used is the empirically based one given by Groves (1969). CIRA (1972) in the form of mean seasonal longitudinally averaged zonal and meridional fields for latitudes from 80° S to 80° N and altitudes from 25 km to 130 km.

When ADVECT was applied to typical nuclear debris clouds for times up to 48 hours after release, results differed significantly from those of other models, specifically, the one used by the WEPH code. WEPH produces a cloud expanding uniformly in the horizontal direction and at all times centered at the release point: ADVECT predicts elongated, almost thread like clouds, with a predominately east-west orientation with generally significant displacements of the center of mass from the release point. Since beta patch patterns are similar in shape to the debris clouds, it is likely that the differences in cloud advection between the two models would also be reflected in the predictions of communications interference.

The communications environment at any given time after a nuclear event is characterized, as far as beta effects are involved, by the distribution of free electrons in the atmosphere. To arrive at this distribution it was necessary to add to ADVECT subroutines which would

generate a properly distributed beta flux, calculate the resulting ionization rates for regions conjugate to the cloud, and finally produce a quasi-equilibrium density distribution for free electrons. The analytic model of Knapp and Fischer (1970) for beta transport was used along with the ionization and recombination rates prescribed by them.

A brief review of ADVECT and the beta deposition routines appended to it is given in this report along with some typical results provided by the code. This section concludes with a review of the beta transport treatment (Knapp and Fischer, 1970) and the results of a study of its relative accuracy.

5.1 ADVECT-Review

A detailed description of the basic ADVECT computer code is found in Zalesak and Coffey (1975). Briefly, the interior and exterior surfaces of a nuclear debris cloud after stabilization are defined as nets of tracer particles which move passively in a predetermined velocity field. At each time step, each tracer particle is moved using a second order scheme with the local fluid velocity multiplied by the time step increment. Thus from the simplest of calculations, the motion of the entire cloud is determined.

Calculations of typical stabilized debris clouds using ADVECT quickly revealed the overwhelming importance of vertical wind shear, as well as of net translation of the cloud by the winds. While the models used in codes like WEPH predicted a constant horizontal radial expansion of the cloud in time, with the center of mass remaining at the release point, ADVECT revealed a rapid vertical shearing of the cloud,

predominantly in the east-west direction. At times later than a few hours, the cloud gives the appearance of a long worm-like structure. In addition, large excursions of the center of mass of this structure from the initial release point were not uncommon.

As an example, Fig. 5.1 shows the computed position and configuration of clouds 24 hours after release over the central United States (40°N, 265°E) at 75 km altitude on 4 different days of the year (Jan. 1, Apr. 1, July 1, Oct. 1, respectively) at 12:00 noon. The clouds were originally centered ellipsoids 20 km thick vertically and 60 km in horizontal diameter. The box in the map of each plot shows the location of the longitude-latitude-altitude "box" enclosing the cloud given by ADVECT. By contrast, the circle shows the cloud location given by the model in WEPH. The plots below the map in each figure display views of the aforementioned longitude-latitude-altitude box enclosing the ADVECT cloud from above and from the south. Note that the abscissa and ordinate are not to scale, as can be seen from the cloud-box dimensions given below the two plots.

5.2 <u>Addition of Beta Deposition Routines to ADVECT</u>

From the results of the previous section, it is obvious that one would expect differences in communication path conditions between ADVECT and the models used in WEPH. In order to quantify these differences, it was necessary to add beta particle deposition and chemistry routines to ADVECT. We describe the physics briefly:

For several days after the release a nuclear debris cloud is an intense source of beta particles. These beta particles are constrained

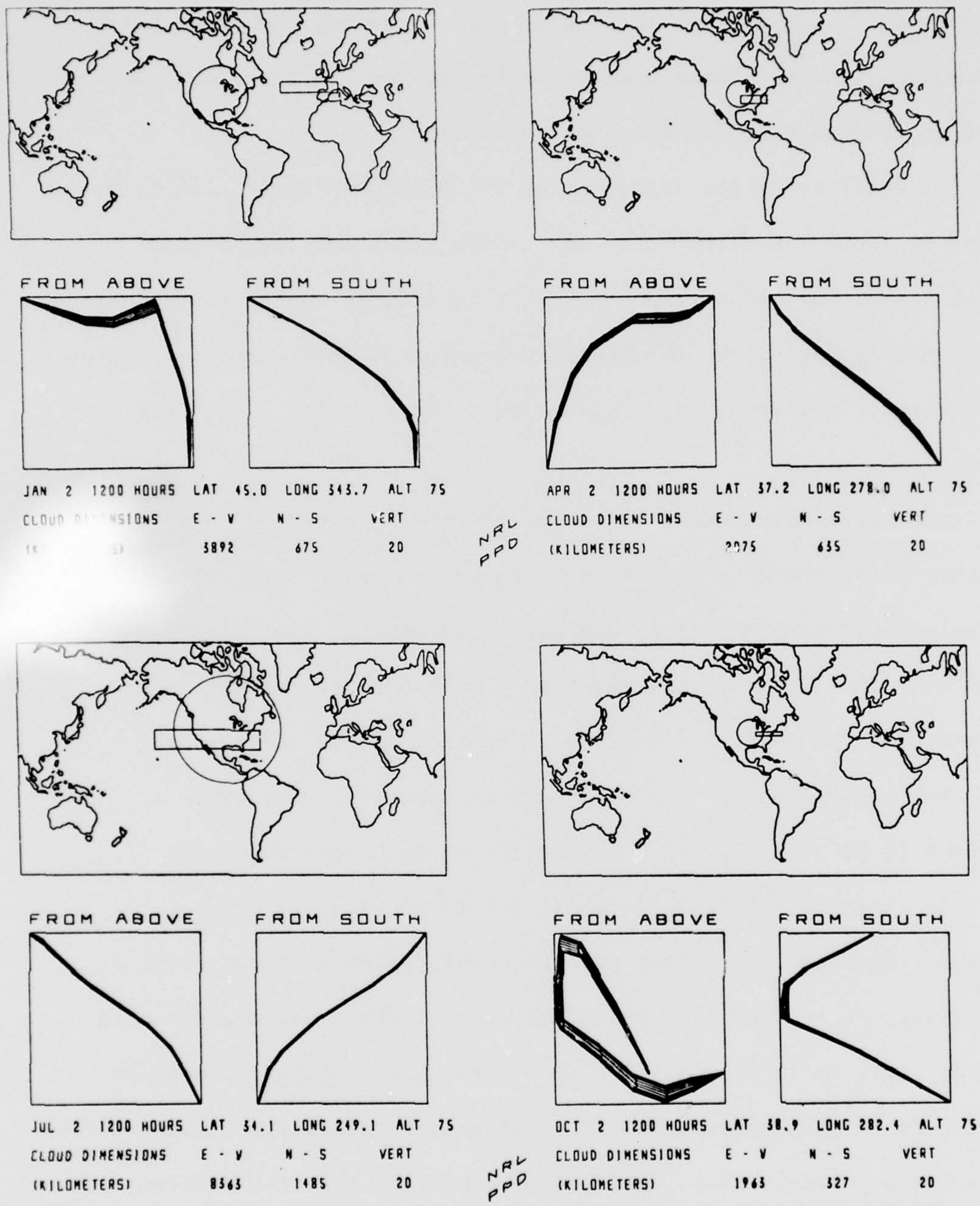

Fig. 5.1 — Cloud configurations and positions 24 hours after release for clouds released at 75 km altitude over central United States on dates Jan. 1, Apr. 1, July 1, and Oct. 1. The circles on the map represent the results of a horizontal radial expansion about the release point, while the rectangles represent the results of ADVECT.

to move along geomagnetic field lines. Half the beta particles produced along a given field line are assumed to escape upward; the other half move downward into the dense atmosphere below, and are absorbed. The absorption process produces enhanced ionization.

At equilibrium the intensity of the β induced ionization is determined by local ion-electron recombination rates and the external electron deposition rate. The net result is a quasi-equilibrium electron density enhancement below, the degree depending on beta particle flux, cloud altitude, effective dip angle, time of day, latitude, and the altitude in question.

The first step toward the computation of electron density enhancements was the development of a subroutine which integrated the local beta particle production rate along geomagnetic field lines through the cloud. To do this required a more precise definition of the surface of the cloud. A surface is defined in our model as the sum of the subsurfaces of an n x m "net" of tracer points. Thus a subsurface is the interior of a figure formed by connecting point (i,j) to $(i + 1, j)$ to $(i + 1, j + 1)$ to $(i, j + 1)$ to (i,j), $1 \leq 1 \leq n$, $1 \leq j \leq m$. However, these four points do not define a unique surface. The ambiguity is removed by subdividing each of these subsurfaces with a line from (i,j) to $(i + 1, j + 1)$, thus forming two <u>planar</u> triangular subdivisions in each subsurface. The integrated beta particle production rate, or beta particle flux, is found by computing the intersection, if any, of a geomagnetic field line with each subsurface, multiplying the production rate between intersections by the distance between intersections, and summing over all intersection pairs. The local production rate itself

depends on the fission yield of the nuclear device in question and on the time elapsed after the burst.

Once the beta particle flux along a field line is known, the electron density enhancement at any point along that field line can be computed using the prescriptions given in Knapp and Fischer (1972). Further prescriptions in Knapp and Fischer can be used to compute the non-deviative absorption of the enhanced region due to electron-neutral, ion-neutral, and ion-electron collisions for a given electromagnetic wave frequency.

Figures 5.2 - 5.4 show the results from ADVECT for a 1 megaton fission yield cloud released at 95 km altitude over Johnston Island (169.9° W, 16.5°N) on January 1, 6 hours after release. Displayed are 10 MHz wave absorption contours (db/km) as a function of longitude (abscissa) and latitude (ordinate) in degrees for altitudes, 65, 75, and 85 km respectively. Figures 5.5 - 5.7 display the same results for a WEPH-type code. In addition, Figures 5.8 and 5.9 plot the latitude and longitude integrated attenuations, respectively, for both the ADVECT and WEPH-type code calculations of the above problem. These plots give the total signal attenuation in db for 10 MHz signals along all east-west and north-south paths through the clouds at each of the three altitudes.

It can be seen that the vertical extent of the significant signal attenuation is considerable ($\sim$30 km) and that is fact the attenuation region presents itself as a rather thick "curtain" through which signals may or may not have to pass, depending on the exact geometry of the signal path. Note that quite significant attenuation can take

Fig. 5.2 — Results from ADVECT: 10 MH_z wave attenuation contours (db/km) at altitude 65 km, six hours after release of 50 kiloton cloud at 95 km over Johnston Island (169.9°W, 16.5°N). The abscissa is the longitude in degrees and the ordinate is the latitude in degrees.

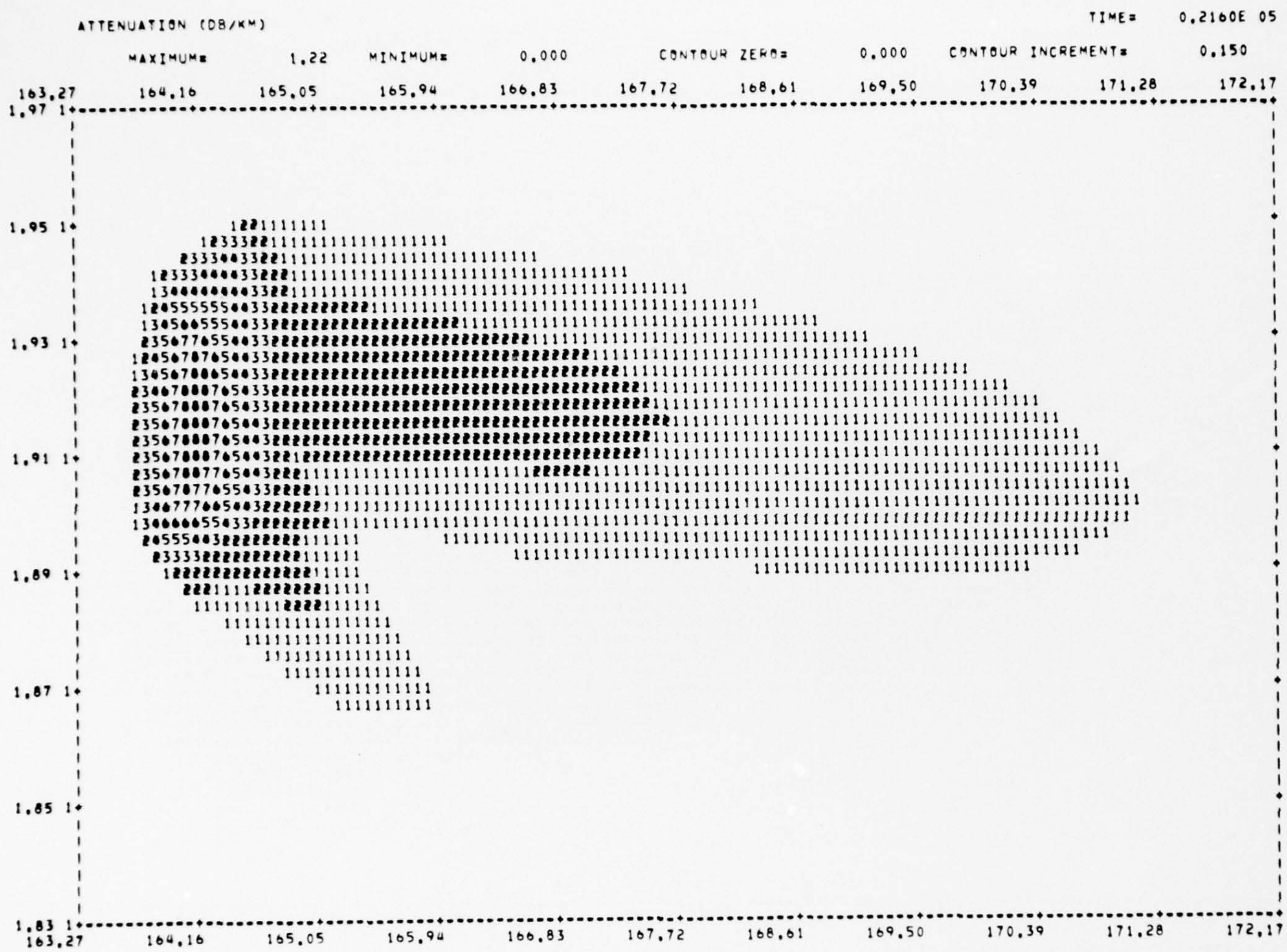

Fig. 5.3 — Same as Fig. 5.2 but at altitude 75 km

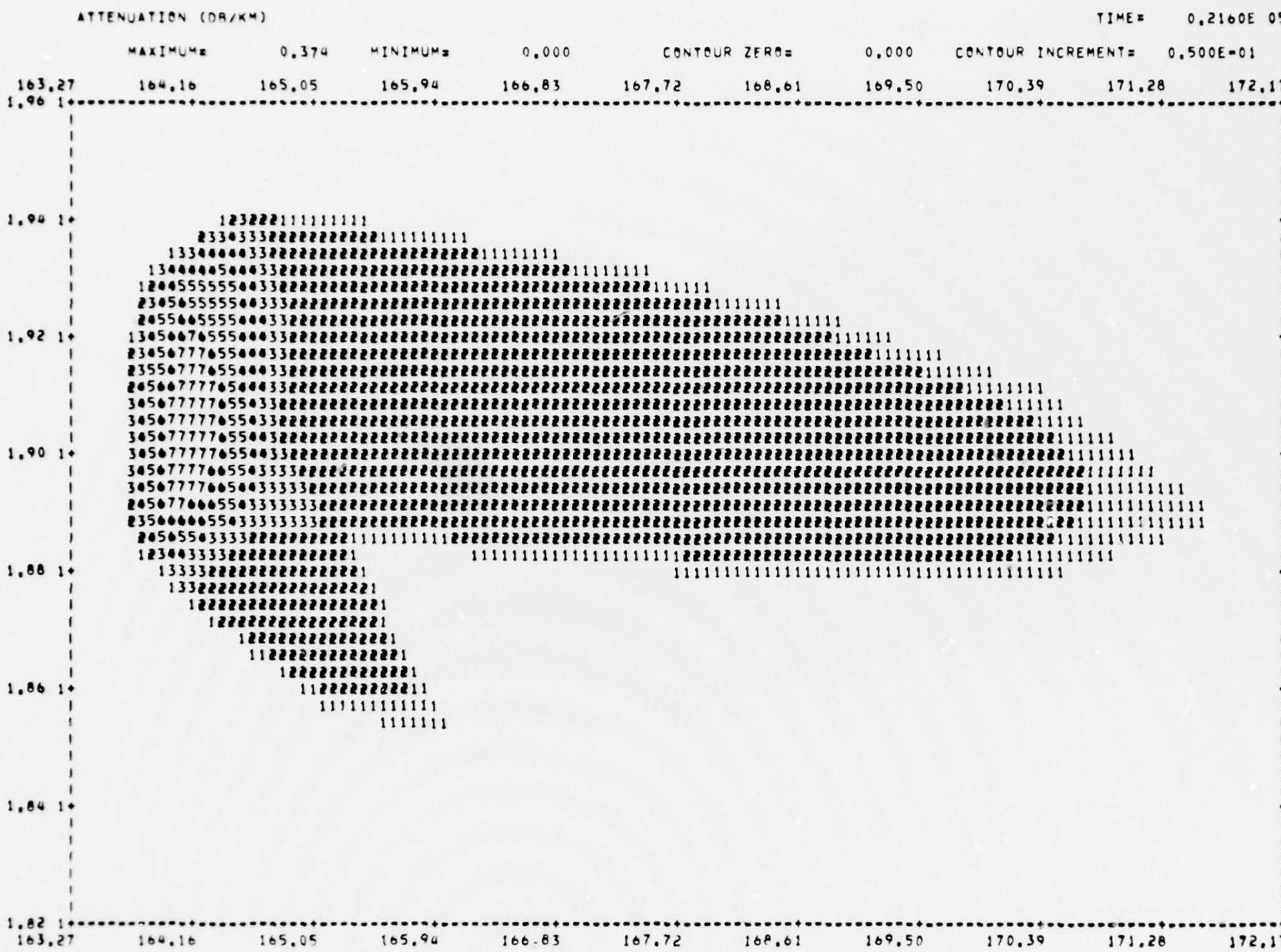

Fig. 5.4 — Same as Fig. 5.2 but at altitude 85 km

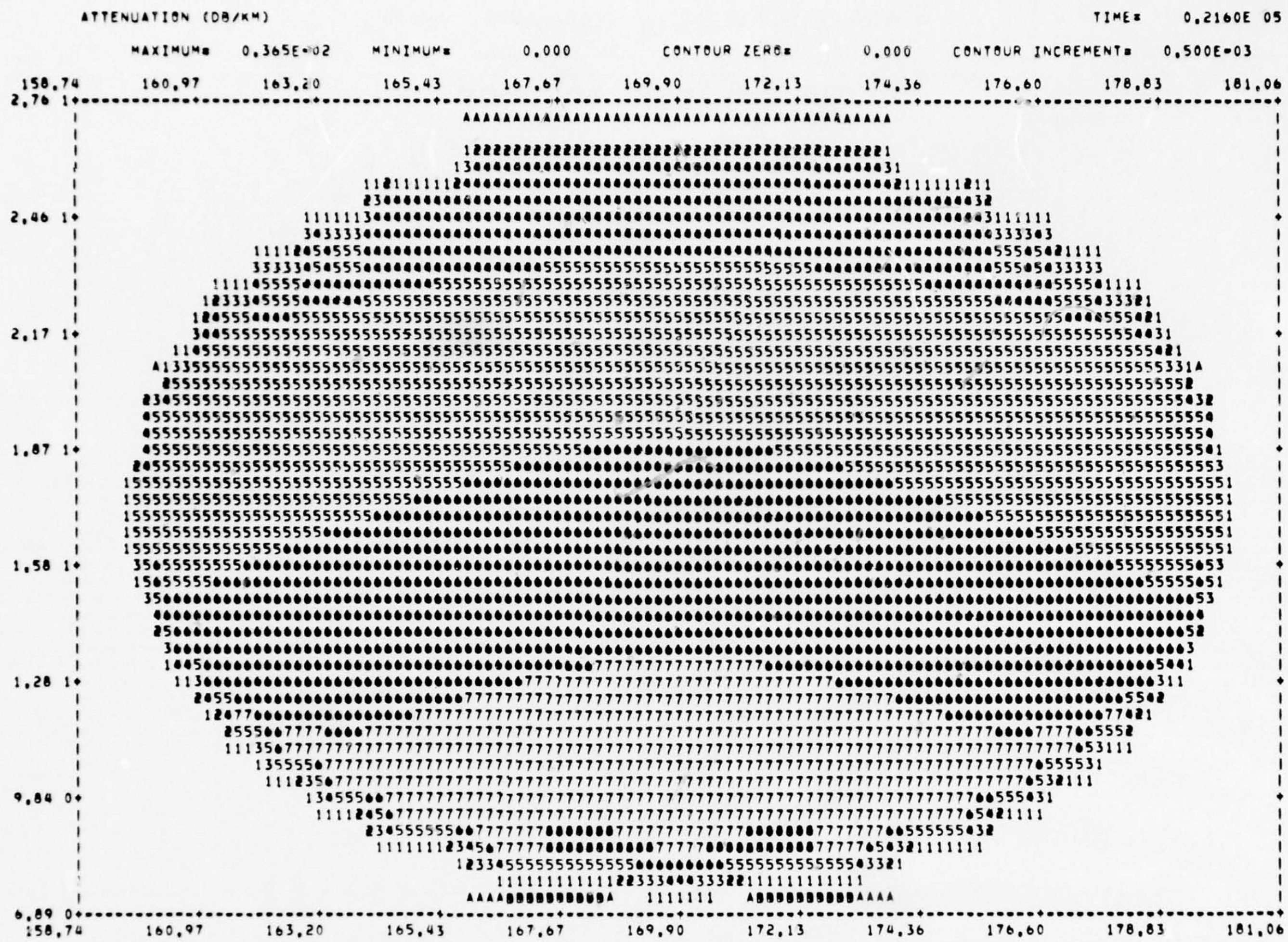

Fig. 5.5 — Same as Fig. 5.2 but for results of WEPH-type horizontal expansion about stabilization point. Contours evaluated at altitude 65 km.

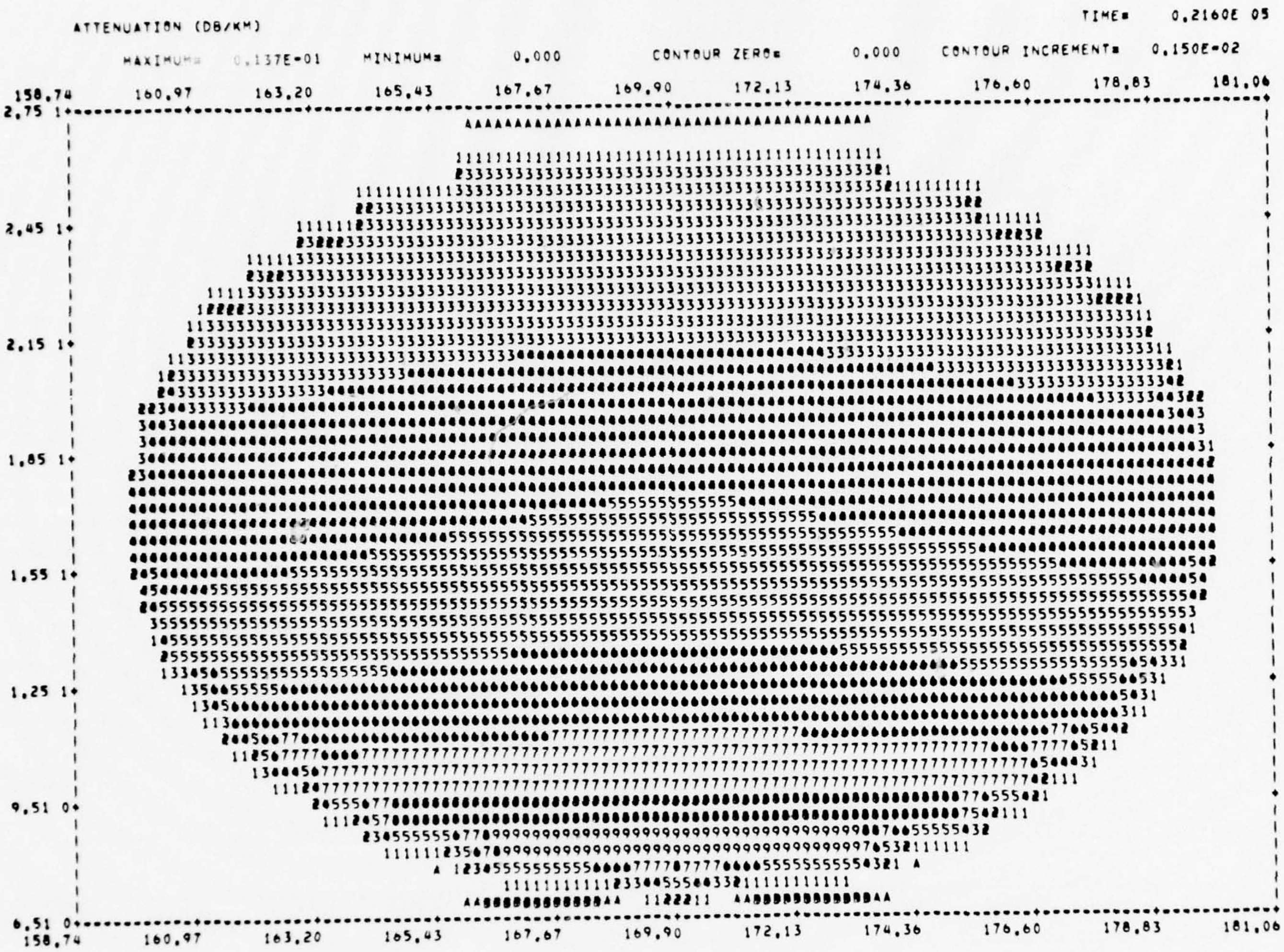

Fig. 5.6 — Same as Fig. 5.5 but at altitude 75 km

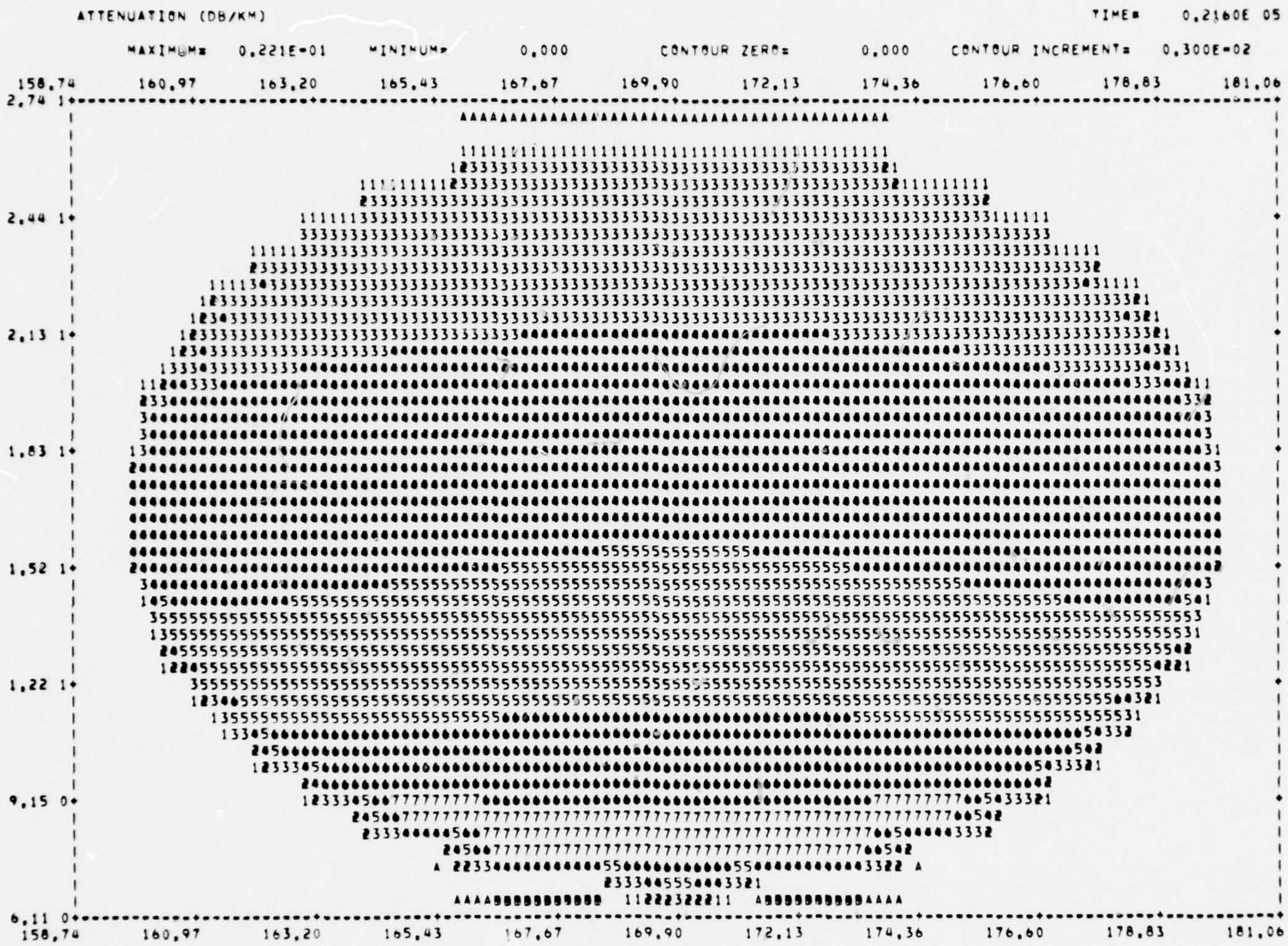

Fig. 5.7 — Same as Fig. 5.5 but at altitude 85 km

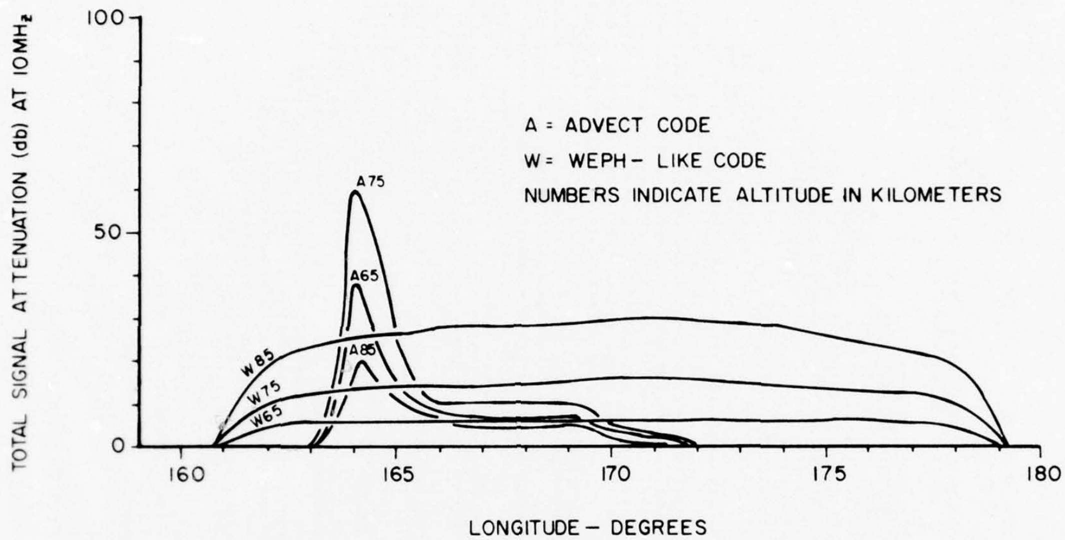

Fig. 5.8 — Total 10 MH_z wave attenuation (db) for north-south directed signal path vs longitude of signal path in degrees. Shown are plots for both the ADVECT and WEPH-like calculations at 65, 75 and 85 km signal path altitude.

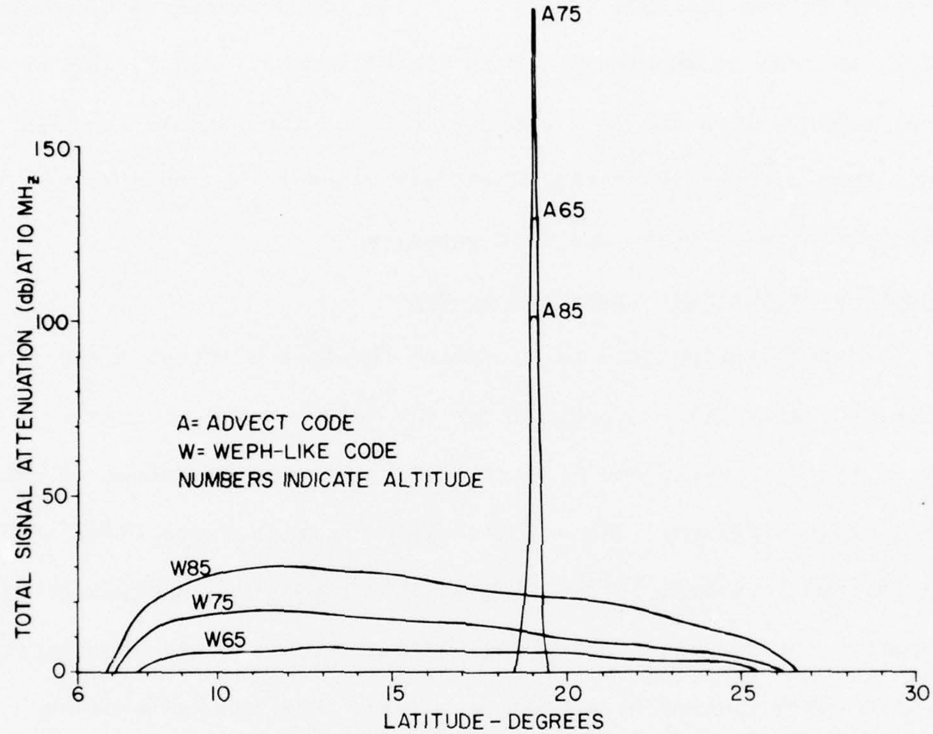

Fig. 5.9 — Total 10 MH_z wave attenuation (db) for east-west directed signal paths vs. latitude of signal path in degrees. Shown are plots for both the ADVECT and WEPH-like calculations at 65, 75 and 85 km signal path altitude.

place even at this late time. Also note the dependence of the total attenuation on the path direction (WEPH models would compute no path dependence for paths through the cloud center). It can be seen that the large differences in total wave attenuation along the same signal path are due to two distinct causes: 1) The cloud center is displaced in ADVECT, whereas it remains fixed in the WEPH model; and 2) the enhancement regions in ADVECT are ribbon-like, not the pancakes assumed in WEPH. Thus a signal path that WEPH determines to be inoperative could in fact be wide open, and vice-versa.

5.3 Accuracy of the Beta Transport Scheme

The prescription used to determine the free electron production rate, i.e. the analytic expressions for the beta induced ionization of atmosphere found in Knapp and Fischer (1970), has the advantage of being computationally efficient. We are interested here in summarizing the physical assumptions made in arriving at this analytical approximation and comparing the results, for typical cases, produced with this approximation with those yielded by a computationally less tractable method of known, high accuracy.

In both treatments betas are assumed to be emitted isotropically and to follow spiral paths along geomagnetic field lines. The following assumptions are also made in the Knapp and Fischer scheme:

1) The beta energy deposition coefficient μ_β, is independent of beta energy over the range involved.

2) The beta emission spectrum can be represented by

$$F(E) = \frac{1}{E_B} e - E/_{E_B} \quad \text{betas / MeV - beta}$$

where E_B is the average beta energy and F(E)dE represents the fraction of betas with the energy range between E and E + dE.

3) Energy absorbed from betas is localized in the region of the energy absorbing encounter.

4) There is no change in the pitch angle distribution due to atmospheric collisions.

5) Ionization due to electrons trapped in the geomagnetic field is negligible.

Under these assumptions the ionization rate per unit volume of atmosphere can be expressed as

$$q_\beta = N_i \mu_\beta \rho \int_0^1 \frac{F(\mu, B)}{\mu Bs/B} \quad e - \frac{m\mu_s}{E_\beta \mu} \quad d\mu \qquad (5.1)$$

where $F(\mu,B)\, d\mu$ is the number of betas with pitch angle cosines between μ and $\mu + d\mu$, n_i is the number of ion pairs created per unit energy deposited, B_s and B are the geomagnetic intensities at the source and deposition points respectively, ρ is the atmospheric mass density at the deposition point, and m is the atmospheric mass penetrated along the geomagnetic field line between the source and deposition points.

m is given by:

$$m = \frac{P - P_s}{g \sin \varphi} \qquad (5.2)$$

where φ is the magnetic dip angle and P and Ps are atmospheric pressures at the deposition and source points. Equation 5.2 derives from the assumption of hydrostatic equilibrium.

F (μ,B), the beta pitch angle distribution function, can be evaluated by noting that a beta will reflect or mirror when

$$\frac{B}{B_s} = \frac{1}{1-\mu_s^2} \qquad (5.3)$$

Since emission at the source is isotropic we, have

$$F\ (\mu_s, B_s)\ d\mu_s = \frac{N_\beta}{2}\ d\mu_s \qquad (5.4)$$

where N_B is the number of betas emitted per unit time, per unit volume. Under the assumption of negligible pitch angle scattering from atmospheric collisions the invariance of beta magnetic moment leads to

$$\frac{\sin \theta s}{\sqrt{B_s}} = \frac{\sin \theta}{\sqrt{B}}\ , \qquad (5.5)$$

From Eqs. (5.3), (5.4) and (5.5)

$$F(\mu,B) = \frac{N_\beta}{2} \frac{B_s}{B} \frac{\mu}{\sqrt{1 - \frac{B_s}{B}(1-\mu)^2}} \qquad (5.6)$$

By substituting Expressions (5.2) and (5.6) in Equation (5.1) and intergrating over μ the final expression for q_B becomes

$$q_\beta = N_\beta N_i \mu_\beta \rho \, E_1 \left(\frac{\mu_\beta (P_s - P)}{E_\beta \;/\sin\varphi} \right) \qquad (5.7)$$

where E_1 is the exponential integral defined by:

$$E_1(x) = \int_x e^{-t}/t \, dt$$

<u>An Alternative Energy Deposition Scheme</u>

The expression for the ionization rate due to the passage of betas through the atmosphere given in Eq. (5.1) was derived by assuming a constant energy deposition coefficient, μ_β, and integrating the exponential energy spectrum from $E = \mu_\beta\, m/\mu$ to $E = \mu_\beta\, m/\mu$, where m is the total mass penetrated along a geomagnetic field line. In general, μ_β is not a constant but an energy dependent variable arising from discrete energy losses suffered by an electron in an essentially random series of collisions with atmospheric atoms. These collisions with atomic electrons and nuclei result also in changes of direction, a factor which makes the total path length

and net depth of penetration unequal. If the electron energy is considerably greater than the binding energies of the atomic electrons encountered, then the details of atomic structure can be ignored and appropriate averages over various atomic characteristics may be used. The transport and energy deposition problem can be treated within either a Monte-Carlo or a diffusion equation framework, the latter being computationally more efficient if somewhat less flexible.

The virtue of going from a constant μ_β model to a more physically realistic one may be seen more easily if we first consider the problem of a planar source embedded in an infinite ocean of air, emitting monoenergetic, monodirectional electrons. Energy deposition profiles for 0.2, 0.4, 1.0 and 2.0 MeV electrons from transport calculations by Spencer (1959) are shown in Fig.(5.10) along with constant μ_β profiles. The value of μ_β is taken as 2 MeV-cm^2/gm, the optimum value used in the Knapp-Fischer scheme. The plots show that the constant coefficient assumption should cause an underestimate in the deposition from low energy electrons at high altitudes and an overestimate of the amount of energy reaching the lower altitudes. Most of the beta energy in the assumed exponential spectrum falls within the 0.2 - 2.0 MeV range of these plots since the average energy, E_β , varies from 1.0 MeV a few minutes after detonation to 0.7 MeV a few hours later.

The choice of a suitable electron transport scheme was made on the basis of the availability of an efficient computer code (Strickland et. al., (1975)) for solving the Fokker-Planck equation. The

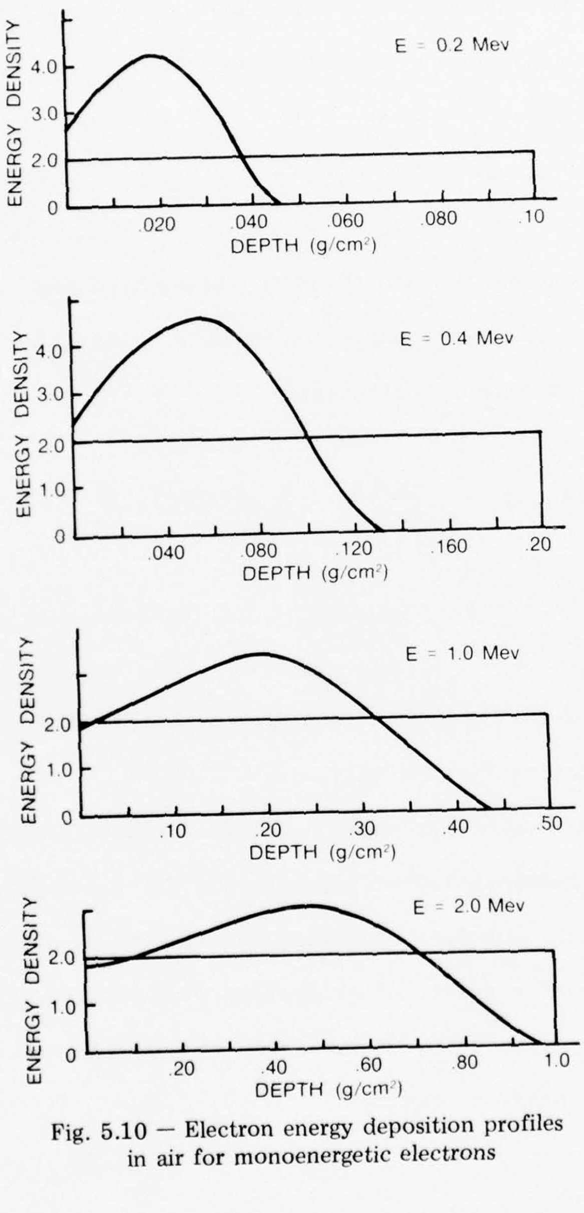

Fig. 5.10 — Electron energy deposition profiles in air for monoenergetic electrons

form of the equation applicable here has the *distribution function* Φ expressed in terms of the variables μ, E and τ where μ is the cosine of the orbit pitch angle, E is the electron kinetic energy and τ is an effective column density given by

$$d\tau = n(z)\, \sigma_T (E)\, dz$$

where n (z) is the mass density of the atmosphere and σ_T is the sum of the ionization, excitation and elastic collision cross sections. The equation is expressed in the form:

$$\mu \frac{\partial \Phi}{\partial t} (\tau, E, \mu) = \frac{Q(E)}{2\upsilon\ (E)} \frac{2}{\partial \mu} \left[(1-\mu^2) \frac{\partial \Phi}{\partial \mu} \right]$$

$$+ \frac{1}{\sigma\ (E)} \frac{\partial}{\partial E} \left(L\ (E)\ \Phi \right)$$

where Z (E) and L (E) are the momentum transfer cross section and energy loss functions respectively.

The original low energy version of the Fokker-Planck solver was modified by the substitution of relativistic cross sections for non-relativistic ones. The loss of energy suffered by an electron per unit path length as a result of collisions with orbital electrons of the medium is given by the formulation of Rohrlich and Carlson (1954) of the Bethe-Block theory:

$$L(E) = \frac{0.1536}{\beta^2} \left(\sum \omega_i \frac{Z_i}{A_i} \right) \left\{ \ln \left[\frac{T^2(T+2)}{2(I/mc^2)^2} \right] + 1-\beta^2 \right.$$

$$\left. + \left[T^2/8 - (2T+1) \ln 2 \right] / (T+1)^2 \right\}$$

where $L(T)$ is the average energy loss per unit path length ($MeV\text{-}cm^2/gm$) ; E is the electron kinetic energy (MeV), mc^2 is the electron rest mass energy, $T = E/mc^2$; $\beta = v/c$ and Z_i, A_i, and ω_i are the atomic weight, atomic number, and the fraction by mass of the i'th constituent of the medium. I is the mean excitation energy of the medium, taken as 96.8 eV for air.

The momentum transfer cross section was calculated using the screened Rutherford cross section of Goudsmit and Saunderson (1940) multiplied by a spin factor evaluated by McKinley and Feschback (1948). This differential cross section for scattering into solid angle $2\pi \sin\theta \, d\theta$ is given by:

$$\frac{d\sigma}{d\Omega} = \frac{z^2 e^4}{m^2 v^4} \frac{1}{(1-\cos\theta + 2\eta)^2} \left\{ 1 - \frac{1}{2} \beta^2 (1-\cos\theta) \right.$$

$$\left. + \frac{\pi\alpha\beta}{\sqrt{2}} (1-\cos\theta)^{\frac{1}{2}} \left(1 - \frac{(1-\cos\theta)^{\frac{1}{2}}}{\sqrt{2}}\right) \right\}$$

where $\alpha = \frac{z}{137}$.

The code incorporating these modifications was checked by duplicating a case studied by Berger, Seltzer, and Maeda (1970) involving energy deposition in the atmosphere by electrons with an exponential energy spectrum with average energy 200 KeV. The Berger et. al. study utilized a Monte-Carlo code. The deposition profile provided by the Fokker-Planck code duplicated the Monte-Carlo results within the bounds of the accuracy of the graphical display provided by Berger et. al.

Conclusions

In order to access the limitations of the simple constant energy deposition scheme it was compared to Fokker-Planck results for two cases: $E_\beta = 0.8$ MeV and $E_\beta = 1.0$ MeV. The first is characteristic of a beta spectrum about an hour after detonation, the second about a few seconds after detonation. The energy deposition results, plotted in Figs.(5.11) and (5.12) show that the simple model agrees quite well with the Fokker-Planck curves between 60 km and 90 km altitude, with the disparity typically 30% or smaller. At 50 km and below, where the deposition falls off, this disparity between the treatments increases rapidly to an order of magnitude and greater, reflecting differences seen in the deposition curves for monochromatic betas. These results are for an exponential spectrum, but should hold equally for an empirical beta spectrum.

The assumption of a constant energy deposition coefficient is, therefore, adequate in the region where the deposition peaks. Outside of this peak region this assumption fails to provide reasonable answers and the Fokker-Planck scheme represents a possible alternative.

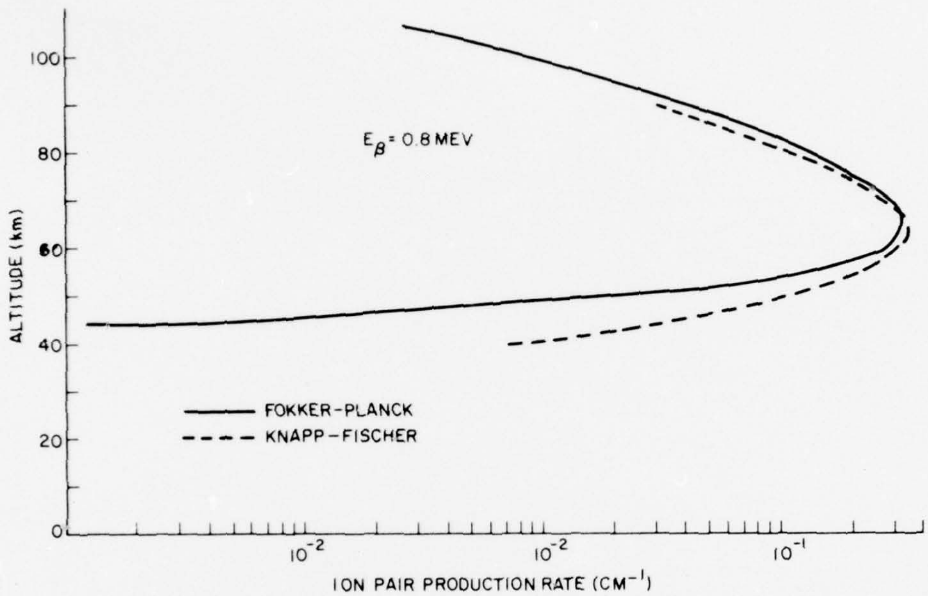

Fig. 5.11 — Comparison of ion pair production rate profiles for Fokker-Planck and Knapp-Fischer models. E_β = 0.8 MeV.

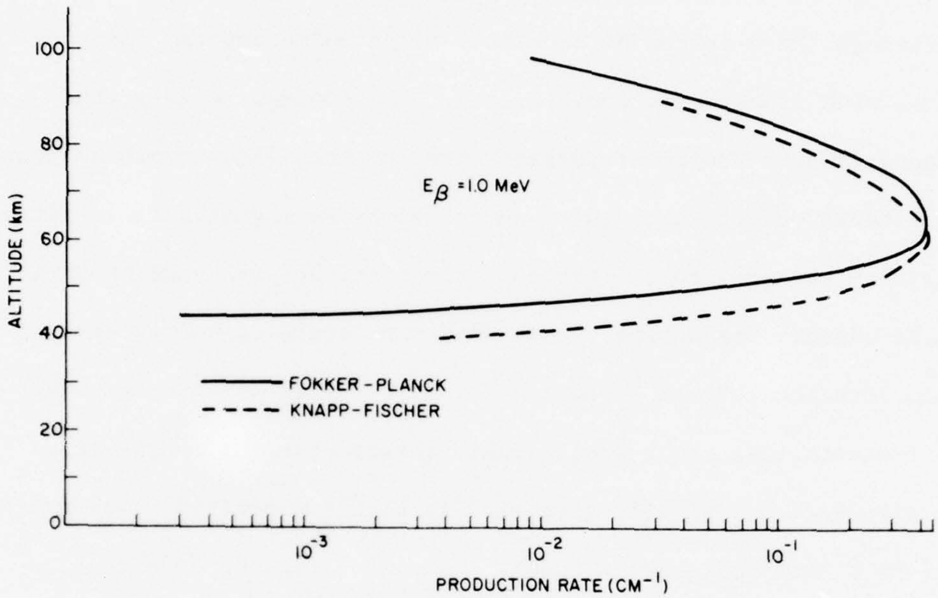

Fig. 5.12 — Similar to 5.11 except that E_β = 1.0 MeV

Section 6

SUMMARY

Radioactive debris clouds from high altitude nuclear explosions ionize air in the magnetically conjugate regions at lower altitudes primarily through the emission of energetic betas which undergo ionizing collisions with atmospheric constituents. The ionized regions thus formed constitute a source of interference for satellite communications. Since the betas are constrained to spiral along geomagnetic field lines, the beta flux pattern, to a first approximation, has the same shape as the debris cloud. The debris cloud, on a time scale of hours, changes shape and location through advection by mesospheric winds. Past NRL results indicate that short scale length shears observed in the mesospheric circulation typically give rise to highly elongated cloud configurations within hours after burst. The understanding of such late time HANE effects is, therefore, critically dependent on knowledge of upper atmosphere wind patterns.

This past year, NRL has completed an analysis of observational data on mesospheric winds, in particular, the climatological model given by Groves, CIRA (1972). The model was found to have large systematic errors attributable, primarily, to tidal components and planetary waves which remain unresolved in the sparse data field. NRL has developed theoretical dynamical models of the upper atmosphere which, in conjunction with observational data, will provide a reliable predictive capability for the mesospheric circulation.

The circulation of the upper atmosphere is thermally driven by insolation which varies in time and space. Radiative heating functions

have been developed to replace earlier, less accurate ones by Leovy (1964) used in the NRL linear model of the mean mesospheric circulation. The heating functions are produced by a computer program which can be used to provide either mean seasonal heating rates for use in climatological forecasts or point-by-point local heating rates suitable for solar tidal calculations (diurnal and semi-diurnal time scales). The new heating function has been incorporated into the NRL linear mesospheric model and test runs have indicated that the model accurately simulates the observed mean zonal flow for both solstitial and equinoctial conditions.

Superimposed on the mean mesospheric circulation are planetary waves on a diurnal time scale which react non-linearly with each other and with the mean wind current. This solar-driven tidal fluctuation has been modeled at NRL with a non-linear semi-spectral numerical scheme which has successfully simulated both the diurnal and semi-diurnal modes of the tide. This program has been improved in the past year with major changes in the lower boundary condition and increased resolution in the computational grid. Comparison of results from this model with analytic results from Lindzen (1971) reveal excellent agreement.

The overall goal of the NRL effort is the development of a numerical model which, given wind and bomb data, tracks the advection of debris, computes the equilibrium distribution of beta induced ionization at specified time, and then determines communication signal attenuation by ray tracing. This program has been completed with the incorporation of beta deposition routines based on analytic expressions given by Knapp and Fischer (1970). These approximate expressions have been found to agree within $\pm$ 20% with a more rigorous NRL electron

transport code based on the Fokker-Planck equation, in the regions of peak ionization.

ACKNOWLEDGEMENT

The authors would like to acknowledge the many helpful suggestions and information received from the staff members and particularly, the assistance of Dr. T. Coffey. They would also like to thank Dr. J. Block for assembling this report.

REFERENCES

Baker, L. and D. Strobel (1975_a), Linear models of mesospheric circulation, NRL Memorandum Report 3101, 22 pp.

Baker, L. and D. Strobel (1975_b), Linear models of mesospheric circulation II: development and applications of heating functions, NRL Memorandum Report 3222, 15 pp.

Belmont, A. D., D. G. Dartt and G. D. Nastrom (1975), Variations of stratospheric zonal winds, 20-65 km, 1961-1971, J. App. Met. 14, 585-594.

Berger, M. J., S. M. Seltzer, and K. Maeda, Energy, deposition by auroral electrons in the atmosphere, J. Atmos. Terr. Phys., 32, 1015, 1970.

Blake, D. W., Simplified photochemical models and their applications in the stratosphere & mesosphere (Thesis, U. of Chicago).

Chapman, W. A., M. J. Cross, D. A. Flower, G. E. Peckham and S. D. Smith (1974), A spectral analysis of global atmospheric temperature fields observed by the selective chopper radiometer on the Nimbus 4 satellite during the year 1970-71, Proc. Roy. Soc. Lond. A. 338, 57-76.

Charney, J. G. and P. G. Drazin, Propagation of planetary-scale from the lower atmosphere into the upper atmosphere, J. Geophys. Res. 66, 83-109, (1961).

Charney, J. G. and M. E. Stern, On the stability of internal baro-clinic jets in a rotating atmosphere, J. Atmos. Sci. 19, 159-172, (1962).

COSPAR International Reference Atmosphere (1965), (North Holland, Amsterdam).

COSPAR International Reference Atmosphere (1972), (Academie Verlag,Berlin).

Dickinson, R. E., Baroclinic instability of an unbounded zonal shear flow in a compressible atmosphere, J. Atmos. Sci. 30, 1520-1527, (1973).

Ebel, A., Heat and momentum sources of mean circulation at an altitude of 70 to 100 km, Tellus 26, 325-333, (1974).

Fukuyama, K. Latitudinal Distributions of Minor Neutral Hydrogen-Oxygen constituents in the Winter Mesosphere and Lower Thermosphere, J. Atmos. Terr. Phys., 36, 1297-1320, 1974a.

Fukuyama, K. Latitudinal Distributions of Photochemical Heating Rates in the Winter Mesosphere and Lower Thermosphere, J. Atmos. Terr. Phys. 36, 1321-1334, 1974b.

Glass, M. and A. Spizzichino, Waves in the lower thermosphere: recent experimental investigations, J. Atmos. Terr. Phys. 36, 1825-1839, (1974).

Goudsmit, G. A., and J. L. Saunderson, Phys. Rev., 57 36 (1940).

Grammeltvedt, A., A survey of finite-difference schemes for the primitive equations for a barotopic fluid, Mon. Weather Rev., 97, 384-404, (1970).

Groves, G. V., Wind models from 60 to 130 km altitude for different months and latitudes, J. Brit. Interplanet. Soc. 22, 285-307, (1969).

Houghton, D. D., W. L. Jones, A numerical model for linearized gravity and acoustic waves, J. Comp. Phys., 3, 339-357, (1969).

Knapp, W. S. and P. G. Fischer, Aids for the study of electromagnetic blackout, DASA 2499, Defense Atmoic Support Agency, Washington, D. C. 1970.

Kriester, B., Large scale circulation patterns of the stratosphere, Space Sci. Rev. 13, 258-273, (1972).

Krueger, A. J. Heath, D. F., Carlton, L. M., Variations in the Stratospheric Ozone Field Inferred from Nimbus Satellite Observations PAGEOPH, 106-108, 1258-1280, 1973.

Kurihara, Y., On the use of implicit and iterative methods for the time integration of the wave equation, Mon. Weather Rev., 93, 33-46, (1965).

Leovy, C., Radiative Equilibrium of the Mesosphere, J. A. S., 21, 238-248, 1964a.

Leovy, D., Simple Models of Thermally Driven Mesospheric Circulation, J. A. S., 21, 327-341, 1964b

Leovy, C. and T. Ackerman, Evidence for high-frequency synoptic disturbances near the strato pause, J. Atmos. Sci. 30, 940-941, (1973)

Lindzen, R. S., Thermally driven diurnal tide in the atmosphere, Quart. J. R. Met. Soc. 93, 18-42, (1967).

Lindzen, R., E. S. Batten, K. W. Kim, Oscillations in atmospheres with tops, Mon. Weather Rev., 96, 133-140 (1968).

Lindzen, R., Mathematical problems in the geophysical sciences, Lecturers in Applied Mathematics, 14, 293-360 (1971).

Lindzen, R. S., Will, D. J. An Analytic Formula for Heating Due to Ozone Absorption, J.A.S. 30, 313-315, 1973.

Lindzen, R., S. S. Hong, Effects of mean winds and horizontal temperature gradients on solar and lunar simi-diurnal tides in the atmosphere, J. Atmos. Sci., 31, 1421-1446 (1974).

Madala, R., S. A. Piacsek and S. T. Zalesak (1975), A semi-spectral numerical model for forced vertically propagating planetary waves, part I - application of the model to linear diurnal and semi-diurnal atmospheric thermal tides, NRL Memorandum Report 3145, 40 pp.

McKinley, W. A., and H. Feshback, Phys. Rev., 74, 1759, (1948).

Park, J. H. and J. London, Ozone photochemistry and radiative heating of the middle atmosphere, J. Atmos. Sci. 31, 1898-1961 (1974).

Quiroz, R. S. (1969), Meteorological rocket research since 1959 and current requirements for observation and analysis above 60 kilometers, NASA Contractor Report CR-1293, NASA, Washington, D.C., 1-66.

Schoeberl, M. R. (1975), The propagation of planetary scale waves into the upper atmosphere, Ph.D. Thesis, University of Illinois, 1-270.

Simmons, A. J., Baroclinic instability at the winter stratopause, Quart. J. R. Met. Soc. 100, 531-540, (1974).

Rohrlich F. and B. L. Carlson, Positron-Electron differences in energy loss and multiple scattering, Phys. Rev., 93, 38, (1954).

Spencer, L. V., Energy dissipation by fast electrons, National Bureau of Standards Monograph 1, Washington, D. C. (1959).

Strickland, D. J., D. L. Book, T. P. Coffey and J. A. Fedder, Transport Techniques for describing scattering and energy deposition of energetic auroral electrons, NRL Memorandum Report 3117, Naval Research Laboratory, Washington, D. C.

Trenberth, D. E., Global Model of the General Circulation of the Atmosphere Below 75 Kilometers with an Annual Heating Cycle, Monthly Weather Review, 101, 287-321, 1973.

van Loon, H., R. L. Jenne and K. Labitzke, Zonal harmonic standing waves, J. Geophys. Res. 78, 4463-4471, (1973).

Yanowitch, M., A numerical study of vertically propagating waves in a viscous isothermal atmosphere, J. Comp. Phy., 4, 531, 1969

Zalesak, S. and T. Coffey (1975), Advection of artificially produced upper atmospheric clouds in empirically determined wind Fields, NRL Memorandum Report 3046, Naval Research Laboratory, Washington, D.C., 1-27.

DEPARTMENT OF DEFENSE

DIRECTOR
COMMAND CONTROL TECHNICAL CENTER
PENTAGON RM BE 685
WASHINGTON, D.C. 20301
    01CY ATTN C-650 G. C. JONES
    01CY ATTN C-650 W. HEIDIG
    01CY ATTN C-312 R. MASON

DIRECTOR
DEFENSE ADVANCED RSCH PROJ AGENCY
ARCHITECT BUILDING
1400 WILSON BLVD.
ARLINGTON, VA. 22209
    01CY ATTN NUCLEAR MONITORING RESEARCH
    01CY ATTN STRATEGIC TECH OFFICE

DEFENSE COMMUNICATION ENGINEER CENTER
1860 WIEHLE AVENUE
RESTON, VA. 22090
    01CY ATTN CODE R820 R. L. CRAWFORD
    01CY ATTN CODE R410 JAMES W. MCLEAN

DIRECTOR
DEFENSE COMMUNICATIONS AGENCY
WASHINGTON, D.C. 20305
    (ADR CNWDI: ATTN CODE 240 FOR)
    01CY ATTN CODE 480
    01CY ATTN CODE 810 R. W. ROSTRON
    01CY ATTN CODE 101B MAJ R. ROOD
    01CY ATTN MAUREY RAFFENSPERGER

DEFENSE DOCUMENTATION CENTER
CAMERON STATION
ALEXANDRIA, VA. 22314
    (12 COPIES IF OPEN PUBLICATION, OTHERWISE 2 COPIES)
    12CY ATTN TC

DIRECTOR
DEFENSE INTELLIGENCE AGENCY
WASHINGTON, D.C. 20301
    01CY ATTN DT-1B
    01CY ATTN W. WITTIG DC-7D

DIRECTOR
DEFENSE NUCLEAR AGENCY
WASHINGTON, D.C. 20305
01CY ATTN STSI ARCHIVES
01CY ATTN STVL
03CY ATTN STTL TECH LIBRARY
01CY ATTN DDST
03CY ATTN RAAE

DIR OF DEFENSE RSCH & ENGINEERING
DEPARTMENT OF DEFENSE
WASHINGTON, D.C. 20301
01CY ATTN S&SS (OS)

COMMANDER
FIELD COMMAND
DEFENSE NUCLEAR AGENCY
KIRTLAND AFB, NM 87115
01CY ATTN FCPR

DIRECTOR
INTERSERVICE NUCLEAR WEAPONS SCHOOL
KIRTLAND AFB, NM 87115
01CY ATTN DOCUMENT CONTROL

DIRECTOR
JOINT STRAT TGT PLANNING STAFF JCS
OFFUTT AFB
OMAHA, NB 68113
01CY ATTN JLTW-2
01CY ATTN JPST CAPT G. D. GOETZ

CHIEF
LIVERMORE DIVISION FLD COMMAND DNA
LAWRENCE LIVERMORE LABORATORY
P. O. BOX 808
LIVERMORE, CA 94550
01CY ATTN FCPRL

DIRECTOR
NATIONAL SECURITY AGENCY
FT. GEORGE G. MEADE, MD 20755
01CY ATTN JOHN SKILLMAN R52
01CY ATTN FRANK LEONARD
01CY ATTN W14 PAT CLARK

OJCS/J-3
THE PENTAGON
WASHINGTON, D.C. 20301
(OPERATIONS)
01CY ATTN WWMCCS EVAL OFC MR. TOMA

ASD (C31) (SYSTEMS)
3D224, THE PENTAGON
WASHINGTON, D.C. 20301
01CY ATTN DR. M. EPSTEIN
01CY DR. J. BABCOCK

WWMCCS SYSTEM ENGINEERING ORG
WASHINGTON, D.C. 20305
01CY ATTN R. L. CRAWFORD

COMMANDER/DIRECTOR
ATMOSPHERIC SCIENCES LABORATORY
U.S. ARMY ELECTRONICS COMMAND
WHITE SANDS MISSILE RANGE, NM 88002
01CY ATTN DRSEL-BL-SY-S F. E. NILES

DIRECTOR
BMD ADVANCED TECH CTR
HUNTSVILLE OFFICE
P. O. BOX 1500
HUNTSVILLE, AL 35807
01CY ATTN ATC-T MELVIN T. CAPPS
01CY ATTN ATC-O W. DAVIES
01CY ATTN ATC-R DON RUSS

PROGRAM MANAGER
BMD PROGRAM OFFICE
5001 EISENHOWER AVENUE
ALEXANDRIA, VA 22333
01CY ATTN DACS-BMT JOHN SHEA

CHIEF C-E SERVICES DIVISION
U.S. ARMY COMMUNICATIONS CMD
PENTAGON RM 1B269
WASHINGTON, D.C. 20310
01CY ATTN CC-OPS-CE

COMMANDER
HARRY DIAMOND LABORATORIES
2800 POWDER MILL ROAD
ADELPHI, MD 20783
(CNWDI-INNER ENVELOPE: ATTN: DRXDO-RBH)
01CY ATTN MILDRED H. WEINER DRXDO-TI
01CY ATTN DRXDO-RB ROBERT WILLIAMS
01CY ATTN DRXDO-NP FRANCIS N. WIMENITZ
01CY ATTN DRXDO-NP CYRUS MOAZED

DIRECTOR
TRASANA
WHITE SANDS MISSILE RANGE, NM 88002
01CY ATTN ATAA-SA
01CY ATTN TCC/F. PAYAN JR
01CY ATTN ATAA-TAC LTC JOHN HESSE

COMMANDER
U.S. ARMY COMM-ELEC ENGRG INSTAL AGY
FT. HUACHUCA, AZ 85613

01CY ATTN EED-PED GEORGE LANE

COMMANDER
U.S. ARMY ELECTRONICS COMMAND
FORT MONMOUTH, NJ 07703
01CY ATTN DRSEL-NL-RD H. S. BENNET
01CY ATTN DRSEL-PL-ENV HANS A. BOMKE

COMMANDER
U.S. ARMY FOREIGN SCIENCE & TECH CTR
220 7TH STREET, NE
CHARLOTTESVILLE, VA 22901
01CY ATTN P. A. CROWLEY
01CY ATTN R. JONES

COMMANDER
U.S. ARMY MATERIEL DEV & READINESS CMD
5001 EISENHOWER AVENUE
ALEXANDRIA, VA 22333
01CY ATTN DRCLDC J. A. BENDER

COMMANDER
U.S. ARMY NUCLEAR AGENCY
FORT BLISS, TX 79916
01CY ATTN MONA-WE J. BERBERET

DIRECTOR
U.S. ARMY BALLISTIC RESEARCH LABS
ABERDEEN PROVING GROUND, MD 21005
01CY ATTN LAWRENCE J. PUCKETT

COMMANDER
U.S. ARMY SATCOM AGENCY
FT. MONMOUTH, NJ 07703
01CY ATTN DOCUMENT CONTROL

COMMANDER
U.S. ARMY MISSILE INTELLIGENCE AGENCY
REDSTONE ARSENAL, AL 35809
01CY ATTN JIM GAMBLE

CHIEF OF NAVAL OPERATIONS
NAVY DEPARTMENT
WASHINGTON, D.C. 20350
01CY ATTN OP 943 LCDR HUFF
01CY ATTN ALEXANDER BRANDT
01CY ATTN RONALD E. PITKIN

CHIEF OF NAVAL RESEARCH
NAVY DEPARTMENT
ARLINGTON, VA 22217
01CY ATTN CODE 418
01CY ATTN CODE 461

COMMANDER
NAVAL ELECTRONIC SYSTEMS COMMAND
NAVAL ELECTRONIC SYSTEMS CMD HQS
WASHINGTON, D.C. 20360
01CY ATTN NAVALEX 034 T BARRY HUGHES
01CY ATTN PME 117-T SATELLITE COMM PROJECT OFF
01CY ATTN PME 117

COMMANDING OFFICER
NAVAL INTELLIGENCE SUPPORT CTR
4301 SUITLAND ROAD, BLDG. 5
WASHINGTON, D.C. 20390
01CY ATTN MR. DUBBIN STIC 12

COMMANDER
NAVAL OCEAN SYSTEMS CENTER
SAN DIEGO, CA 92152
01CY ATTN WILLIAM F. MOLER
01CY ATTN CODE 0230 C. BAGGETT
03CY ATTN CODE 2200
01CY ATTN R. EASTMAN

DIRECTOR
NAVAL RESEARCH LABORATORY
WASHINGTON, D.C. 20375
01CY ATTN CODE 7700 TIMOTHY P. COFFEY
01CY ATTN CODE 5460 ELECTROMAG PROP BR
01CY ATTN CODE 5430
03CY ATTN CODE 7701 JACK D. BROWN
01CY ATTN HDQ COMM DIR BRUCE WALD (CODE 5400)
01CY ATTN CODE 5465 PROP APPLICATIONS
01CY ATTN CODE 5461 TRANS IONO PROP
01CY ATTN CODE 7750

COMMANDER
NAVAL SPACE SURVEILLANCE SYSTEM
DAHLGREN, VA 22448
01CY ATTN CAPT J. H. BURTON

COMMANDER
NAVAL SURFACE WEAPONS CENTER
WHITE OAK, SILVER SPRING, MD 20910
01CY ATTN CODE WA501 NAVY NUC PRGMS OFF

DIRECTOR
STRATEGIC SYSTEMS PROJECT OFFICE
NAVY DEPARTMENT
WASHINGTON, D.C. 20376
01CY ATTN NSP-2141
01CY ATTN NSSP-2722 FRED WIMBERLY

NAVAL SPACE SYSTEM ACTIVITY
P. O. BOX 92960
WORLDWAY POSTAL CENTER
LOS ANGELES, CALIF. 90009
01CY ATTN A. B. HAZZARD

COMMANDER
ADC/DC
ENT AFB, CO 80912
01CY ATTN DC MR. LONG

COMMANDER
ADCOM/XPD
ENT AFB, CO 80912
    01CY ATTN XPQDQ

AF GEOPHYSICS LABORATORY, AFSC
HANSCOM AFB, MA 01731
    01CY ATTN OPR HAROLD GARDNER
    01CY ATTN OPR JAMES C. ULWICK
    01CY ATTN LKB KENNETH S. W. CHAMPION
    01CY ATTN OPR ALVA T. STAIR
    01CY ATTN SUOL RSCH LIB
    01CY ATTN PHP JULES AARONS
    01CY ATTN PHD JURGEN BUCHAU
    01CY ATTN PHD JOHN P. MULLEN

AF WEAPONS LABORATORY, AFSC
KIRTLAND AFB, NM 87117
    01CY ATTN SUL
    01CY ATTN CA ARTHUR H. GUENTHER
    01CY ATTN DYC CAPT L. WITTWER
    01CY ATTN SAS JOHN M. KAMM
    01CY ATTN DYC CAPT MARK A. FRY

AFTAC
PATRICK AFB, FL 32925
    01CY ATTN TF/MAJ WILEY
    01CY ATTN TN

AIR FORCE AVIONICS LABORATORY, AFSC
WRIGHT-PATTERSON AFB, OH 45433
    01CY ATTN AAD WADE HUNT
    01CY ATTN AFAL AAB H. M. HARTMAN
    01CY ATTN AAD ALLEN JOHNSON

HEADQUARTERS
ELECTRONIC SYSTEMS DIVISION/XR
HANSCOM AFB, MA 01731
    01CY ATTN XRC LTC J. MORIN
    01CY ATTN XRE LT MICHAELS

HEADQUARTERS
ELECTRONIC SYSTEMS DIVISION/YS
HANSCOM AFB, MA 01731
    01CY ATTN YSEV

COMMANDER
FOREIGN TECHNOLOGY DIVISION, AFSC
WRIGHT-PATTERSON AFB, OH 45433
    01CY ATTN NICD LIBRARY
    01CY ATTN ETD B. L. BALLARD

HQ USAF/RD
WASHINGTON, D.C. 20330
    01CY ATTN RDQ

COMMANDER
ROME AIR DEVELOPMENT CENTER, AFSC
GRIFFISS AFB, NY 13440
    01CY ATTN EMTLD DOC LIBRARY
    01CY ATTN OCSE V. COYNE

SAMSO/SZ
POST OFFICE BOX 92960
WORLDWAY POSTAL CENTER
LOS ANGELES, CA 90009
(SPACE DEFENSE SYSTEMS)
    01CY ATTN SZJ MAJOR LAWRENCE DOAN

COMMANDER IN CHIEF
STRATEGIC AIR COMMAND
OFFUTT AFB, NB 68113
    01CY ATTN XPFS MAJ BRIAN G. STEPHAN
    01CY ATTN ADWATE CAPT BRUCE BAUER
    01CY ATTN NRT

HEADQUARTERS
ELECTRONIC SYSTEMS DIVISION (AFSC)
HANSCOM AFB, MA 01731
    01CY ATTN JIM DEAS

SAMSO/YA
P. O. BOX 92960
WORLDWAY POSTAL CENTER
LOS ANGELES, CA 90009
    01CY ATTN YAT CAPT L. BLACKWELDER

SAMSO/SK
P. O. BOX 92960
WORLDWAY POSTAL CENTER
LOS ANGELES, CA 90009
    01CY ATTN SKA LT MARIA A. CLAVIN

SAMSO/MN
NORTON AFB, CA 92419
(MINUTEMAN)
    01CY ATTN MNNL LTC KENNEDY

COMMANDER
ROME AIR DEVELOPMENT CENTER, AFSC
HANSCOM AFB, MA 01733
    01CY ATTN ETEI A. LORENTZEN

U.S. ENERGY RSCH AND DEV ADMIN

EG&G, INC.
LOS ALAMOS DIVISION
P. O. BOX 809
LOS ALAMOS, NM 85544
    01CY ATTN JAMES R. BREEDLOVE

UNIVERSITY OF CALIFORNIA
LAWRENCE LIVERMORE LABORATORY
P. O. BOX 808
LIVERMORE, CA 94550
    01CY ATTN TECH INFO DEPT L-3
    01CY ATTN RONALD L. OTT L-531
    01CY ATTN DONALD R. DUNN L-156
    01CY ATTN RASPH S. HAGER L-31

LOS ALAMOS SCIENTIFIC LABORATORY
P. O. BOX 1663
LOS ALAMOS, NM 87545
    01CY ATTN DOC CON FOR ERIC LINDMAN
    01CY ATTN DOC CON FOR R. F. TASCHEK
    01CY ATTN DOC CON FOR ERIC JONES
    01CY ATTN DOC CON FOR JOHN S. MALIK
    01CY ATTN DOC CON FOR MARTIN TIERNEY J-10
    01CY ATTN DOC CON FOR JOHN ZINN

SANDIA LABORATORIES
P. O. BOX 5800
ALBUQUERQUE, NM 87115
    01CY ATTN DOC CON FOR J. P. MARTIN ORG 1732
    01CY ATTN DOC CON FOR W. D. BROWN ORG 1353
    01CY ATTN DOC CON FOR A. DEAN THORNBROUGH ORG 1245
    01CY ATTN DOC CON FOR T. WRIGHT
    01CY ATTN DOC CON FOR D. A. DAHLGREN ORG 1722

OTHER GOVERNMENT

DEPARTMENT OF COMMERCE
OFFICE OF TELECOMMUNICATIONS
INSTITUTE FOR TELECOM SCIENCE
BOULDER, CO 80302
    01CY ATTN WILLIAM F. UTLAUT
    01CY ATTN G. REED

NATIONAL OCEANIC & ATMOSPHERIC ADMIN
ENVIRONMENTAL RESEARCH LABORATORIES
DEPARTMENT OF COMMERCE
BOULDER, CO 80302
    01CY ATTN JOSEPH H. POPE
    01CY ATTN RICHARD GRUBB
    01CY ATTN C. L. RUFFNACH

NASA
GODDARD SPACE FLIGHT CENTER
GREENBELT, MD 20771
    01CY ATTN ATS-6 OFC P. CORRIGAN

DEPARTMENT OF DEFENSE CONTRACTORS

AEROSPACE CORPORATION
P. O. BOX 92957
LOS ANGELES, CA 90009
    01CY ATTN IRVING M. GARFUNKEL
    01CY ATTN T. M. SALMI
    01CY ATTN V. JOSEPHSON
    01CY ATTN S. P. BOWER
    01CY ATTN N. D. STOCKWELL
    01CY ATTN P. P. OLSEN 120 RM 2224E
    01CY ATTN F. E. BOND RM 5003
    01CY ATTN J. E. CARTER 120 RM 2209
    01CY ATTN F. A. MORSE A6 RM 2407

ANALYTICAL SYSTEMS ENGINEERING CORP
5 OLD CONCORD ROAD
BURLINGTON, MA 01803
    01CY ATTN RADIO SCIENCES

BOEING COMPANY, THE
P. O. BOX 3707
SEATTLE, WA 98124
    01CY ATTN GLEN KEISTER
    01CY ATTN D. MURRAY

CALIFORNIA AT SAN DIEGO, UNIV OF
3175 MIRAMAR ROAD
LA JOLLA, CA 92037
    01CY ATTN HENRY G. BOOKER

BROWN ENGINEERING COMPANY, INC.
CUMMINGS RESEARCH PARK
HUNTSVILLE, AL 35807
    01CY ATTN ROMEO A. DELIBERIS

CHARLES STARK DRAPER LABORATORY, INC.
555 TECHNOLOGY SQUARE
CAMBRIDGE, MA 02139
    01CY ATTN D. B. COX
    01CY ATTN J. P. GILMORE MS 63

COMPUTER SCIENCES CORPORATION
P. O. BOX 530
6565 ARLINGTON BLVD
FALLS CHURCH, VA 22046
    01CY ATTN H. BLANK
    01CY ATTN JOHN SPOOR

COMSAT LABORATORIES
LINTHICUM ROAD
CLARKSBURG, MD 20734
    01CY ATTN R. R. TAUR

CORNELL UNIVERSITY
DEPARTMENT OF ELECTRICAL ENGINEERING
ITHACA, NY 14850
    01CY ATTN D. T. FARLEY JR

ESL INC.
495 JAVA DRIVE
SUNNYVALE, CA 94086
    01CY ATTN R. K. STEVENS
    01CY ATTN J. ROBERTS
    01CY ATTN JAMES MARSHALL
    01CY ATTN V. L. MOWER
    01CY ATTN C. W. PRETTIE

FORD AEROSPACE & COMMUNICATIONS CORP
3939 FABIAN WAY
PALO ALTO, CA 94303
    01CY ATTN J. T. MATTINGLEY MS X22

GENERAL ELECTRIC COMPANY
SPACE DIVISION
VALLEY FORGE SPACE CENTER
GODDARD BLVD KING OF PRUSSIA
P. O. BOX 8555
PHILADELPHIA, PA 19101
    01CY ATTN M. H. BORTNER SPACE SCI LAB

GENERAL ELECTRIC COMPANY
TEMPO-CENTER FOR ADVANCED STUDIES
816 STATE STREET (P.O. DRAWER QQ)
SANTA BARBARA, CA 93102
01CY ATTN DASIAC
01CY ATTN DON CHANDLER
01CY ATTN TOM BARRETT
01CY ATTN TIM STEPHENS
01CY ATTN WARREN S. KNAPP
01CY ATTN WILLIAM MCNAMERA
01CY ATTN B. GAMBILL
01CY ATTN MACK STANTON

GENERAL RESEARCH CORPORATION
P. O. BOX 3587
SANTA BARBARA, CA 93105
01CY ATTN JOHN ISE JR
01CY ATTN JOEL GARBARINO

GEOPHYSICAL INSTITUTE
UNIVERSITY OF ALASKA
FAIRBANKS, AK 99701
(ALL CLASS ATTN: SECURITY OFFICER)
01CY ATTN T. N. DAVIS (UNCL ONLY)
01CY ATTN NEAL BROWN (UNCL ONLY)
01CY ATTN TECHNICAL LIBRARY

GTE SYLVANIA, INC.
ELECTRONICS SYSTEMS GRP-EASTERN DIV
77 A STREET
NEEDHAM, MA 02194
01CY ATTN MARSHAL CROSS

INSTITUTE FOR DEFENSE ANALYSES
400 ARMY-NAVY DRIVE
ARLINGTON, VA 22202
01CY ATTN J. M. AEIN
01CY ATTN ERNEST BAUER
01CY ATTN HANS WOLFHARD
01CY ATTN JOEL BENGSTEN

HARRIS CORP, E.S.D.
P. O. BOX 37
MELBOURNE, FL 32901
01CY ATTN ADV PROG DEPT DR. CARL DAVIS

HSS, INC.
2 ALFRED CIRCLE
BEDFORD, MA 01730
    01CY ATTN DONALD HANSEN

INTL TEL & TELEGRAPH CORPORATION
500 WASHINGTON AVENUE
NUTLEY, NJ 07110
    01CY ATTN TECHNICAL LIBRARY

JAYCOR
1401 CAMINO DEL MAR
DEL MAR, CA 92014
    01CY ATTN S. R. GOLDMAN

JOHNS HOPKINS UNIVERSITY
APPLIED PHYSICS LABORATORY
JOHNS HOPKINS ROAD
LAUREL, MD 20810
    01CY ATTN DOCUMENT LIBRARIAN
    01CY ATTN THOMAS POTEMRA
    01CY ATTN JOHN DASSOULAS

LOCKHEED MISSILES & SPACE CO INC
P. O. BOX 504
SUNNYVALE, CA 94088
    01CY ATTN DEPT 60-12
    01CY ATTN D. R. CHURCHILL

LOCKHEED MISSILES AND SPACE CO INC
3251 HANOVER STREET
PALO ALTO, CA 94304
    01CY ATTN MARTIN WALT DEPT 52-10
    01CY ATTN RICHARD G. JOHNSON DEPT 52-12
    01CY ATTN BILLY M. MCCORMAC DEPT 52-54

KAMAN SCIENCES CORP
P. O. BOX 7463
COLORADO SPRINGS, CO 80933
    01CY ATTN B. J. BITTNER

LINKABIT CORP
10453 ROSELLE
SAN DIEGO, CA 92121
    01CY ATTN IRWIN JACOBS

M.I.T. LINCOLN LABORATORY
P. O. BOX 73
LEXINGTON, MA 02173
    01CY ATTN LIB A-082 FOR DAVID M. TOWLE
    01CY ATTN MR. WALDEN X113
    01CY ATTN JAMES H. PANNELL L-246
    01CY ATTN D. CLARK

MCDONNELL DOUGLAS CORPORATION
5301 BOLSA AVENUE
HUNTINGTON BEACH, CA 92647
    01CY ATTN N. HARRIS
    01CY ATTN J. MOULE
    01CY ATTN GEORGE MROZ
    01CY ATTN BILL OLSON

MISSION RESEARCH CORPORATION
735 STATE STREET
SANTA BARBARA, CA 93101
    01CY ATTN P. FISCHER
    01CY ATTN W. F. CREVIER
    01CY ATTN STEVEN L. GUTSCHE
    01CY ATTN D. SAPPENFIELD
    01CY ATTN R. BOGUSCH
    01CY ATTN R. HENDRICK
    01CY ATTN RALPH KILB
    01CY ATTN DAVE SOWLE
    01CY ATTN F. FAJEN
    01CY ATTN M. SCHEIBE
    01CY ATTN CONRAD L. LONGMIRE
    01CY ATTN WARREN A. SCHLUETER

MITRE CORPORATION, THE
P. O. BOX 208
BEDFORD, MA 01730
    01CY ATTN J. C. KEENAN
    01CY ATTN G. HARDING
    01CY ATTN CHIEF SCIENTIST W. SEN
    01CY ATTN S. A MORIN
    01CY ATTN C. E. CALLAHAN

PACIFIC-SIERRA RESEARCH CORP
1456 CLOVERFIELD BLVD.
SANTA MONICA, CA 90404
    01CY ATTN F. C. FIELD JR

PHOTOMETRICS, INC.
442 MARRETT ROAD
LEXINGTON, MA 02173
    01CY ATTN IRVING L. KOFSKY

PHYSICAL DYNAMICS INC.
P. O. BOX 21589
SEATTLE, WA 98111
    01CY ATTN E. J. FREMOUW

PHYSICAL DYNAMICS INC.
P. O. BOX 1069
BERKELEY, CA 94701
    01CY ATTN A. THOMPSON
    01CY ATTN JOSEPH B. WORKMAN

R & D ASSOCIATES
P. O. BOX 9695
MARINA DEL REY, CA 90291
    01CY ATTN RICHARD LATTER
    01CY ATTN FORREST GILMORE
    01CY ATTN BRYAN GABBARD
    01CY ATTN WILLIAM B. WRIGHT JR
    01CY ATTN ROBERT F. LELEVIER
    01CY ATTN WILLIAM J. KARZAS

RAND CORPORATION, THE
1700 MAIN STREET
SANTA MONICA, CA 90406
    01CY ATTN CULLEN CRAIN
    01CY ATTN ED BEDROZIAN

SCIENCE APPLICATIONS, INC.
P. O. BOX 2351
LA JOLLA, CA 92038
    01CY ATTN LEWIS M. LINSON
    01CY ATTN DANIEL A. HAMLIN
    01CY ATTN D. SACHS
    01CY ATTN E. A. STRAKER
    01CY ATTN CURTIS A. SMITH
    01CY ATTN JACK MCDOUGAL

RAYTHEON CO.
528 BOSTON POST ROAD
SUDBURY, MA 01776
    01CY ATTN BARBARA ADAMS

SCIENCE APPLICATIONS, INC.
HUNTSVILLE DIVISION
2109 W. CLINTON AVENUE
SUITE 700
HUNTSVILLE, AL 35805
01CY ATTN DALE H. DIVIS

SCIENCE APPLICATIONS, INCORPORATED
8400 WESTPARK DRIVE
MCLEAN, VA 22101
01CY ATTN B. ADAMS

STANFORD RESEARCH INSTITUTE
333 RAVENSWOOD AVENUE
MENLO PARK, CA 94025
01CY ATTN DONALD NEILSON
01CY ATTN ALAN BURNS
01CY ATTN G. SMITH
01CY ATTN L. L. COBB
01CY ATTN DAVID A. JOHNSON
01CY ATTN WALTER G. CHESNUT
01CY ATTN CHARLES L. RINO
01CY ATTN WALTER JAYE
01CY ATTN M. BARON
01CY ATTN RAY L. LEADABRAND

SYSTEM DEVELOPMENT CORPORATION
4130 LINDEN AVENUE
DAYTON, OH 45432
01CY ATTN F. G. MEYER

TECHNOLOGY INTERNATIONAL CORP
75 WIGGINS AVENUE
BEDFORD, MA 01730
01CY ATTN W. P. BOQUIST

TRW DEFENSE & SPACE SYS GROUP
ONE SPACE PARK
REDONDO BEACH, CA 90278
01CY ATTN R. K. PLEBUCH R1-2078
01CY ATTN ROBERT M. WEBB R1-1150

VISIDYNE, INC.
19 THIRD AVENUE
NORTH WEST INDUSTRIAL PARK
BURLINGTON, MA 01803
01CY ATTN CHARLES HUMPHREY
01CY ATTN J. W. CARPENTER